

Microfluidic Scintillation Detectors for High Energy Physics

THÈSE N° 6620 (2015)

PRÉSENTÉE LE 19 JUIN 2015

À LA FACULTÉ DES SCIENCES ET TECHNIQUES DE L'INGÉNIEUR
LABORATOIRE DE MICROSYSTÈMES 4
PROGRAMME DOCTORAL EN MICROSYSTÈMES ET MICROÉLECTRONIQUE

ÉCOLE POLYTECHNIQUE FÉDÉRALE DE LAUSANNE

POUR L'OBTENTION DU GRADE DE DOCTEUR ÈS SCIENCES

PAR

Pietro MAODDI

acceptée sur proposition du jury:

Dr G. Boero, président du jury
Prof. Ph. Renaud, Dr A. Mapelli, directeurs de thèse
Prof. A. Bay, rapporteur
Dr C. Casella, rapporteuse
Dr G. Lehmann Miotto, rapporteuse



ÉCOLE POLYTECHNIQUE
FÉDÉRALE DE LAUSANNE

Suisse
2015

To my brother.



ABSTRACT

This thesis deals with the development and study of microfluidic scintillation detectors, a technology of recent introduction for the detection of high energy particles. Most of the interest for such devices comes from the use of a liquid scintillator, which entails the possibility of changing the active material in the detector, leading to increased radiation resistance. A first part of the thesis focuses on the work performed in terms of design and modelling studies of novel prototype devices, hinting to new possibilities and applications. In this framework, the simulations performed to validate selected designs and the main technological choices made in view of their fabrication are addressed.

The second part of this thesis deals with the microfabrication of several prototype devices. Two different materials were studied for the manufacturing of microfluidic scintillation detectors, namely the SU-8 photosensitive epoxy and monocrystalline silicon. For what concerns the former, an original fabrication approach based on successive bonding and selective release steps of resin layers patterned over sacrificial metal films is detailed. This approach was used to fabricate monolithic, free-standing devices embedding one or two layers of microfluidic channels, with a material budget corresponding to only $\sim 0.03\%$ and $\sim 0.06\%$ of the radiation length of SU-8. A first experimental validation of these devices is presented as well.

Concerning silicon devices, studies on the fabrication of microchannel arrays by both dry and wet etching are reported. Adaptations of these standard techniques to the specific needs of microfluidic scintillation detectors are addressed, specifically the smoothing of scalloped sidewalls resulting from deep reactive ion etching as well as the mask design methodology applied to KOH etching in order to yield microchannels with smooth vertical sidewalls on wafers with the standard $\langle 100 \rangle$ crystalline orientation. The anisotropic characteristics of wet etching were also exploited to demonstrate the fabrication of arrays of microfluidic channels having slanted reflective facets at their extremities, which can act as micromirrors that deviate the scintillation light in the out of plane direction, thus introducing new possibilities for the planar integration of the devices.

Experimental results on the characterization of the light yield and attenuation length of silicon prototype devices performed using electrons from a radioactive source are presented. A brief study on the accelerated ageing of the detector in which the liquid scintillator was

ABSTRACT

damaged by intense UV irradiation is reported. Such study provides encouraging results on how the capability of recirculating the active material in microfluidic scintillation detectors can be used to extend their lifetime or increase the stability of their performance in time.

KEYWORDS

Particle detectors, microfluidics, scintillation detectors, liquid scintillators, microfabrication, silicon, SU-8.

RÉSUMÉ

Cette thèse traite du développement et de l'étude de détecteurs microfluidiques à scintillation, une technologie introduite récemment, pour la détection des particules à haute énergie. Une grande partie de l'intérêt pour ces dispositifs vient de l'utilisation d'un scintillateur liquide, ce qui entraîne la possibilité de remplacer le matériel actif du détecteur, amenant à une meilleure résistance aux radiations. La première partie de la thèse décrit le travail accompli en termes de conception et de modélisation de nouveaux prototypes, en suggérant aussi des nouvelles possibilités et applications. Dans ce cadre, les simulations faites pour valider certains concepts et les principaux choix technologiques faits en vue de leur implémentation, sont détaillées.

La deuxième partie de cette thèse porte sur la microfabrication de différents prototypes. Deux matériaux ont été étudiés pour la construction de détecteurs microfluidiques à scintillation: la résine époxy photosensible SU-8 et le silicium monocristallin. Concernant le premier, une technique de fabrication originale est décrite, s'appuyant sur des étapes successives de soudage et de dissolution sélective de couches de résine structurées sur des couches minces métalliques sacrificielles. Cette technique a été utilisée pour produire des dispositifs monolithiques incluant un ou deux niveaux de canaux microfluidiques, avec un épaisseur correspondant à respectivement $\sim 0.03\%$ et $\sim 0.06\%$ de la longueur de radiation du SU-8. Une première validation expérimentale de ces dispositifs est aussi présentée.

Pour les dispositifs en silicium, des études de fabrication de microcanaux par gravure sèche et humide sont décrites. L'adaptation de ces techniques standards aux besoins spécifiques des détecteurs microfluidiques à scintillation est adressée, en particulier le lissage des parois résultant du procédé de gravure ionique réactive profonde ainsi que la méthodologie de dessin de masques utilisée pour obtenir des microcanaux avec des parois verticales lisses sur des plaques ayant l'orientation cristalline standard $\langle 100 \rangle$, après leur gravure par hydroxyde de potassium. Les caractéristiques anisotropes de la gravure humide ont été aussi exploitées pour démontrer la fabrication de microcanaux incluant des micro-miroirs obliques aux extrémités, qui peuvent dévier la lumière scintillante perpendiculairement au plan des canaux, introduisant des nouvelles possibilités pour l'intégration planaire de ces dispositifs.

Les résultats expérimentaux de la caractérisation de l'efficacité et de la longueur d'atténuation des prototypes en silicium, faite en utilisant

RÉSUMÉ

des électrons émis par une source radioactive, sont présentés. Une brève étude sur le vieillissement accéléré du détecteur, au sein duquel le scintillateur liquide a été endommagé par irradiation ultraviolette intense, est décrite. Cette étude a donné des résultats prometteurs pour la possibilité de circuler le matériel actif dans les détecteurs microfluidiques à scintillation pour augmenter leur durée de vie ou améliorer la stabilité temporelle de leur performance.

MOTS CLÉS

Détecteurs de particules, microfluidique, détecteurs à scintillation, scintillateurs liquides, microfabrication, silicium, SU-8.

ACKNOWLEDGEMENTS

This work was carried out during the years 2012-2015 at Microsystems Laboratory 4, EPFL and at Detector Technology group, CERN. Working in two institutes and cities left me indebted with *many* people for their generous support to this research and for making my time as a PhD student memorable; I'll try here to thank some of them.

First of all, I would like to express my sincere gratitude to my thesis director Professor Philippe Renaud, for accepting me in his group and entrusting me with a great deal of freedom in the elaboration of this project, while always providing precious advice and support throughout. Thank you for running such a great laboratory.

I thank my thesis co-director Alessandro Mapelli, for giving me the opportunity to discover CERN and for his keen and enthusiastic support during these years.

Among the many people that helped me at CERN, I am grateful in particular to Paolo Petagna for his wise supervision during my first year; Benedetto Gorini, Maurice Haguenaer, Giovanna Lehmann Miotto and Stefano Veneziano, for their scientific advice and fruitful discussions during our countless meetings; Christophe Bault and Francisco Perez Gomez for their assistance in mechanical design; Christian Joram for his help with some experiments and finally to my section and group leaders, Andrea Catinaccio and Mar Capeans Garrido, for their support to the project.

I would also like to thank all the group at LMIS₄, in particular Sébastien Jiguet for sharing his knowledge in the art of SU-8 processing and Arnaud Bertsch for his help in chemistry matters and for patiently reviewing this manuscript.

I thank all the staff of the CMi at EPFL, who run an outstanding cleanroom in which I spent many hours, as well as the numerous users that I got to know there – in particular Clara, Davide, Emilie, Hadrien, Enrica, Samuel and Alessia – for transforming those hours of work into delightful chatting.

Much gratitude is deserved by the students I had the chance to help supervise, for their contributions and for teaching me many things. Thanks Dara, David, Ludovic, Eric, Leili, Guillaume, Cindy, Davy, Mikhail, Hari, Jacopo and Rosalia.

ACKNOWLEDGEMENTS

A special thank goes to the many colleagues-turned-friends I was lucky enough to meet during these years.

In particular I thank Gaia & Giulia, for transforming room 20-1-014 at CERN into “The Best Office”: music, laughs and *La Zanzara* in the air, plants and flowers literally *everywhere*. Thanks also to our frequent visitors “Ali” and Andrea, our neighbour Jérôme, and to all the friends and lunchmates in Geneva: Antonella, Aniello, Francesco, Stefano, Marco, Raffaello, Tiziana, Mauro, Jessica and Diego, for the great times together!

My greatest thanks go to *Les Amis* and extended family: Matteo, Bea, Antonio, Patrizia, Lucian, Mariana, Diego, Giovanna, Sergio and Om-bretta, with whom I shared moments that I’ll never forget. Grazie ragazzi! And also thanks to H el ene, the French *r esistance* in our otherwise all-Italian outpost in Bussigny. Merci pour tout!

I would like to thank Camillo and Giulia for the many ski trips, nights of master-level Burraco playing, wonderful meals and general nice time together in Chavannes.

No less gratitude goes to all the friends at EPFL, especially to the historic LMIS(2+4) lunch and coffee (and often, Sat) fellowship: thank you Pierre, Sophie, Fabien, Robert, Jagoda, Bilge, Jules, Elodie, Rima, Cristina, Amelie, Niccol o, Guillaume, Stefano and Carolin! I also have to thank Mojtaba and Shady for always carrying a smile and a kind word whenever we cross paths in the lab.

Vorrei infine ringraziare mia madre, mio padre e mio fratello Emilio, per il loro supporto e amore incodizionato.

Thanks everyone.

Lausanne, April 2015

CONTENTS

ABSTRACT	iii
RÉSUMÉ	v
ACKNOWLEDGEMENTS	vii
PREFACE	1
Thesis outline	1
1 SCINTILLATION DETECTORS	3
1.1 Particles-matter interactions	3
1.1.1 Energy loss by heavy particles	3
1.1.2 Energy loss by electrons	4
1.1.3 Fluctuations in energy loss	6
1.1.4 Scattering	7
1.2 Scintillators	8
1.2.1 Scintillation in organic materials	8
1.2.2 Scintillation in inorganic materials	10
1.2.3 Radiation damage in scintillators	11
1.3 Photodetectors	11
1.3.1 Photomultiplier tubes	12
1.3.2 Photodiodes	13
1.3.3 Silicon photomultipliers	15
1.4 State of the art scintillation detector technologies . . .	16
1.4.1 Fibres	16
1.4.2 Capillaries	18
1.4.3 Microfluidics	20
2 DESIGN AND MODELING OF MICROFLUIDIC DETECTORS	23
2.1 Motivation and goals	23
2.2 Study of light propagation in microchannels	25
2.2.1 Simulation method	25
2.2.2 Evaluation of optical coatings	26
2.3 Case studies	29
2.3.1 A thin SU-8 microfluidic scintillation detector .	29
2.3.2 A microfluidic scintillation detector with out-of- plane light output	30
2.4 Conclusions and outlook	32
3 SU-8 MICROFLUIDIC DEVICES FOR SCINTILLATION DETECTION	35
3.1 The SU-8 photoepoxy	35

CONTENTS

3.2	Fabrication of single layer devices	36
3.2.1	Preparation of the substrates	36
3.2.2	Patterning of the first SU-8 layer	38
3.2.3	Patterning of the second SU-8 layer	38
3.2.4	Wafer bonding and device release	39
3.3	Fabrication of double layer devices	39
3.3.1	Substrates preparation	39
3.3.2	Patterning of the first SU-8 layer	41
3.3.3	Patterning of the second SU-8 layer	41
3.3.4	First wafer bonding and selective release	41
3.3.5	Final bonding and device release	41
3.4	Optical coating experiments	42
3.4.1	Materials and methods	42
3.4.2	Results	44
3.5	Experimental validation	44
3.6	Conclusions and outlook	45
4	SILICON MICROFLUIDIC DEVICES FOR SCINTILLATION DETECTION	49
4.1	Introduction	49
4.2	Fabrication of devices by dry etching	49
4.2.1	Deep reactive ion etching of silicon	50
4.2.2	Dry etching of microfluidic channels and inlets	51
4.2.3	Surface smoothing and optical coating	52
4.2.4	Fluidic and optical packaging	53
4.3	Fabrication of devices by wet etching	54
4.3.1	Anisotropic wet etching of silicon	54
4.3.2	Alignment of masks to the silicon crystal	55
4.3.3	Wet etching of the microchannels	56
4.3.4	Devices with in-plane light output	59
4.3.5	Devices with out-of-plane light output	60
4.4	Light yield measurements	60
4.4.1	Measurement setup	60
4.4.2	Data analysis	62
4.5	Scintillator damage studies	65
4.6	Conclusions and outlook	68
5	CONCLUSIONS AND OUTLOOK	71
A	INTERNALS OF THE CUSTOM MONTE CARLO SIMULATOR	75
A.1	Structure and dependencies	75
A.2	Models	76
A.3	Photon propagation	76

CONTENTS

B ADDITIONAL APPLICATIONS FOR THE SU-8 BONDING AND RE- LEASE PROCESS	81
GLOSSARY	83
BIBLIOGRAPHY	85
CURRICULUM VITAE	95

LIST OF FIGURES

Figure 1.1	Stopping power for positive muons in copper.	5
Figure 1.2	Energy loss distribution for a 10 GeV positive muon passing through 1.7 mm of silicon. . . .	6
Figure 1.3	Quantities for a simplified description of scattering.	7
Figure 1.4	Depiction of the photon emission mechanisms of hydrocarbon-based scintillators.	9
Figure 1.5	Basic structure and working principle of a PMT.	13
Figure 1.6	Sketch of the working principle of a p-i-n photodiode.	14
Figure 1.7	SiPM schematic and optical micrograph. . . .	15
Figure 1.8	Light collection in a scintillating optical fibre. .	17
Figure 1.9	Prototype detector based on capillaries filled with liquid scintillator.	19
Figure 1.10	Working principle of a microfluidic scintillation detector.	21
Figure 2.1	Concept of xy position detection using two layers of microfluidic channels.	24
Figure 2.2	Reflectivity of aluminium and Teflon AF films on silicon.	27
Figure 2.3	Reflectivity of aluminium and Teflon AF films on silicon.	28
Figure 2.4	Monte Carlo simulations of the light transport efficiency in square microchannels.	28
Figure 2.5	Stopping power for electrons in <i>pseudocumene</i> .	31
Figure 2.6	3D model of an array of 63 SU-8 horizontal microchannels.	31
Figure 2.7	Monte Carlo simulation of light transport efficiency in microchannels.	31
Figure 2.8	Schematic depiction of model geometry for simulation.	33
Figure 2.9	Monte Carlo simulations of photon hits distribution on a pixel.	33
Figure 3.1	Structural formula of the SU-8 oligomer. . . .	36
Figure 3.2	Process developed for the fabrication of free standing, monolithic SU-8 microfluidic devices.	37
Figure 3.3	Process developed for the fabrication of SU-8 devices with two embedded microchannel layers.	40

LIST OF FIGURES

Figure 3.4	Optical micrograph of a SU-8 device filled with a colorant.	42
Figure 3.5	Procedure used for the microchannel coating experiments.	43
Figure 3.6	SEM micrographs of coated microchannel cross sections.	45
Figure 3.7	Measurement of the light output from a SU-8 microchannel array.	46
Figure 4.1	Smoothing of silicon microchannels.	51
Figure 4.2	Schematic process flow for the fabrication of dry etched microfluidic channels in silicon. . .	52
Figure 4.3	Silicon devices fabricated by dry etching.	54
Figure 4.4	Depiction of the three main crystalline planes of silicon.	55
Figure 4.5	Marks for the alignment to silicon crystal planes.	56
Figure 4.6	Etch rate measured in the in-plane direction for $\langle 100 \rangle$ silicon wafers exposed to 50% KOH at 78 °C.	58
Figure 4.7	Simplified calculation of the microchannel geometry resulting from KOH etching.	58
Figure 4.8	Test microchannels etched by 40% KOH at 60 °C.	61
Figure 4.9	Alternative designs for the termination of wet-etched microchannels.	61
Figure 4.10	SEM micrograph showing the cross section of a Al-Al thermocompression bonding.	61
Figure 4.11	Sketch of the design used for the fabrication of microchannel ends featuring slanted mirror facets.	62
Figure 4.12	Typical spectrum of the detector output signals.	63
Figure 4.13	Schematic depiction of some parameters of the model over experimental data.	66
Figure 4.14	Distribution of output signals from a microchannel.	66
Figure 4.15	Scan of the trigger position along a microchannel.	67
Figure 4.16	Light output from the scintillator under continuous UV irradiation.	67
Figure 4.17	Light output from the scintillator for increasingly high flow rates.	68
Figure A.1	Reflectivity maps for a microchannel coating consisting of 10 alternated layers of TiO ₂ (35 nm) and SiO ₂ (72 nm).	77

LIST OF FIGURES

Figure A.2	Simulations of a pencil beam of photons being reflected from a specular, rough, and diffusive surface.	77
Figure B.1	Colourised SEM micrographs of various microstructures completely made of SU-8, using the processing technique described in Chapter 3.	81

LIST OF TABLES

Table 1.1	Physical quantities for the description of particles-matter interactions.	4
Table 4.1	Parameters for the model of the detector output statistics.	65

PREFACE

Devices exploiting the phenomenon of scintillation are used since the beginning of the previous century for the detection of ionising particles. The first scintillation detectors, pioneered by Crookes [1], relied on the human eye to spot the faint light flashes emitted by zinc sulphide screens. The coupling of this crystal to photomultiplier tubes in 1944 by Curran and Baker [2, 3] marked the birth of modern electronic scintillation detectors. ZnS remained the only inorganic scintillator used for radiation detection until 1949, when sodium iodide crystals doped with thallium were introduced by Hofstadter [4]. Tens of other scintillating inorganic crystals were discovered since and are still widely used today. Detectors based on organic scintillators have a history as long lasting, starting with the coupling of naphthalene crystals to photomultiplier tubes in 1947 by Kallmann and Broser [5], followed right after by anthracene [6] and stilbene [7]. The introduction of scintillating liquids [8, 9] and plastics [10] allowed years later the production of large scintillator volumes at lower costs. In particular, tracking detectors based on liquid scintillators were studied in the 1990s in the framework of the CERN RD46 collaboration [11], with encouraging results. More recently, microfabrication techniques were applied to the development of novel detectors in which commercial liquid scintillators are injected in arrays of microfluidic channels [12]. In this thesis, novel developments and studies on devices based on this kind of technology, hereby called *microfluidic scintillation detectors*, are presented.

THESIS OUTLINE

The theoretical bases underlying the operation of scintillation detectors are given in Chapter 1, together with examples of state of the art technologies and applications relevant to this work. In Chapter 2 the motivations and goals of this thesis are discussed, and the methodology used for the design of prototype microfluidic scintillation detectors, as well as the modelling results of selected case studies, are presented. The fabrication processes that were developed and the experiments performed on the devices obtained with such processes, are treated in Chapters 3 and 4, gathering respectively the work performed on SU-8 devices and silicon devices. Finally, general conclusions and perspectives for this work are discussed in Chapter 5.

1 | SCINTILLATION DETECTORS

In this chapter the theoretical bases underlying the operation of scintillation detectors are given, as well as examples of current technologies and applications. Section 1.1 offers a brief summary of the particle-matter interactions we are interested in, with this work, while the physics of scintillation is discussed in section 1.2. Section 1.3 deals with several technologies for light sensing used in detectors. Finally, selected state-of-the-art scintillation detector technologies and applications are presented in section 1.4.

1.1 PARTICLES-MATTER INTERACTIONS

When a high energy charged particle passes through a material, it interacts with its constituent atoms in a series of discrete collisions with their nuclei and electrons [13]. The main effects of these collisions on the incident particle are energy loss and deflection of its trajectory. Here we briefly discuss these effects in cases that are commonly encountered in the operation of particle detectors. The physical quantities intervening in the following treatment are grouped in Tab. 1.1 for convenience.

1.1.1 Energy loss by heavy particles

Particles heavier than electrons (such as muons, protons, etc.) lose energy by inelastic scattering with the electronic shells, while elastic collisions with the nuclei deflect their trajectory. Since the energy lost in each interaction is randomly distributed, the exact value of the energy loss rate $-dE/dx$ cannot be calculated a priori; however its mean value, called *stopping power*, can be. For moderately relativistic particles ($\beta\gamma \sim 0.1 \dots 1000$), the stopping power in $\text{MeV g}^{-1} \text{cm}^2$ is well described by the *Bethe equation*:

$$\left\langle -\frac{dE}{dx} \right\rangle = Kz^2 \frac{Z}{A} \frac{1}{\beta^2} \left(\frac{1}{2} \ln \frac{2m_e c^2 \beta^2 \gamma^2 W_{\max}}{I^2} - \beta^2 - \frac{\delta(\beta\gamma)}{2} \right) \quad (1.1)$$

Table 1.1.: Physical quantities for the description of particles-matter interactions.

Symbol	Definition	Value or units
K	$4\pi N_A r_e^2 m_e c^2$	$0.307 \text{ MeV mol}^{-1} \text{ cm}^2$
N_A	Avogadro's number	$6.022 \times 10^{23} \text{ mol}^{-1}$
r_e	classical electron radius	$2.818 \times 10^{-15} \text{ m}$
$m_e c^2$	electron mass $\times c^2$	0.511 MeV
c	speed of light	$299\,792\,458 \text{ m s}^{-1}$
z	charge number of the particle	
Z	atomic number of the absorber	
A	atomic mass of the absorber	g mol^{-1}
β	ratio between particle speed and light speed	
γ	$1/\sqrt{1-\beta^2}$ (Lorentz factor)	
W_{\max}	maximum energy transfer in a single collision	MeV
I	mean excitation energy	eV
$\delta(\beta\gamma)$	density effect correction to ionization energy loss	
p	momentum	MeV/c
X_0	radiation length	g cm^{-2}

Non-elemental materials are accounted for by simply considering them as made up of layers of pure elements:

$$\left\langle -\frac{dE}{dx} \right\rangle = \sum_i w_i \left\langle -\frac{dE}{dx} \right\rangle_i \quad (1.2)$$

Where w_i is the fractional weight of the i th element in the compound. An example of the behaviour of Eq. (1.1) calculated for positive muons in copper is given in the Bethe region of Fig. 1.1. In most practical cases encountered in the operation of detectors, particles have mean energy losses close to the minimum of the Bethe curve; such particles are referred to as *minimum ionizing particles* or *MIPs*. The stopping power curve can be integrated to estimate the mean distance that a particle can travel into a material before losing all its energy (*total range*). This kind of simplified calculation is called *continuous slowing down approximation*, or *CSDA*, of the total range [14, p. 400].

1.1.2 Energy loss by electrons

For electrons the stopping power is not well described by Eq. (1.1), mainly because the identical nature of the particles taking part in the interaction (the incident electrons versus the the atomic electrons)

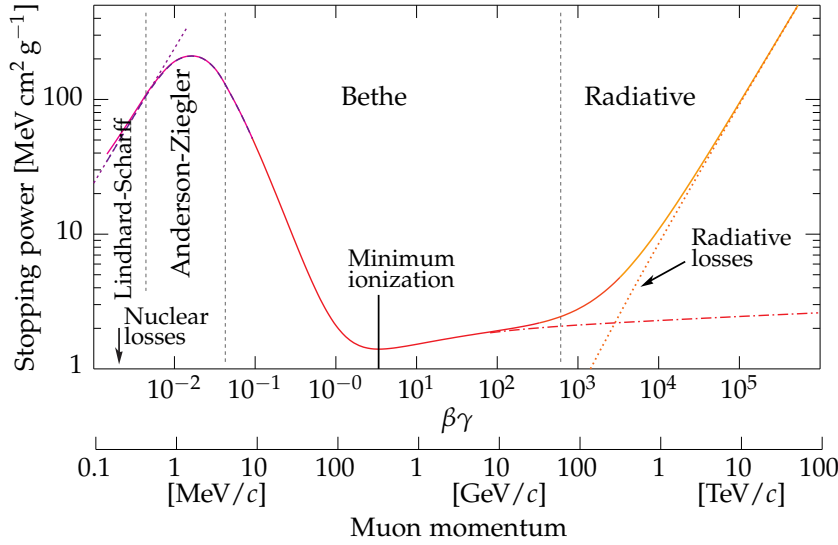


Figure 1.1.: Stopping power $\langle -dE/dx \rangle$ for positive muons in copper as a function of momentum, adapted from [14, p. 399]. In typical cases particles hitting detectors have momenta in the Bethe region of the curve, and in particular close to the minimum ionization. Radiative losses by heavy particles only become important at extremely high energies (this is not the case for electrons, for which the curve is shifted towards lower energies – see section 1.1.2).

must be accounted for. In this case the stopping power can be derived from the Møller cross section [15]:

$$\begin{aligned} \left\langle -\frac{dE}{dx} \right\rangle = & \frac{K Z}{2 A \beta^2} \left[\ln \frac{m_e c^2 \beta^2 \gamma^2 W_{\max}}{I^2} \right. \\ & \left. + (1 - \beta^2) - \frac{2\gamma - 1}{\gamma^2} \ln 2 + \frac{1}{8} \left(\frac{\gamma - 1}{\gamma} \right)^2 - \delta \right] \end{aligned} \quad (1.3)$$

Where the maximum energy transfer in a collision $W_{\max} = \frac{1}{2} m_e c^2 (\gamma - 1)$ is half the kinetic energy of the incident electron. For positrons the treatment is similar except one has to use the Bhabha cross section and W_{\max} corresponds to the whole kinetic energy [15].

At higher energies the energy loss of electrons is dominated by bremsstrahlung (radiative losses). In this regime the stopping power is $\langle -dE/dx \rangle = E/X_0$, where X_0 is the characteristic amount of matter traversed by an electron, called *radiation length* and measured in g cm^{-2} . In particular, the ratio X_0/ρ between the radiation length and the density of a material gives the mean distance the electron can travel in the material before losing all but $1/e$ of its energy. For this reason the thickness of components in detector systems are often given in units of X_0 . The radiation length for an elemental material can be conveniently calculated by the following empirical formula:

$$X_0 = \frac{716.4 \cdot A}{Z(Z+1) \ln(287 \cdot Z^{-1/2})} \quad (\text{g cm}^{-2}) \quad (1.4)$$

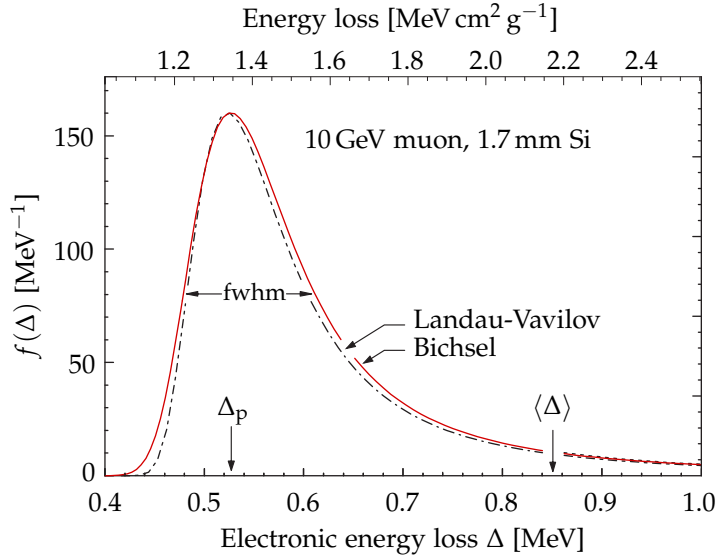


Figure 1.2.: Electronic energy loss distribution for a 10 GeV positive muon passing through 1.7 mm of silicon, calculated by both the classical Landau-Vavilov distribution and the more recent Landau-Vavilov-Bichsel which includes the density correction $\delta(\beta\gamma)$. The full width at half maximum (fwhm) is about 4ζ . The mean value $\langle\Delta\rangle$ is considerably higher than the most probable value Δ_p because of the long tail of the distribution. Adapted from [14, p. 402].

For compound materials, the total radiation length can be approximated by:

$$\frac{1}{X_0} = \sum_i \frac{w_i}{X_{0,i}} \quad (1.5)$$

Where $X_{0,i}$ is the radiation length of the i th element and w_i its fractional weight.

1.1.3 Fluctuations in energy loss

The concept of stopping power alone is not sufficient to describe the energy loss of particles in many practical cases, e.g. when dealing with detectors of limited thickness ($x \sim 1$ mm). In this case the stochastic nature of the energy exchange in the single collisions dominates the behaviour of the energy loss and large deviations from the mean value are observed. For a detector of thickness x , the probability distribution $f(\Delta, \beta\gamma, x)$ of the energy loss Δ can be modelled by the *Landau-Vavilov-Bichsel distribution* [16], which has the most probable value Δ_p for the energy loss given by:

$$\Delta_p = \zeta \left[\ln \frac{2mc^2\beta^2\gamma^2}{I} + \ln \frac{\zeta}{I} + 0.2 - \beta^2 - \delta(\beta\gamma) \right] \quad (1.6)$$

where $\zeta = (K/2)(Z/A)(x/\beta^2)$ MeV, with x expressed in g cm^{-2} (i.e. multiplied by the density of the material). Given the highly-skewed

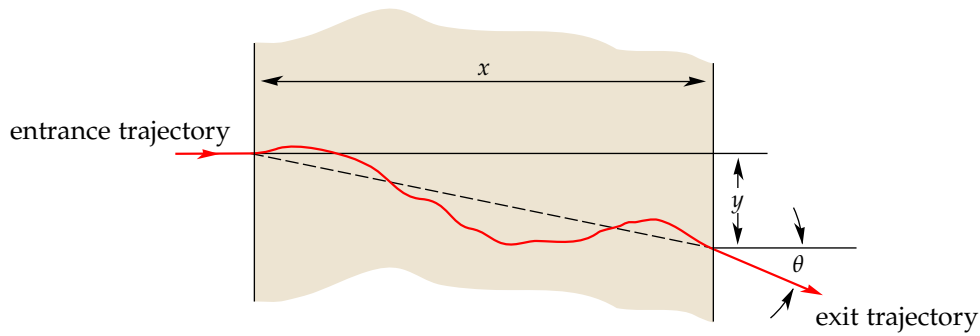


Figure 1.3.: Quantities used for a simplified description of scattering, adapted from [14, p. 403].

shape of the distribution, of which an example is shown in Fig. 1.2, Δ_p is considerably lower than the mean value $\langle \Delta \rangle$, which divided by the thickness x corresponds to the $\langle dE/dx \rangle$ quantity discussed before. Since roughly 90% of the collisions contribute to energy deposits below $\langle \Delta \rangle$, one should not use Eq. (1.1) or Eq. (1.3) for describing energy loss by single particles in detectors of limited thickness, but rather the quantity Δ_p/x . For very thin detectors ($x < 0.1$ mm) even the Landau distribution does not agree any longer with the experimental data, in which its width 4ζ significantly underestimates the actual spread in energy losses. However the most probable value Δ_p/x , which scales with thickness as $a \ln x + b$, can still be calculated adequately using Eq. (1.6).

1.1.4 Scattering

Apart from losing energy, a particle passing through a material is deflected by a series of scatters. For charged particles this is mostly due to Coulomb interaction with nuclei (however for hadrons also the strong interaction contributes). Assuming an incident particle with a trajectory perpendicular to a layer of thickness x of an isotropic material, it is possible to study the deflection of the trajectory by considering its projection onto a plane containing the entrance and exit points, as shown in Fig. 1.3; on such a plane the deflection of the trajectory can be described simply by the couple (y, θ) . If one considers a large number of random small-angle scatters, the net distributions of y and θ can be modelled as Gaussian, because of the central limit theorem. Using a Gaussian fit approximation of the Molière distribu-

tion [17], the root mean square values of y and θ are described by the relations [18, 19]:

$$\theta^{\text{rms}} = \frac{13.6 \text{ MeV}}{\beta c p} z \sqrt{\frac{x}{X_0}} \left[1 + 0.038 \ln \frac{x}{X_0} \right] \quad (1.7)$$

$$y^{\text{rms}} = \frac{1}{\sqrt{3}} x \theta^{\text{rms}} \quad (1.8)$$

For thin layers (or for large-angle scatters) the Gaussian approximation does not hold any more, and longer tails appear in the distribution of the experimental data. Moreover it should be noted that for anisotropic materials (e.g. silicon) scattering depends on the orientation of the particle trajectory with respect to the crystal lattice.

1.2 SCINTILLATORS

As discussed in the previous section, when high energy particles pass through a material they lose energy, leaving a trail of excited atoms. In a particular class of materials a small fraction of this energy is released as optical photons: this phenomenon is called *scintillation* and the materials exhibiting it are known as *scintillators* (or *scintillating materials*). Scintillators can be classified according to their chemistry in organic and inorganic materials, exhibiting different properties and light production mechanisms.

1.2.1 Scintillation in organic materials

Organic scintillators exist in the form of organic crystals (e.g. anthracene, stilbene, naphthalene), plastics (e.g. polystyrene, polyvinylbenzene, polyvinyltoluene) and liquids (e.g. toluene, xylene, pseudocumene). In actual applications organic crystals are seldom used, because they are difficult to grow in large sizes and to machine; nonetheless the light yield of scintillating plastics and liquids is often expressed as a percent of the light yield of anthracene, which is the highest of all known organic scintillators.

It can be noted that all practical organic scintillators are aromatic hydrocarbon compounds [20], meaning their molecules feature delocalized electrons in π orbitals. Upon absorbing energy from a high energy particle, a molecule with π -electrons in the ground singlet state S_0 can transition to higher energy states which are, in order of increasing energy, the excited singlet states S_1, S_2, \dots and the triplet states T_0, T_1, T_2, \dots [21]. Molecules in higher excited singlet states decay very rapidly (~ 10 ps) to the first excited state S_1 with no emission of photons (internal degradation) [22, p. 162]. S_1 then decays

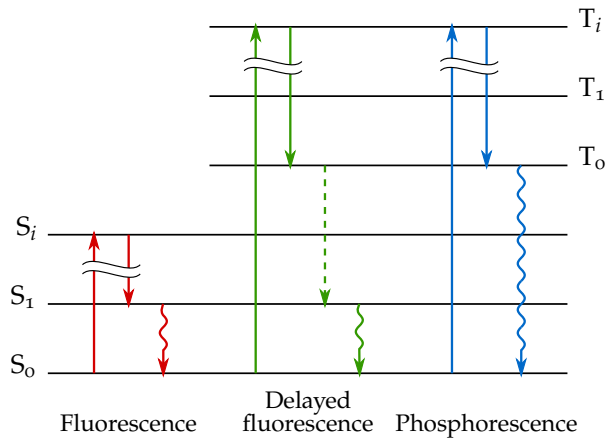


Figure 1.4.: Depiction of the three photon emission mechanisms that occur in scintillators based on aromatic hydrocarbons. In fluorescence, the most common and rapid mechanism, UV photons are generated via the $S_1 \rightarrow S_0$ transition. The same goes for delayed fluorescence, except the slow T_0 - T_0 interaction between two excited molecules precedes the fluorescent transition. The slowest process is phosphorescence, in which UV photons of shorter wavelength are produced via the rare $T_0 \rightarrow S_0$ transition.

back to the ground state S_0 with the emission of a UV photon: this is the phenomenon of *fluorescence*, the fast component of light emission in scintillation. Excited triplet states instead, decay immediately to the ground triplet state T_0 with no emission of photons. A molecule in the state T_0 generally interacts with another molecule in the same state, with the mechanism: $T_0 + T_0 \rightarrow S_1 + S_0 + \text{phonons}$, that leaves one of the molecules in the excited single state S_1 , which then undergoes the $S_1 \rightarrow S_0$ fluorescent transition with the emission of UV photons. Because the T_0 - T_0 interaction is slow, this component of scintillation is called *delayed fluorescence*. A last possibility is the direct transition $T_0 \rightarrow S_0$, which has a low probability of occurrence and is therefore very slow (more than 100 μs): this is the *phosphorescence* component of scintillation, yielding UV photons of shorter wavelength because of the higher energy difference between T_0 and S_0 . A schematic depiction of these mechanisms is given in figure Fig. 1.4.

Because the photons emitted by scintillation have energies corresponding to definite state transitions, they can be reabsorbed by the scintillator itself and have therefore rather short attenuation lengths (several mm) [14, p. 417]. To address this problem, wavelength shifting molecules called *fluors* are added to a scintillating base, so that the UV photons can be absorbed and re-emitted at longer wavelengths (usually in the blue or green region). If a fluor is dissolved at high concentrations ($\sim 1\%$ in weight), the mean distance between a molecule of base and a fluor one is of the order of 10 nm: at this scale the main energy transfer mechanism between the two molecules is not the exchange of UV photons but rather a resonant dipole-dipole interaction

known as *Förster energy transfer*, which strongly couples the base and the fluor [23]. Therefore a *primary* fluor in high concentration is often used to increase the speed and the light yield of the scintillator, while a *secondary* fluor is often added in lower concentrations ($\sim 0.05\%$ in weight) to further shift the wavelength to the region of interest (usually chosen where the available photodetectors are more efficient).

The typical light yield of commercial organic scintillators is about one photon per 100 eV of energy deposited [24], while the decay times are of the order of 1 ns. Light output spectra are generally centred in the blue region ($\lambda_0 \sim 425$ nm).

1.2.2 Scintillation in inorganic materials

Inorganic scintillators exist in form of crystals (CsI, BaF₂, PbWO₄, ...), noble gases (He, Ar, Xe, ...) and glasses (Ce-doped lithium or boron silicates).

Inorganic crystals exhibit an electronic band structure with an energy gap separating the fully populated valence band from the empty conduction band. Impurities are added to the crystal to form *luminescent centres* which locally introduce states having energies that fall in the middle of the forbidden gap. Upon excitation induced by a high energy particle, electrons jump to the conduction bands leaving their corresponding holes in the valence band. These carrier pairs recombine at luminescent centres, where the electrons first transition non-radiatively to the intermediate energy states introduced by the dopant and then fall back to the valence band and recombine with holes, with the emission of scintillation photons [25, p. 232]. It is also possible for electrons in the conduction band to transition to trap states in the middle of the energy gap which have long recombination times; this introduces a slow component to the scintillation process. The recombination time constants and the wavelength of the emitted photons depend on the type of crystal and dopant, however inorganic crystal scintillators are generally slower (time constants of $\sim 10 - 100$ ns) than organic scintillators. The light yield of inorganic crystals is very high, in the order of about 4 photons per 100 eV of energy deposited. Inorganic crystal scintillators also have higher atomic numbers and therefore much higher densities ($\rho \sim 4 - 8$ g cm⁻³) than organic scintillators ($\rho \sim 1$ g cm⁻³), meaning they are preferred in applications where a high stopping power is needed, such as calorimetry.

In gases the light emission mechanism is the simple de-excitation of single atoms which transitioned to excited energy level upon the passage of a high energy particle: this process is very rapid (~ 1 ns) and the emitted photons are in the UV region. Wavelength-shifting

coatings may be applied to the walls of the gas container to obtain output spectra suited to usual photodetectors.

Scintillating glasses based on lithium or boron are used in very specialized application such as neutron detection (because of the high neutron cross sections of Li and B [26]) or in chemically harsh environments where a resistant scintillator is needed. They have however rather low light yields (~ 0.35 photons per 100 eV of energy deposited).

1.2.3 Radiation damage in scintillators

All known scintillators are subject to radiation damage, with effects depending on a plethora of factors such as the scintillator chemistry, the nature of radiation (gamma rays, protons, neutrons, . . .), the total radiation dose and dose rate, the composition of the surrounding atmosphere (presence of oxygen in particular), the temperature. The main effects observed in scintillators are the degradation of the light yield and of the optical transparency, but the mechanisms underlying these effects are complex and not well understood [14, p. 417].

The dominant effect upon intense irradiation is the appearance of *colour centres* which increase light absorption at short wavelengths, reducing the intensity and the uniformity of the scintillator response. In organic scintillators this phenomenon can be mitigated by the addition of fluors that shift the light output to longer wavelengths (green, red). In typical plastic scintillators significant degradation of the light yield is observed after doses of $10^3 - 10^4$ Gy [25, p. 224], although certain formulations show little effects up to doses as high as 10^5 Gy [27]. Inorganic crystals are more prone to radiation damage than plastics, with damage that can appear in the less resistant materials after doses as small as 10 Gy [25, p. 247]. The defects induced in an inorganic crystal degrade both the light yield and the response time of the scintillator, because trap states with long decay times are created, leading to phosphorescent emission. Of particular interest among scintillators are organic liquids which, lacking a crystalline or even a solid structure, are significantly more resistant to radiations [28, 29].

1.3 PHOTODETECTORS

In order to obtain a particle detector, a scintillator needs to be coupled to a photodetector that converts the light produced upon the passage of a particle into an electrical signal. In this section we describe the

main technologies used for light detection in scintillation detectors and relevant to the experimental part of this work in particular.

1.3.1 Photomultiplier tubes

The most used photodetector in particle physics experiments to date is the *photomultiplier tube*, or *PMT* [30]. The basic structure of a PMT consists in a tube inside which vacuum is created ($\sim 10^{-6}$ mbar), featuring a transparent window through which the photons can enter. A material with a low work function (chosen according to the wavelength range of interest) is deposited on the inner surface of the window, constituting the *photocathode*. When a photon hits the photocathode, a free electron is emitted by photoelectric effect. This electron is accelerated by the focusing electrode placed behind the photocathode towards a chain of *dynodes*, which are nickel or steel electrodes coated with secondary emissive materials (e.g. BeO, MgO, ...) and biased at increasing voltages [31, p. 17]. When the electron hits the first dynode, more electrons are liberated because of secondary emission. These electrons are then accelerated to the next dynode of the chain, where the process is repeated and each of them generates other electrons by secondary emission. This process is illustrated in figure Fig. 1.5. At the end of the dynode chain, the multiplied electrons are collected by the anode, resulting in an appreciable output current pulse. This multiplication process can be modelled introducing a gain factor G [14, p. 414]:

$$G = AV^{kn} \quad (1.9)$$

where $k \sim 0.7 - 0.8$ and A are constants depending on the material and number n of dynodes, while V is the applied high voltage. The gain is typically of $\sim 10^5 - 10^6$ electrons per one photon. The detection efficiency of PMTs depends mostly on the quantum efficiency of the photocathode, which is a wavelength-dependent quantity. For bialkali photocathodes, often used in couple with organic scintillators, the peak quantum efficiency is $\sim 27\%$ at 390 nm [31, p. 35]. It should be noted that the output signal from a PMT is not deterministic (i.e. a given number of photons hitting the photocathode does not always correspond to the same number of output electrons) because of the quantum efficiency, the statistical fluctuations in the electron multiplication process (in particular Eq. (1.9) only gives an average value for the gain), the noise of the readout electronics, etc.

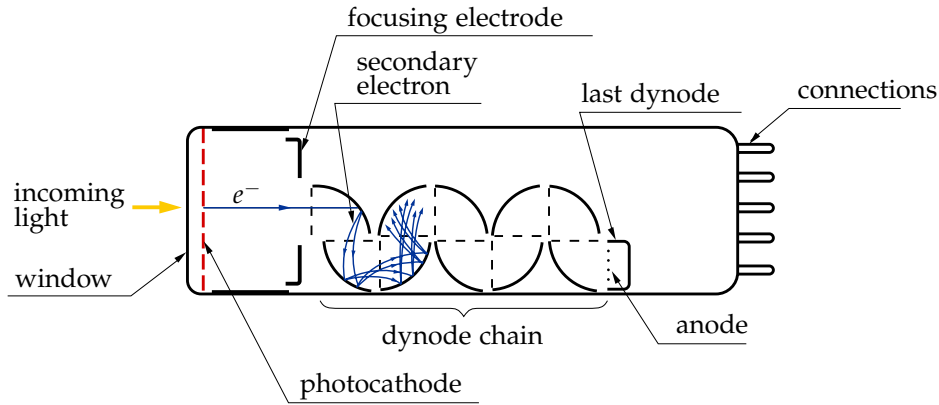


Figure 1.5.: Depiction of the basic structure of a photomultiplier tube and its working principle (adapted from [31, p. 13]). An incoming photon enters the transparent window and is converted to an electron by the photocathode. This electron is accelerated towards the dynode chain by the focusing electrode. When an electron hits a dynode one or more additional electrons are generated by secondary emission, so that at the end of the dynode chain many electrons ($\sim 10^5 - 10^6$) are collected by the anode.

1.3.2 Photodiodes

Photodiodes are one of the simplest semiconductor photodetectors. The basic structure of a photodiode is based on a semiconductor p-n junction in reverse bias. In dark conditions the only current through the junction is given by the leakage of minority carriers, thermal noise and shot noise. These phenomena constitute the *dark current* I_{dark} , related to the reverse saturation current I_{sat} and to the bias voltage of the diode as [32]:

$$I_{\text{dark}} = I_{\text{sat}} \left(e^{\frac{eV}{k_B T}} - 1 \right) \quad (1.10)$$

where e is the elementary charge, k_B the Boltzmann constant, T the temperature and V the voltage applied to the photodiode. When an incoming photon is absorbed in the depleted region across the junction, it excites an electron-hole pair (this is the simple *photogeneration* of charge carriers in semiconductors). Because of the high electric field in the depleted region resulting from the reverse bias, the two carriers are separated and accelerated towards opposite directions (thus they cannot recombine), creating a *photocurrent* I_{ph} which depends on the illumination of the junction and adds up to the dark current.

$$I_{\text{ph}} = -\varepsilon_q \frac{\lambda e}{hc} P_{\text{opt}} \quad (1.11)$$

$$I = I_{\text{dark}} + I_{\text{ph}} \quad (1.12)$$

where $\varepsilon_q(\lambda)$ is the quantum efficiency of the photodiode, P_{opt} the incident optical power, λ the wavelength, and the other symbols indicate the canonical physical constants.

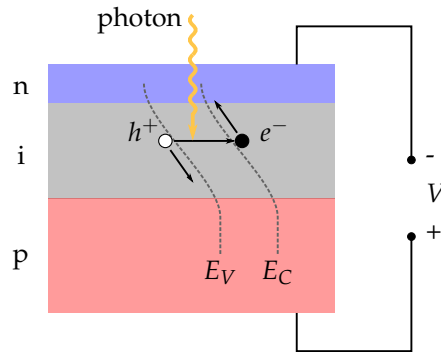


Figure 1.6.: Sketch of the working principle of a p-i-n photodiode. The junction is in reverse bias ($V < 0$), so in dark conditions the energy barrier prevents the majority carriers in a region to drift to the other and viceversa (only a small dark current is present). Upon the absorption of a photon in the vicinity or inside the intrinsic zone, an electron-hole pair is excited, respectively in the conduction band E_C and in the valence band E_V . Because of the electric field in the intrinsic zone, these carriers are separated and drift towards the electrodes creating a photocurrent.

Since the depleted region in a p-n junction has a thickness in the order of $\sim 1 - 10 \mu\text{m}$, in order to increase the size of the high electric field region where photons need to be absorbed (and thus the quantum efficiency of the device), the p-i-n structure is used in most photodiodes, featuring an intrinsic (i.e. with null net doping) semiconductor region between the doped sides (see Fig. 1.6). High quantum efficiencies (up to 90% at the peak wavelength) can be achieved with such structure. Moreover photodiodes can be patterned in very large arrays containing many small independent pixels. It has to be noted that, albeit the quantum efficiency of the carrier generation process can be high, the gain of such a device is unitary: one electron-hole pair contributing to the photocurrent is generated at most per each photon. Hence a simple photodiode, unlike a PMT, is not sensitive to single photons because in this case the photocurrent is too low with respect to the dark current and its fluctuations, and cannot be distinguished in the output (see Eq. (1.12)). At room temperature the minimum detectable signal is typically of several hundreds of photons [14, p. 416].

To address such problems a particular class of photodiodes called *avalanche photodiodes* or *APDs* were introduced. The p-i-n structure of APDs is optimised to operate in very high reverse bias. In such condition the electric field across the depleted region is so high that the drifting photogenerated carriers acquire enough energy to generate further carriers by *impact ionization*. This effect is called *avalanche breakdown*, and leads to the multiplication of the number of carriers, which can be modelled introducing a gain factor G in Eq. (1.11); as a result a detectable electrical signal can be obtained even for very low light levels. However the operation of APDs is linear only up to gains of ~ 200 ; to be able to efficiently detect single photons, the de-

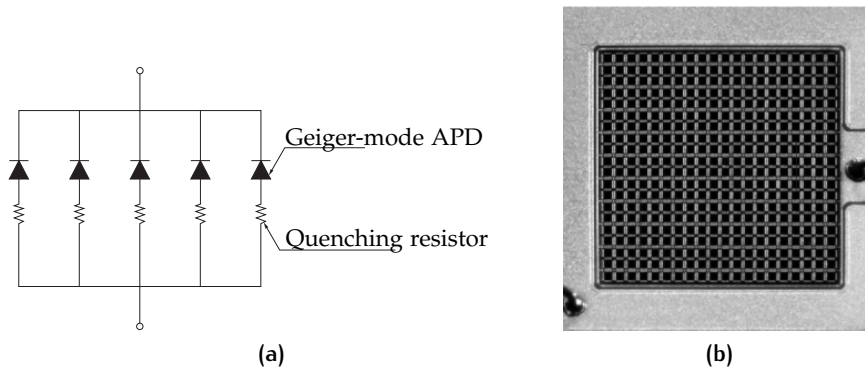


Figure 1.7.: (a) Schematic showing the circuitual structure of a SiPM, made by the parallel connection of many APDs each connected to a quenching resistor and (b) optical micrograph of a SiPM pixel containing 400 APDs (dark squares). The bias lines and quenching resistors are in the spaces between APDs, and constitute a “dead area” for the device. Both images adapted from [35].

vice must be operated in *Geiger mode*, where the gain can be as high as $\sim 10^8$ [14, p. 416]. In this extreme case the APD becomes an on/off device that saturates upon the absorption of any number of photons, completely sacrificing any dynamic range.

1.3.3 Silicon photomultipliers

An extension of avalanche photodiodes that combines high sensitivity with sufficiently high dynamic range is represented by *silicon photomultipliers* or *SiPMs* (sometimes also called *multi pixel photon counters* or *MPPCs*), a relatively recent technology [33, 34]. These photodetectors consist of dense arrays containing many ($\sim 10^2 - 10^4$) small APD cells operated in Geiger mode and in parallel connection, as shown in Fig. 1.7a, so that the total output signal is the sum of all the cells outputs. When a bunch of photons hits the device, it drives as many cells to saturation, thus producing a signal directly proportional to the number of photons. The response is actually linear only if each and every photon saturates a different cell: for this reason the number of APDs in a SiPM is chosen according to the desired dynamic range of the device. For a SiPM with N cells, the probability p_0 that n photons hit as many cells can be demonstrated to be:

$$p_0(n) = \frac{N!}{(N-n)!N^n} \quad (1.13)$$

If we take for example a SiPM with $N = 1000$, then $p_0(10) = 96\%$, i.e. for 10 incoming photons there is about a 4% probability of non linear response.

A simple APD cell is not sensitive any more to further incoming photons after it saturates: for this reason a *quenching resistor* that brings the cell back to the correct bias condition after the avalanche breakdown is connected in series to each APD cell in a SiPM. The surface occupied by this integrated resistor on the array represent a “dead area” of the SiPM that is not sensitive to light, as shown in Fig. 1.7b. As a figure of merit, the fill factor FF of a SiPM is defined as the ratio between the photosensitive surface (i.e. the sum of the APDs surfaces) and the total surface of the device. Therefore the photon detection efficiency PDE can be expressed as:

$$PDE = FF \cdot \varepsilon_q \cdot p_{\text{avalanche}} \quad (1.14)$$

where ε_q is the quantum efficiency and $p_{\text{avalanche}}$ is the probability that the carriers undergo avalanche multiplication. Since both ε_q and $p_{\text{avalanche}}$ are very high (respectively up to ~ 0.9 and ~ 1), while usually $FF < 0.5$, it is the latter that limits the detection efficiency of these devices. Increasing the density of the cells in a SiPM leads to worse fill factors, there is hence a direct trade-off between detection efficiency and dynamic range. It should be noted that even with these limitations the resulting detection efficiency is higher than that of PMTs, an advantage that together with the reduced size and cost, insensitivity to magnetic fields, etc. explains why SiPMs are becoming more and more popular in instrumentation for high energy physics.

1.4 STATE OF THE ART SCINTILLATION DETECTOR TECHNOLOGIES

In this section some selected state-of-the-art scintillation detector technologies are discussed, chosen only on the basis of their relation to the work presented in the following chapters of this thesis, and without any ambition of completeness with respect to the plethora of technological solutions developed during the long history of scintillation detectors.

1.4.1 Fibres

Clad optical fibres with a scintillating core called *scintillating fibres* (often abbreviated as *SciFi*) have become a mainstream technology in high energy physics [36]. The cladding has a refractive index n_{cl} lower than that of the core n_{cr} , so that a portion of the scintillation light is confined in the core because of *total internal reflection (TIR)*. In

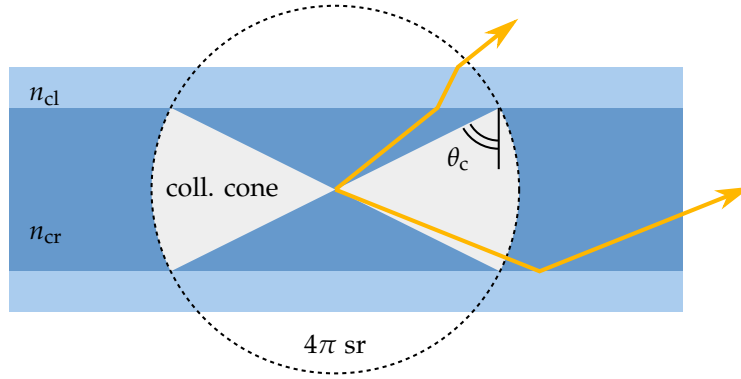


Figure 1.8.: Light collection in a scintillating optical fibre. Scintillation photons are emitted isotropically over the full solid angle, but only the photons with trajectories within the collection cone defined by the critical angle θ_c are confined in the fibre, while the others are lost.

particular, all photons emitted inside the cone defined by the *critical angle*

$$\theta_c = \arcsin \frac{n_{cl}}{n_{cr}} \quad (1.15)$$

which is defined with respect to the normal to the core/cladding interface, are collected and can propagate along the fibre. According to this behaviour, depicted in figure Fig. 1.8, the *collection efficiency* of a fibre can be calculated as the ratio between the solid angle defined by the collection cone and the solid angle of emission, which is the full solid angle since scintillation photons are emitted isotropically:

$$\epsilon_c = \frac{2 \cdot 2\pi (1 - \cos(\frac{\pi}{2} - \theta_c)) \text{ sr}}{4\pi \text{ sr}} = 1 - \cos\left(\frac{\pi}{2} - \theta_c\right) \quad (1.16)$$

Another figure of merit for a scintillating fibre is its *attenuation length*, defined as the distance over which the signal is reduced to $1/e$ of its original value according to the Beer-Lambert law. This quantity depends on both absorption in the core and quality of the core-cladding interface.

Practical scintillating fibres can be made either from inorganic scintillators, e.g. glass doped with Ce^{3+} ($n = 1.56$) and clad with a low refractive index glass ($n = 1.47$) [37] or organic scintillators, typically polystyrene ($n = 1.59$) clad with polymethyl methacrylate ($n = 1.49$) [14, p. 417]. In such fibres collection efficiencies are of $\sim 5 - 10\%$, while attenuation lengths are of the order of ~ 1 m. Typical diameters are of $0.5 - 1$ mm, but in recent detectors plastic fibres with diameters down to $250 \mu\text{m}$ are used [38]. Considering that ~ 2000 photons/mm are generated by a MIP passing through a scintillating fibre [14, p. 417] and given these typical efficiency figures, one can verify that only a few photons can reach the end of a fibre, which is why very efficient photodetectors are needed in SciFi detec-

tors. Scintillating fibres are usually assembled in bundles or planes in order to obtain segmented detection volumes that can reconstruct the tracks of particles passing through. A typical arrangement is the so called *u-v stereo* geometry, where two sets of planar fibre bundles (the *u*-planes and the *v*-planes) are arranged at an angle in several layers (intrinsically giving a third coordinate), so that the trajectory can be reconstructed from the sampled (u, v, z) passage points.

The state of the art in fibre-based detectors is well represented by the upgrade of the LHCb experiment at CERN with a new SciFi tracker [38, 39], ongoing at the time of this writing and expected to become operational in 2018 [40]. The detector is divided in three stations each containing four planes of fibre “mats” oriented along three directions (*x-u-v-x* stereo geometry). Each of the 10-12 mats (500 cm long and 13 cm wide) constituting a plane is made of 6 staggered layers of double-clad scintillating fibres (KURARAY SCSF-78) with a diameter of 250 μm , an average attenuation length of ~ 3 m and a collection efficiency of 5.4%, embedded in epoxy. The fibres are interrupted in the middle of the mat so their length is of about 250 cm. Both ends of a mat are coupled to integrated linear arrays of SiPMs ($PDE \sim 35\%$ at the peak emission wavelength of the fibres) which span its whole thickness and have the same pitch as the fibres (125 μm). In this way light from a track spreads over a few pixels and centroiding techniques can be used to push the spatial resolution beyond the pitch limit (which is of $125 \mu\text{m} / \sqrt{12} \sim 36 \mu\text{m}$ rms). An average yield of ~ 12 photoelectrons/MIP was measured (i.e. ~ 2 per each single fibre), and is expected to improve [40].

1.4.2 Capillaries

The use of glass capillaries filled with a liquid scintillator and coupled to photodetectors has been investigated as a technology for scintillation detectors in the past [41, 42], with their high radiation tolerance as the main motivation [29]. The refractive index of the scintillator is higher than that of the glass, so a filled capillary can be seen as a *liquid core* scintillating fibre. Complete prototypes of scintillation trackers based on this concept were demonstrated, in particular in the framework of the RD41 collaboration at CERN [11]. In these devices a segmented detection volume was obtained by packing together large capillaries (diameter in the order of 1 mm) of borosilicate glass and then slowly drawing them at high temperature to reduce their diameter and fuse them into bundles with a hexagonal cross section [43]. To reduce the optical cross-talk between neighbouring capillaries, dark glass rods called *extra mural absorbers* or *EMA* were inserted in a fraction of the inter-capillary spaces during fabrication.

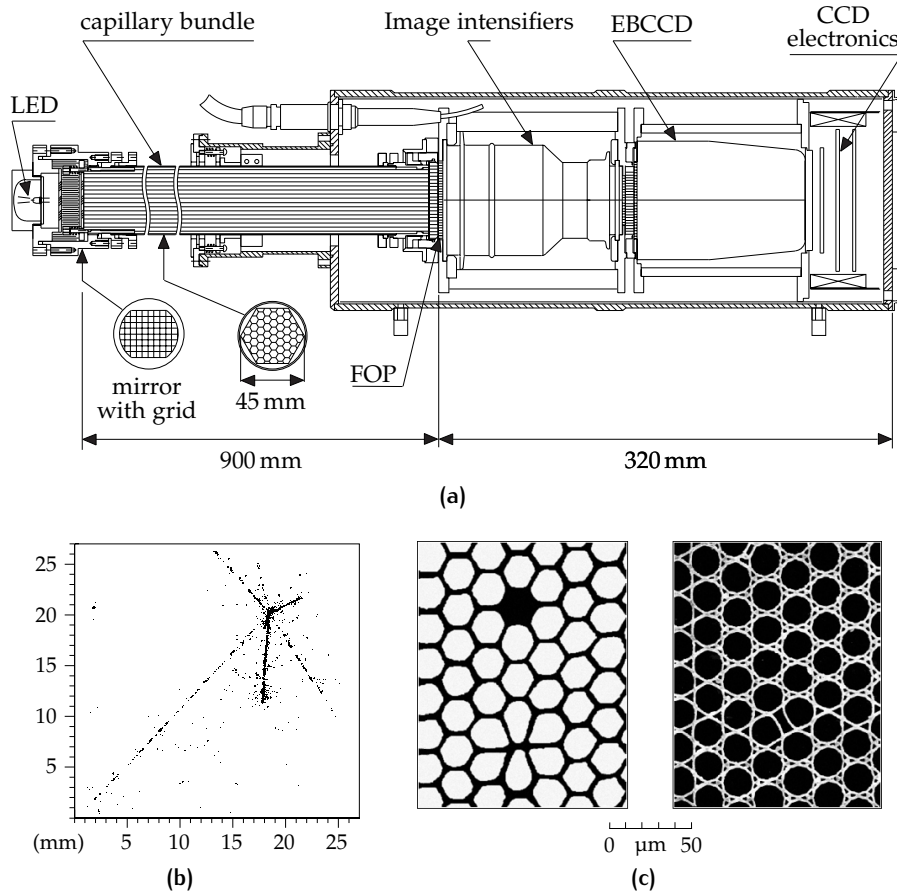


Figure 1.9.: Prototype detector based on capillaries filled with liquid scintillator developed by the CERN RD46 collaboration [11]. (a) Scheme of the detector, featuring a large size bundle of $\sim 10^6$ capillaries. (b) Neutrino interaction event recorded by the detector. (c) Micrographs of the cross section of capillary arrays (areas with defects selected).

Several bundles were then packed together and a second drawing at high temperature was performed to fuse them together into layer elements, each containing many very small capillaries with an inner diameter of $20 - 30 \mu\text{m}$ and a wall thickness of $\sim 3 \mu\text{m}$. The complete detection volume were assembled from several layers, each constructed by glueing together such layer elements. The largest implementation, depicted in Fig. 1.9a, features about 10^6 capillaries with a length of 90 cm, coupled at one end to an optoelectronic readout system composed by image intensifiers cascaded with a CCD, to produce a “picture” of the scintillation events from all the capillaries at the same time.

The borofloat glass capillaries ($n = 1.49$) were filled with a custom liquid scintillator based on methyl naphthalene ($n = 1.62$) [41, 43], resulting in a large collection efficiency. Attenuation lengths up to $\sim 3 \text{ m}$ were measured in capillaries with an inner diameter of $20 \mu\text{m}$ [11], indicating an excellent optical quality of the liquid/glass inter-

face. Good experimental results in tests with cosmic rays and muon neutrino beams were obtained, demonstrating high resolution and low noise measurements of particle tracks (see Fig. 1.9b). The main disadvantages of these detectors are the complexity of the fabrication process, which could result in many imperfections in the geometry of the capillaries (examples shown in see Fig. 1.9c) leading to loss of spatial resolution and non-uniform response, and the difficulties in the management of the liquid scintillator: in particular, the procedure for filling the capillaries was long, complex and required specialised equipment [44].

1.4.3 Microfluidics

A more recent development in the field of detectors using liquid scintillators is represented by the introduction of devices based on *microfluidics*, which throughout this work will be referred to as *microfluidic scintillation detectors* or *MSDs*. The first proof-of-concept prototypes of MSDs consisted of a single microfluidic channel featuring a serpentine geometry, fabricated by photolithography of SU-8 resin on a silicon wafer [45, 46, 12]. The walls of the microchannel were gold coated, so that the serpentine geometry defined an array of parallel, optically-independent mirror light guides. The microchannels were closed by mechanically clamping an aluminium coated Mylar foil to the top of the device, so that they could be filled with a liquid scintillator. In this way the light produced in the liquid would propagate along the channel until the side of the device, left uncoated in order for photons to be transmitted through the transparent resin wall and be captured by the corresponding pixel of a multi-anode photomultiplier tube coupled to the side of the device (see Fig. 1.10).

A small microchannel pitch (down to 60 μm in the detection zone) and an average light yield of 1.65 photoelectrons/MIP have been demonstrated with such prototypes in experiments using electrons from a ^{90}Sr radioactive source. The main motivation for the study of this technology is the advantage in terms of management of the liquid scintillator allowed by microfluidics: it is in principle easy to pump fresh scintillator in a continuous single channel to completely renew the active material, resulting in a potentially increased radiation resistance. Moreover the microfabrication techniques used for manufacturing microfluidic chips allow more precise control, repeatability and flexibility with respect to the “traditional” fabrication techniques used to fabricate thin glass capillaries. These and further expected advantages, as well as potential applications of microfluidic scintillation detectors, will be addressed in the next chapter.

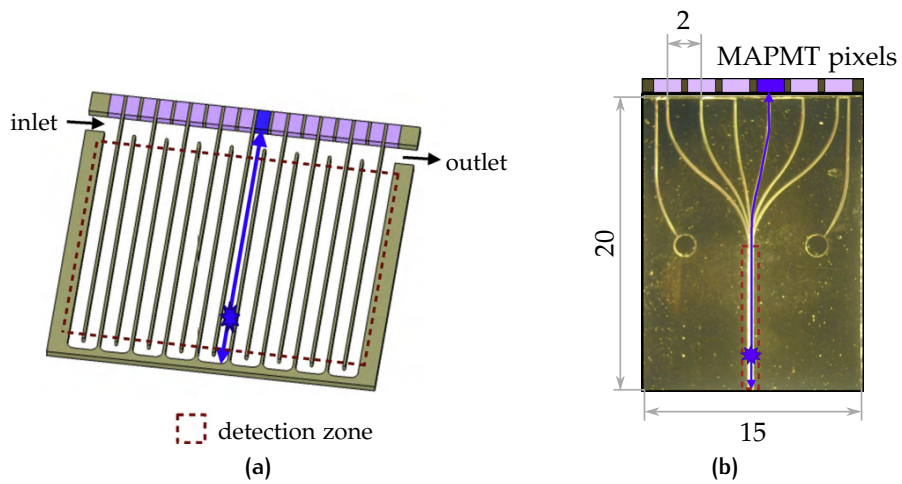


Figure 1.10: (a) Working principle of a microfluidic scintillation detector: the light generated in a microchannel filled with liquid scintillator is guided to a photodetector coupled to the side of the chip. (b) One of the first prototypes, with gold coated microchannels made of SU-8 (dimensions in mm). A “funnel” shaped microchannel array was used to adapt the $60\ \mu\text{m}$ pitch in the detection zone to the 2 mm pitch of the multi-anode PMT (MAPMT) used. Both images adapted from [12].

2 | DESIGN AND MODELING OF MICROFLUIDIC DETECTORS

In this chapter the methodology used for the design of microfluidic scintillation detectors and the results of the modelling of selected case studies are presented. The general motivations and goals driving this thesis are discussed in section 2.1. Section 2.2 treats the basics of light transport in microfluidic channels and presents the simulation methods used. A couple of case studies to which these methods were applied, selected in relation to the fabrication work presented in the next chapters, are discussed in section 2.3.

2.1 MOTIVATION AND GOALS

As anticipated in section 1.4.3, scintillation detectors based on microfluidics promise several interesting characteristics, that would make their use advantageous in certain applications.

Most of the interest comes from the use of a liquid scintillating material. Liquid scintillators are in fact intrinsically less sensitive to radiation damage with respect to their solid counterparts (see section 1.2.3). On top of this, the replacement of the liquid scintillator in a microfluidic detector can in principle be done by relatively easy means, for example by including a pump in the system. This is not the case for detectors based on solid scintillators, because the replacement of the scintillating elements implies possible variations in the geometrical alignments and in the coupling to the photodetectors, affecting the performance. The possibility of replacing the liquid ideally eliminates the ageing of the scintillator from the factors that determine the lifetime of the detector (which would then be dictated by the ageing of the structural materials, of the photodetectors, etc.).

Other advantages are related to the small dimensions obtainable with the fabrication technologies used for the manufacturing of microfluidic scintillation detectors. These could be advantageous in applications where a high spatial resolution (i.e. a fine detector segmentation), or a low *material budget* (i.e. a limited thickness of the detector) are needed. Apart from the smaller dimensions, the direct manufacturing of microchannel arrays can be expected to be more reliable in terms of geometrical precision with respect to the construction of arrays by the assembly of discrete detector elements (in particular for what concerns the mutual alignment of such elements).

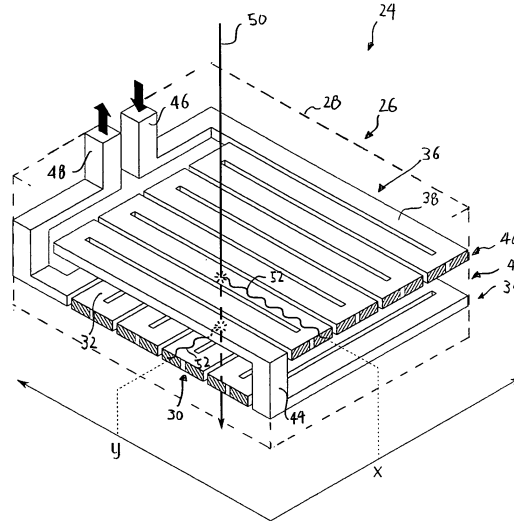


Figure 2.1.: Concept of xy position detection using two layers of microfluidic channels, adapted from [47].

The arrangement of several planes of scintillating fibres in stereo geometry for the reconstruction of particle trajectories was briefly discussed in section 1.4.1. The same concept can be in principle extended to microfluidic scintillation detectors as well, by having planes of microchannels oriented at a different angle. In particular, with two orthogonal layers of microfluidic channels the position of a particle passing through the detector plane can be identified. A possible microchannel design for such a *double layer* device is depicted in Fig. 2.1.

The considerations made in the previous section also apply to double layer MSDs. In particular, both the layers can be obtained from a single microchannel, keeping the possibility of having simple scintillator recirculation. The increased radiation resistance, together with the small thickness obtainable, could be of interest in *beam monitoring* applications. In this case the spatial distribution of the energy deposited by a particle beam passing through the devices would be measured, rather than the position of single particles, with the goal of monitoring beam parameters such its energy, profile and position.

The goal of this work is to study the technological ideas just discussed, i.e. to design and develop microfluidic scintillation detectors with two layers of microchannels, in particular optimising the material budget, and demonstrating the advantages of recirculating the liquid scintillator.

2.2 STUDY OF LIGHT PROPAGATION IN MICROCHANNELS

In a scintillation detector it is desirable to maximise the quantity of light that is transferred to the photodetectors upon scintillation, i.e. the scintillation light has to be *guided* to the photodetector. Practically this is achieved by surrounding the surface of the scintillator with a reflective interface, that prevents light from escaping the scintillator from points not coupled to photodetectors. Either highly reflective metals (e.g. aluminium), white paints (e.g. TiO₂ loaded paints) or polymers (e.g. white polytetrafluoroethylene) are usually applied to the external faces of a scintillating element, or alternatively a low refractive index dielectric material, as is the case for fibres (see section 1.4.1). In the case of microfluidic detectors this aspect can become challenging because, since the scintillator is a liquid, a reflective interface has to be obtained between the liquid and the containment structure, by applying an optical coating on the inner surface of the microchannels. This implies that the chemical compatibility with the liquid scintillators (often aggressive organic solvents) has to be taken into account in the choice of the optical coating.

2.2.1 Simulation method

Simulations of the light transport in microchannels are needed for studying the influence of both the optical coating and the geometry on the performance of the device. Commercial liquid scintillators typically have a light output in the blue region of the visible spectrum, with a maximum emission at $\lambda_0 \sim 420$ nm. This dimension is very small with respect to the characteristic size of the microchannels used in microfluidic scintillation detectors ($\ell \sim 100$ μ m). Since $\ell \gg \lambda_0$, it is possible to use *geometrical optics* to study the propagation of light in the microchannels.¹ A *Monte Carlo* simulation tool to perform such geometrical optics computations in three dimensions was developed. In the tool, scintillation light is modelled as single photons propagating in a 3D space. The optical phenomena considered are absorption in media, and reflection and refraction at interfaces between media. The probabilities of occurrence of such phenomena are modelled respectively using the Beer-Lambert law and the *transfer matrix method* (TMM). The TMM approach allows to model both dielectric materials

¹ Moreover using other approaches, such as finite element simulators implementing beam propagation methods, would result in excessive computational complexity as the large number of propagation modes in a microchannel ($\sim \frac{\pi}{4} \left(\frac{2d}{\lambda_0}\right)^2 \sim 712\,380$, see [48, pp. 258-259]) would require a meshing of the device geometry comparable with the wavelength.

(using a real refractive index) and metals (using a complex refractive index). Interference effects in thin films, such as the optical coatings used in the microfluidic channels, are kept into account by the TMM as well. A more detailed explanation of the inner calculation mechanisms and models used by the simulator are given in appendix A.

2.2.2 Evaluation of optical coatings

The optical behaviour of several materials was simulated to choose an optical coating for the microchannels. In particular, the ELJEN TECHNOLOGY EJ-305 liquid scintillator (peak emission wavelength $\lambda_0 = 425$ nm, refractive index at peak emission $n = 1.505$, attenuation length ~ 3 m) was considered as the emitting medium, while silicon ($n = 5.04 + 1.5j$ at λ_0) was considered as the base material for the microchannels. The reflectivity of the coated silicon surface for photons emitted by the scintillator (depending by the photons incidence angle, the thickness and the refractive index of the coating) was then calculated for several materials via the transfer matrix method. Among the metallic coatings studied, chosen with respect to the available technologies for their deposition, aluminium ($n = 0.56 + 5.15j$) was found to yield the highest reflectivity, close to 90% for any incidence angle. As a comparison, the value for gold is close to 60%. For what concerns dielectrics, transparent fluoropolymers such as Teflon AF [49] ($n \sim 1.31$) or transparent acrylic polymers such as the optical adhesive NOA1375 [50] ($n \sim 1.38$) were considered, in relation to their very low refractive index with respect to that of the liquid scintillator, which leads to relatively small values for the TIR critical angle ($\sim 62^\circ$ for the EJ-305/Teflon AF interface).

It should be noted that the behaviour of metallic and dielectric coatings as reflectors is fundamentally different in which the formers can be highly efficient at any incident angle (see Fig. 2.2a), while the latter are (ideally) perfectly efficient for angles greater than the critical one but inefficient (transmissive) for all other angles (see Fig. 2.2b). Another difference concerns the coating thickness necessary to yield an efficient reflection. Very thin films (few tens of nanometres) are sufficient in the case of metallic coatings, while much thicker films (few microns) are needed for dielectric coatings, because of their transparency. These behaviours are shown in Fig. 2.3. In terms of ease of fabrication, this factor favours metallic coatings, as the conformal deposition of thick coatings on microchannels is technologically challenging (see section 3.4).

Monte Carlo simulations of the light propagation in coated microfluidic channels were performed to evaluate the different effect of the optical coatings on the performance of the devices. In particu-

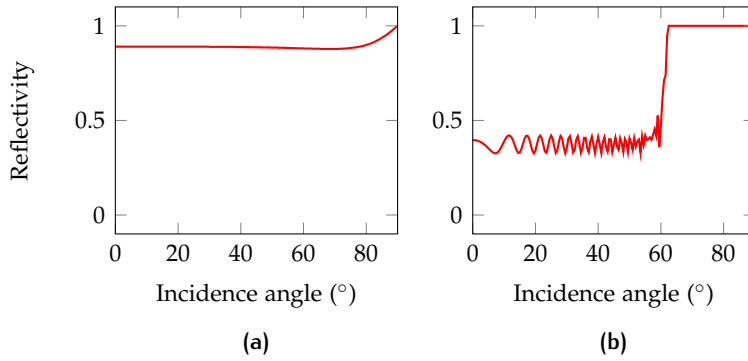


Figure 2.2.: Reflectivity (calculated by the TMM) for 425 nm light propagating in EJ-305 scintillator and impinging at on silicon coated with (a) a 50 nm thick aluminium film and (b) a 5 μm thick Teflon AF film. It can be observed that the behaviour of the metal (specular reflection) is very different with respect to the low refractive index dielectric (exhibiting total internal reflection for angles greater than the critical value of $\sim 62^\circ$). The ripples in the reflectivity of Teflon are due to interference effect and to the presence of silicon underneath the film.

lar the transport efficiency for photons emitted inside microchannels with rectangular cross sections, at different distances from an ideal photodetector placed at one end of the microchannel, was simulated. A representative result is reported in Fig. 2.4, which highlights very different behaviours for metallic and dielectric coatings. In fact, with metallic coatings the signal decays very rapidly with distance, especially in narrow microchannels (while they can be highly efficient for very short distances in large channels). On the contrary, with low- n dielectric coatings the transport efficiency is almost independent from both the distance and the microchannel cross-section. These opposite behaviours are explained by the different reflectivity profiles calculated in Fig. 2.2. Assuming a reflectivity ρ , the probability of still having a photon after N reflections can be estimated as ρ^N . In metals we have $\rho < 1$, meaning the probability decays very rapidly with N (N increases with distance and with decreasing microchannel cross section). On the other hand, in dielectrics we have $\rho = 1$ for photons generated above the critical angle, hence the probability is ideally always unitary (in practice this is not true because of nonidealities such as absorption, surface roughness, etc.), while photons under the critical angle are rapidly lost. Such considerations limit the applicability of metallic coatings to cases where relatively short and/or wide channels are needed, or where the scintillation light production is high enough that the low transport efficiency can be disregarded (as it can be the case in beam monitoring).

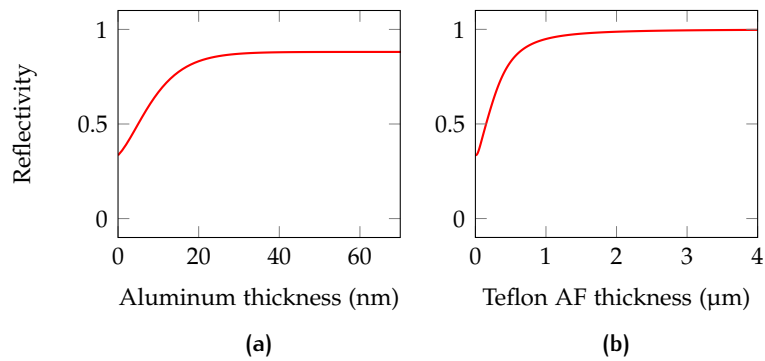


Figure 2.3.: Reflectivity for 425 nm light propagating in EJ-305 scintillator and impinging at 62.1° on (a) an aluminium film deposited on silicon and (b) a Teflon AF film deposited on silicon, as a function of the film thickness. Notice the different scales in the horizontal axes.

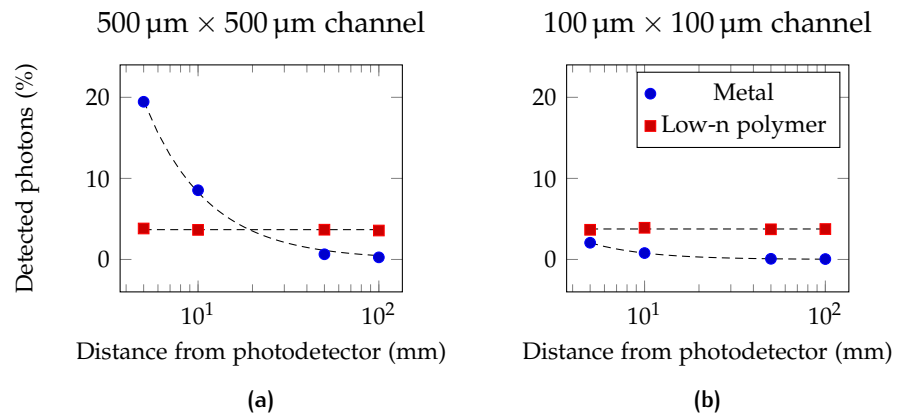


Figure 2.4.: Monte Carlo simulation results (average of three runs with 10^4 photons each) comparing the light transport efficiency of square channels in the case of metallic coating (aluminium, $n = 0.56 + 5.15j$) and polymeric coating (NOA1375 acrylate, $n = 1.37$). EJ-305 liquid scintillator is considered ($n = 1.505$, $\lambda_0 = 425 \text{ nm}$). The dashed lines are power law fits ($r^2 > 0.99$ in all cases).

2.3 CASE STUDIES

In this section the simulations performed for two selected case studies are reported. The purpose of the following discussion is to show the interest of the devices described in chapters 3 and 4, as well as to present the motivations underlying some of the choices (in terms of dimensions, materials, etc.) made in the design and fabrication of such devices.

2.3.1 A thin SU-8 microfluidic scintillation detector

Here the calculations and simulations performed to evaluate the feasibility of a thin microfluidic scintillation detector based on SU-8 resin microchannels, with a Teflon AF optical coating, are reported. These materials and the work performed for the fabrication of such a device are described in chapter 3. The proposed device features an array of 63 microchannels with a cross section of $100 \times 50 \mu\text{m}^2$ and a pitch of $200 \mu\text{m}$. Such width and pitch correspond to those of pixels in some commercial photodetectors (e.g. HAMAMATSU S8865-256 photodiode arrays [51]). EJ-305 is considered as the liquid scintillator for filling the microchannels, and electrons with energies in the MIP range are considered as the excitation particles. The stopping power of the scintillator for electrons was calculated (see Fig. 2.5), and used to estimate the mean energy deposit of electrons in the $50 \mu\text{m}$ scintillator thickness ($\Delta E \sim 6.65 \text{ keV}$). Since the light yield of EJ-305 with respect to electrons is reported to be of around 12 photons per keV [52], an average of 80 photons per scintillation event can be estimated from these figures.² Monte Carlo simulations were performed to study the efficiency of the described microchannels in transporting such scintillation light. The geometry of the whole array is kept into account, to evaluate possible cross-talk effects between the microchannels (see Fig. 2.6a). In the scintillation events treated, a fixed number of photons is emitted with uniform probability over the whole solid angle and propagate in the microchannel array, as shown in Fig. 2.6b. The analysis shows that for the average event about 5 photons over the initial 80 are available to the photodetector at the end of the excited microchannel and that the average crosstalk is acceptable (see Fig. 2.7). Such a device could be used as a thin beam profilometer, similarly to profilometers based on scintillating fibre arrays [53], but with increased radiation hardness and reduced thickness ($\sim 100 \mu\text{m}$

² It should be noted that these calculations neglect the Landau fluctuations of the energy loss in the thin scintillator (see section 1.1.3). Hence although the estimate average is correct, the most probable events would yield less photons.

per microchannel layer, i.e. less than 0.03% of the radiation length calculated for SU-8, $X_0 \sim 350$ mm).

2.3.2 A microfluidic scintillation detector with out-of-plane light output

This section discusses a microfluidic scintillation detector based on silicon microchannels coated with aluminium, in which the channel extremities feature slanted mirror facets that deflect light in the out-of-plane direction, i.e. towards the top part of the device where a locally transparent glass window is present. The interest of such design lies in the possibility of integrating planar photodetectors directly *over* the device (in particular this geometry was studied for the integration of amorphous silicon photodiodes [55, 56, 57]). The processes developed for the fabrication of such devices are reported in section 4.3. A schematic of the model considered in the simulation of such device is shown in Fig. 2.8a (see also Fig. 4.9b for the concept of “out-of-plane” light output). The purpose of this model is to evaluate the efficiency of light transport in such a device, as well as the cross-talk that is present because of the connection between neighbouring microchannels needed for the liquid scintillator circulation. In the model, two ideal photodetector pixels of $950 \times 1000 \mu\text{m}^2$, corresponding respectively to the excited channel and to its neighbour, are placed above the transparent opening located over the slanted mirrors, separated from the liquid scintillator by $100 \mu\text{m}$ of glass. Considering electrons as exciting particles and EJ-305 liquid scintillator, as in the case study discussed in the previous section, an average number of 640 photons per scintillation event can be estimated. In the Monte Carlo simulations performed, scintillation is excited in one microchannel, at a distance of 25 mm from its extremity, and the hits from the guided photons are recorded by the photodetector pixels. Fig. 2.8b shows the hit positions distribution on the pixels surface, which can be used for optimising the design of the pixel shape,³ while the distribution of the number of hits for each pixel is reported in Fig. 2.9. The analysis shows that an average of 3.6 photons hits the pixel corresponding to the excited microchannel, as opposed to an average of 0.5 photons for its neighbour. Notice that in this case the transport efficiency (calculated as the ratio of detected over emitted photons, $3.6/640 \sim 0.56\%$) is much smaller than in the previous case study ($5.16/80 \sim 6.45\%$) because of the lower light guiding performance of aluminium coated microchannels with respect to Teflon AF coated ones (as treated in section 2.2.2). Nonetheless an acceptable light yield is obtained because

³ In particular, areas of the pixel that are not hit by photons, and that therefore contribute more to the dark current than to the signal, can be removed.

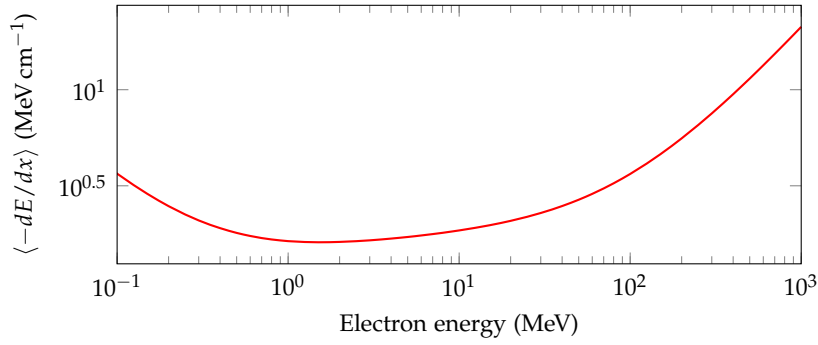


Figure 2.5.: Stopping power for electrons in *pseudocumene*, the main component of the EJ-305 liquid scintillator. Data calculated with *ESTAR* [54] using the pseudocumene weight composition (90% carbon, 10% hydrogen, density: 0.876 g cm^{-3}).

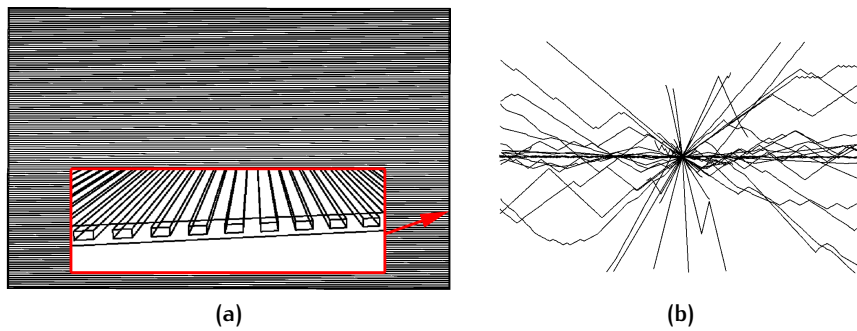


Figure 2.6.: (a) 3D model of an array of 63 SU-8 horizontal microchannels ($100 \times 50 \mu\text{m}$ cross section, 20 mm length, $200 \mu\text{m}$ pitch), coated with Teflon AF and filled with EJ-305. The cross section of the array is visible in the red frame. (b) Monte Carlo simulation of a scintillation event in which 80 photons are produced in the middle of the central channel. The lines represent the photon trajectories seen from the top (the 63 horizontal microchannels are not shown for clarity), while the small traits on the right are the photodetector pixels coupled to the microchannels.

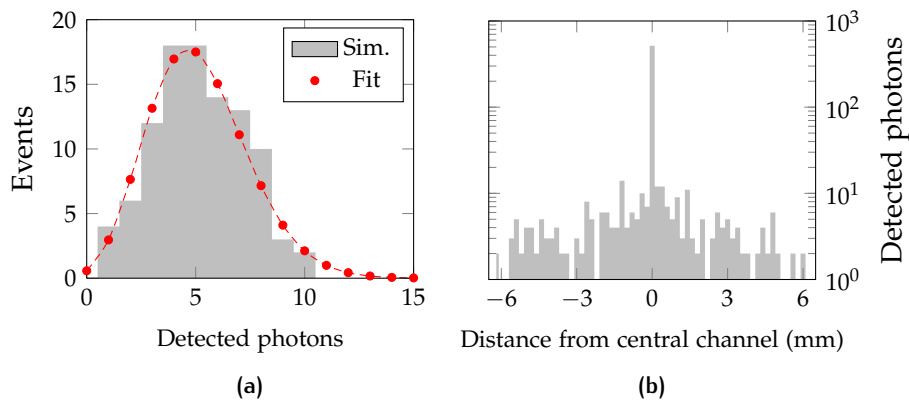


Figure 2.7.: Results of a Monte Carlo simulation of 100 scintillation events of 80 photons each, for the same configuration shown in Fig. 2.6. (a) Photons detected at the end of the central microchannel, fitted with a Poisson distribution ($\mu = 5.16$). (b) Cumulative distribution of the photon detections for all the 100 events in the 63 microchannels, for cross-talk evaluation. The average signal in non excited channels is about two orders of magnitude below that of the central one.

of the deeper microchannels, which yield more scintillation photons.

2.4 CONCLUSIONS AND OUTLOOK

The goal set for this work is the development of microfluidic scintillation detector prototypes to study some of the possibilities offered by such technology, in particular integrating two layers of microchannels, optimising the material budget, and demonstrating the advantages of recirculating the liquid scintillator. The transport of scintillation photons in microfluidic channels was studied, in particular by developing a custom Monte Carlo simulation tool to aid in the design process of such devices. Such tool can be expanded in the future to take into account additional parameters (e.g. surface roughness, modal and chromatic dispersion, particle energy loss fluctuations, ...) or it could be integrated to existing high energy physics simulation software as *Geant4* [58], which as of now has limitations in the treatment of optical photons (notably, thin film effects are not supported [59, pp. 304-311]). The simulations performed on designs based on both thin SU-8 microchannels operating by total internal reflection and large silicon microchannels operating by specular reflection were reported.

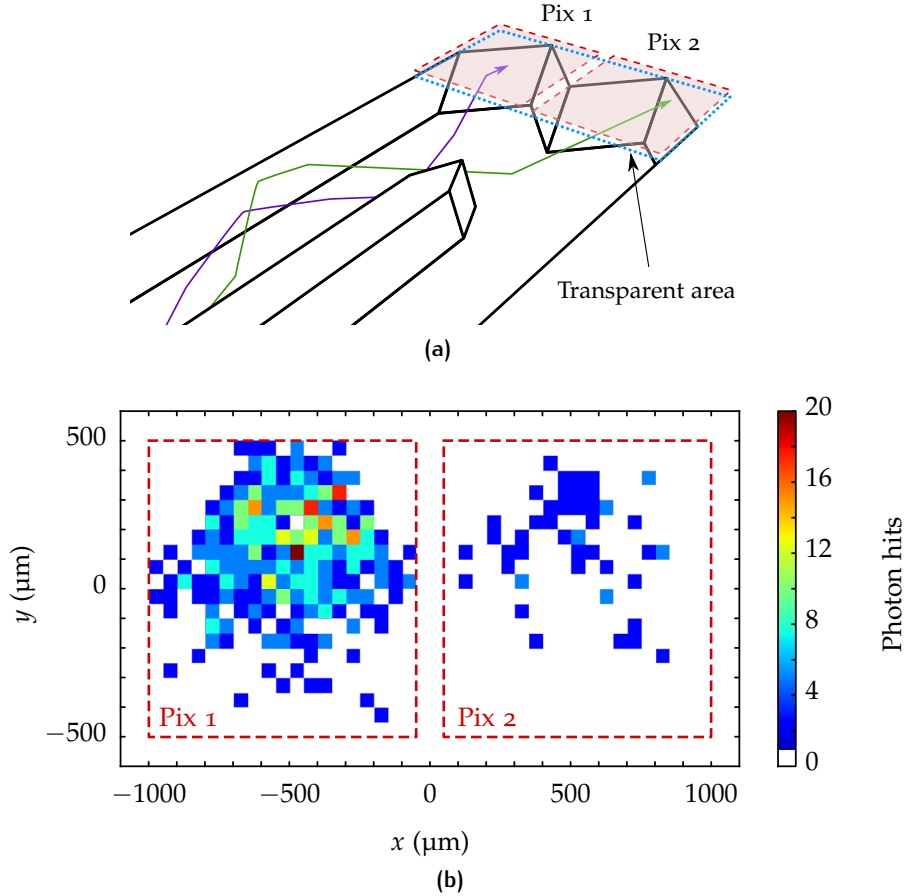


Figure 2.8.: (a) Schematic depiction of the model geometry considered. The microchannels have a cross sections of $850 \times 400 \mu\text{m}^2$, Scintillation photons are generated in microchannel 1, at a distance of 25 mm from the end. The violet arrow shows the possible trajectory of a photon hitting pixel 1 (signal), while the green arrow represents a photon hitting pixel 2 (cross-talk). (b) Result of a Monte Carlo simulations of 100 scintillation events of 640 photons each. The bivariate histogram shows the positional distribution of photon hits in the two pixels.

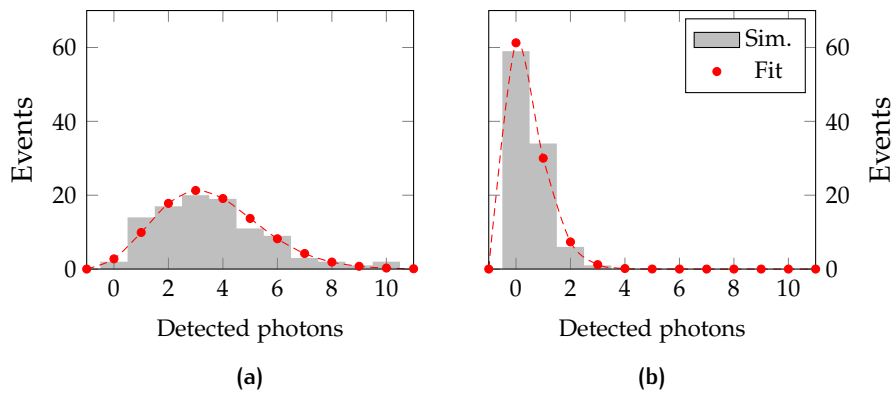


Figure 2.9.: Result of a Monte Carlo simulations of 100 scintillation events of 640 photons each, showing the hits distribution on (a) pixel 1 and (b) pixel 2. The respective Poisson fits have means $\mu_1 = 3.59$ and $\mu_2 = 0.49$ (i.e. the signal on pixel 1 is more than 7 times higher than that of pixel 2, in average).

3

SU-8 MICROFLUIDIC DEVICES FOR SCINTILLATION DETECTION

In this chapter the work performed on microfluidic scintillation detectors based on SU-8 is reported. A brief introduction to the SU-8 photoepoxy is given in section 3.1. The microfabrication processes that were developed for the manufacturing of single and double layer SU-8 microfluidic devices are reported respectively in sections 3.2 and 3.3. Section 3.4 describes the experiments performed for the deposition of optical coatings inside the microchannels. Finally, the validation experiments on the manufactured prototypes are reported in section 3.5.

3.1 THE SU-8 PHOTOEPOXY

SU-8 is a negative-tone resist developed by IBM [60], made by dissolving the EPON SU-8 epoxy resin (produced by SHELL CHEMICAL) in an organic solvent such as *gamma-butyrolactone* or *cyclopentanone*, together with a triaryl sulfonium salt, which acts as the photoinitiator. The name of the resin refers to the epoxide group functionality of 8 present in its base oligomer, shown in Fig. 3.1. Coatings with a wide range of thicknesses (from tens of nanometers to a couple of millimeters) can be obtained by tailoring the viscosity of the mixture and then removing the solvent by heating (*soft bake*). After activation of the photoinitiator by UV exposure (x-rays [61], electrons [62] or protons [63] can be used as well) and a thermal treatment (*post exposure bake*), the resin crosslinks in a dense network where the epoxy functions of the oligomers are bound together. The unexposed parts of the resin, which do not crosslink, can be removed by immersion in a solvent typically *propylene glycol monomethyl ether acetate* (PGMEA), allowing to pattern SU-8. These steps define the process of SU-8 *photolithography*. The resist is widely used in the manufacturing of microsystems, mainly as a polymeric structural material. It exhibits many properties that make it suitable for the microfabrication of particle detectors [64], such as the ability to form structures with high aspect ratios [65], very low surface roughness [66] and high transparency [67] (desirable characteristics when optics are involved, as is the case of this work), a relatively high dielectric strength [68] (useful in devices making use of high electric fields, such as gaseous ioniza-

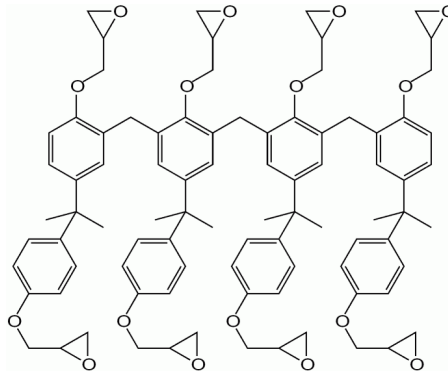


Figure 3.1.: Structural formula of the SU-8 oligomer, featuring 8 epoxy functions. Upon photoactivation the epoxy rings open and bind with epoxy groups of other oligomers to form a highly crosslinked network.

tion detectors) and finally low outgassing [69] (necessary to avoid the pollution of the high vacuum environments in which many detectors work) and a very good radiation tolerance comparable to that of Kapton [70]. The radiation length of crosslinked SU-8 can be estimated using Eq. (1.4) and (1.5) to be $X_0 \sim 350$ mm, i.e. it can be considered a relatively “light” material.

3.2 FABRICATION OF SINGLE LAYER DEVICES

In this section, the microfabrication process developed for the manufacturing of thin SU-8 devices with a single layer of microfluidic channels is detailed.

3.2.1 Preparation of the substrates

Two silicon wafers with a thickness of 380 μm , $\varnothing 100$ mm, boron-doped to a resistivity of 1 – 10 ohm cm and polished on both sides were used as working substrates. A set of alignment marks for the subsequent photolithography and bonding processes were patterned on the backside of the wafers by dry etching (etcher: ALCATEL AMS200), see Fig. 3.2a–f. The use of a single set of marks for all the steps, as opposed to the incremental addition of marks during the process, allows to minimise the alignment errors. Finally (Fig. 3.2g), a 50 nm thick sacrificial film of aluminium was deposited on the front side of the wafers by magnetron DC sputtering (sputterer: BALZERS BAS 450).

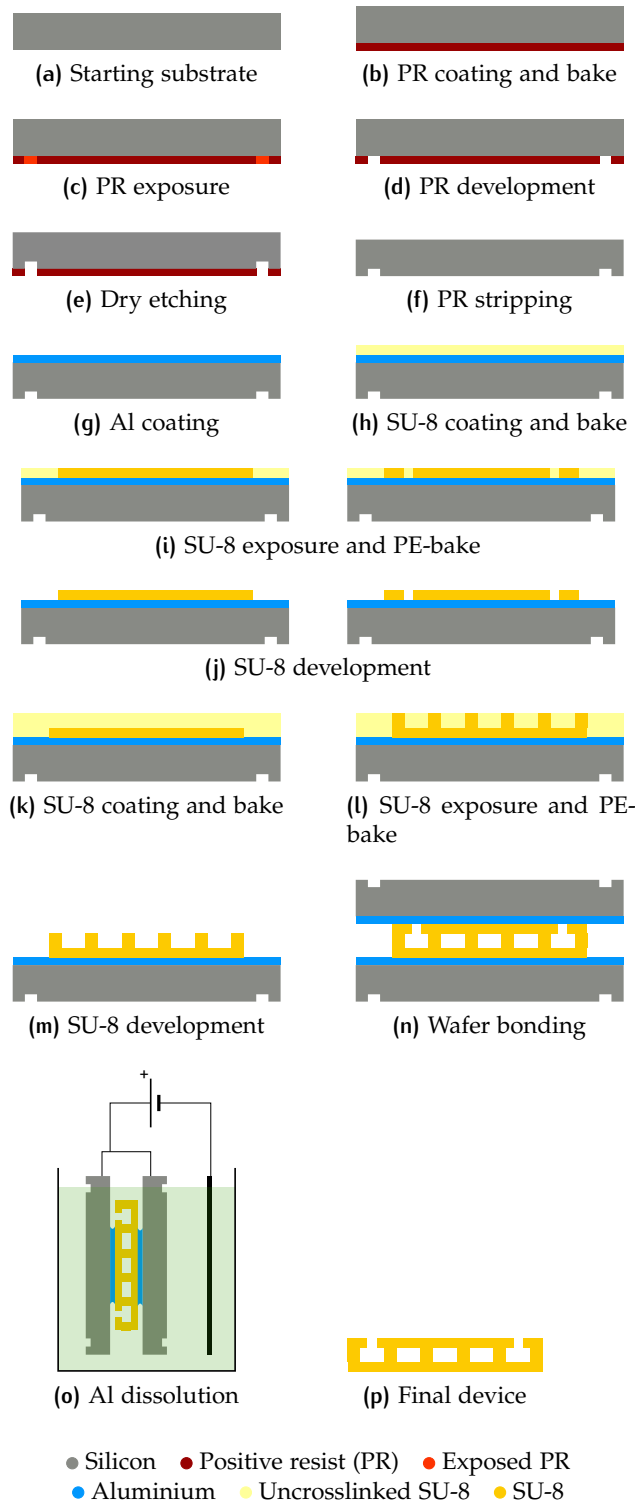


Figure 3.2.: Process developed for the fabrication of free standing, monolithic SU-8 microfluidic devices. Silicon substrates (a) are patterned with alignment marks on the backside (b)–(f). A 50 nm aluminium sacrificial film is deposited on the front side (g). A 30 μm layer of SU-8 is patterned, defining the device bottom part on some wafers and top part on others (h)–(j). A 50 μm layer of SU-8 is patterned over the bottom layer, defining the microchannel array (k)–(m). The two set of wafers are then bonded to assemble the devices (n). Finally, the aluminium film is dissolved and the SU-8 devices are recovered (o)–(p).

3.2.2 Patterning of the first SU-8 layer

A base layer of SU-8 resin (GERSTELTEC GM1070) was spin coated to a thickness of 30 μm (40 s at 2500 RPM using 100 RPM/s acceleration and deceleration rates in a SAWATEC LSM200 coater). After a 10 min reflow time to obtain a more uniform thickness, the resin was soft baked to evaporate the solvent (equipment: SAWATEC HP401Z), bringing the wafers to 120 °C and then again down to room temperature, with heating and cooling rates of 4 °C/min and under a continuous nitrogen flow (Fig. 3.2h).

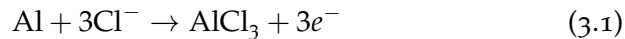
The resin layer was exposed to UV light through a photolithographic mask, aligned to the wafers using the marks previously etched on the backside (aligner: Suss MA6). An exposure dose of 80 mJ cm^{-2} (8 s at an intensity of 10 mW cm^{-2}) was found to be suitable for this SU-8 thickness with the standard mercury-vapour UV photolithography light source used. A mask defining the bottom part of the devices was used for one wafer, while a mask defining the top part of the devices (with the fluidic inlets) was used for the second wafer (Fig. 3.2i). A post-exposure bake to induce crosslinking of exposed SU-8 was performed by heating the wafers, at a rate of ~ 2 °C/min, to 90 °C for 40 min, and then letting them cool down slowly to room temperature. These slow temperature ramps were found to avoid the build-up of stress in the resin. The wafers were developed by immersion in a PGMEA bath for 3 min with mild agitation, dissolving uncrosslinked SU-8 (Fig. 3.2j). Direct drying under an air flow after rinsing with clean PGMEA, without performing the typical rinsing step in isopropyl alcohol, was found to eliminate any problem of bad adhesion of SU-8 to the substrates.

3.2.3 Patterning of the second SU-8 layer

A second layer of SU-8 resin was spin coated to a thickness of 50 μm (40 s at 1700 RPM) on top of the wafer with the bottom part of the devices Fig. 3.2k. In particular, this layer was patterned to define the array of microfluidic channels Fig. 3.2l–m. The processing occurred in the same way as the first layer except for the higher exposure dose (120 mJ cm^{-2}) and longer development time (5 min), because of the additional thickness. The photolithography parameters were found to be important for the success of the subsequent steps, as having overly crosslinked or stressed SU-8 layers would result in respectively bonding failure or warped structures after release. Moreover such choice of parameters allowed to reduce the overall processing time because wafers with different layers could be conveniently grouped in batches sharing the same bake conditions.

3.2.4 Wafer bonding and device release

The two wafers were aligned using the marks on the backside (aligner: Suss BA6) then bond together to assemble the devices (Fig. 3.2n), by applying a pressure of 4 bars at a temperature of 125 °C for 90 min. The pressure allows an intimate contact between the SU-8 surfaces and, since the temperature is higher than that of the post-exposure bake, further crosslinking of the resin occurs, in particular across the interface, resulting in the bonding of the two parts. In order to release the devices, a process based on the anodic dissolution of the aluminium sacrificial film [71] was used. The bonded wafer sandwich was put in a NaCl solution, and a bias of 1 V was applied between the backside of the wafers and other platinum-coated wafers in the solution constituting the counter electrodes (Fig. 3.2o). Since the p-doped wafers used are conductive, the bias is transferred to the aluminium layer, which dissolves in the solution according to the reaction:



for which the activation potential is given by the applied bias. Once the aluminium sacrificial layer was completely dissolved the devices were recovered from the solution, rinsed in deionised water to remove the salt and dried (Fig. 3.2p). Thus, free-standing monolithic SU-8 microfluidic devices with a total thickness of 110 µm (50 µm deep channels sandwiched between two 30 µm layers) were obtained. It should be noted that, upon suitable cleaning, the silicon substrates with the etched alignment marks can be reused.

3.3 FABRICATION OF DOUBLE LAYER DEVICES

Devices with two embedded layers of microfluidic channels were also fabricated [64]. The process developed to this effect extends the one used for the single layer devices introducing an additional wafer, sacrificial film, bonding and release step.

3.3.1 Substrates preparation

Three silicon wafers of the same type and with the same alignment marks described in section 3.2 were used (Fig. 3.3a)]. However in this case a 50 nm thick chromium sacrificial film was deposited on the first wafer, while 50 nm of aluminium were used for the other two (Fig. 3.3b).

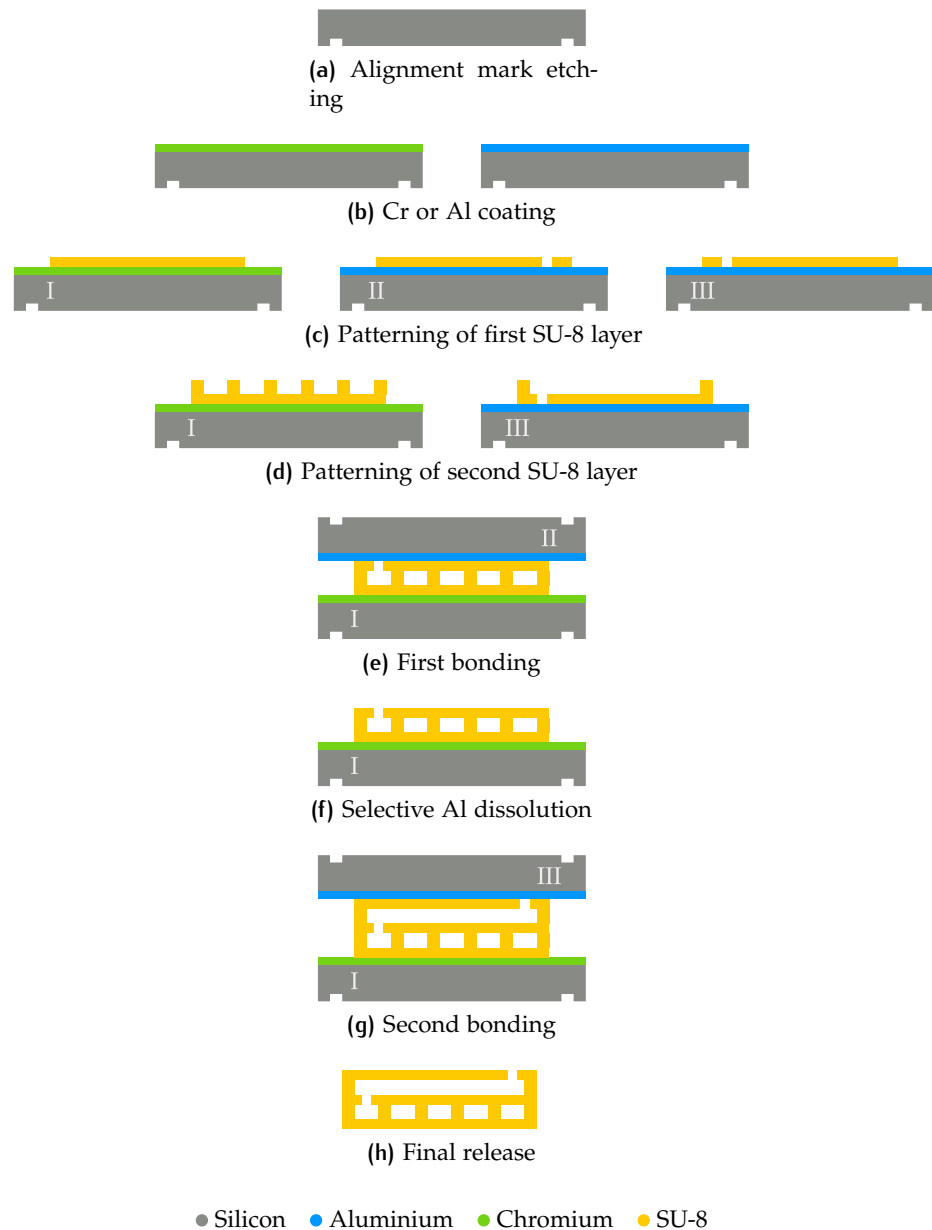


Figure 3.3.: Process developed for the fabrication of SU-8 devices with two embedded microchannel layers (intermediate photolithographic steps not shown). Three wafers with alignment marks etched on the backside (a) are used, here identified with Roman numerals to avoid confusion. 50 nm thick sacrificial layers of Cr and Al are sputtered respectively on one and two wafers (b). A 30 μm layer of SU-8 is patterned on the three wafers, defining respectively the bottom (I), middle (II) and top (III) part of the devices (c). A second, 50 μm thick SU-8 layer is patterned on the top and bottom wafers to define the microchannels (d). The bottom and middle parts are bonded together, closing the first microchannel layer (e). The Al sacrificial layer is selectively dissolved (f) so that a second bonding process to complete the device assembly can be performed (g). Finally, all the sacrificial layers are dissolved to release the devices (h).

3.3.2 Patterning of the first SU-8 layer

A first layer of SU-8 with a thickness of 30 μm was patterned on every wafer with the same photolithography parameters described in section 3.2. In particular, the bottom part of the devices were patterned over the chromium sacrificial film, while the top part (containing the fluidic inlets) and the middle part (containing the fluidic vias connecting the two microchannel layers) were patterned over the aluminium sacrificial films (Fig. 3.3c).

3.3.3 Patterning of the second SU-8 layer

A second SU-8 layer with a thickness of 50 μm was patterned on the wafers with the bottom part and top parts of the devices, to define respectively the first and the second layers of microfluidic channels (Fig. 3.3d). The same process parameters described earlier were used (see section 3.2). Given the increased number of wafers, the shared processing conditions for the different layers proved even more convenient to reduce the fabrication time.

3.3.4 First wafer bonding and selective release

A first bonding process was performed between the wafers with respectively the bottom and the middle part of the devices (Fig. 3.3e). The same alignment method and bonding parameters described in section 3.2.4 were used. The bonded wafer sandwich was then put in a room temperature bath of MERCK AZ400K, a commercial developer for positive photoresists, used in this case as a low concentration KOH solution in order to selectively dissolve the aluminium sacrificial layer, thus releasing the middle layer from its carrier wafer. A mild but continuous ultrasonic agitation was used to remove the hydrogen bubbles forming at the reaction interface, which could otherwise slow down or stop the dissolution. In this way a chromium-coated silicon substrate carrying embedded microfluidic channels made by three-layers of SU-8 was obtained (Fig. 3.3f).

3.3.5 Final bonding and device release

A further full wafer alignment and bonding step was performed to assemble the top part, thus forming the second microfluidics layer and completing the devices (Fig. 3.3g). In this case the bonding temperature was raised to 155 $^{\circ}\text{C}$ in order to keep into account the increased crosslinking of SU-8 induced in the first three layers by the previous bonding process. This temperature is also sufficient to thermally acti-

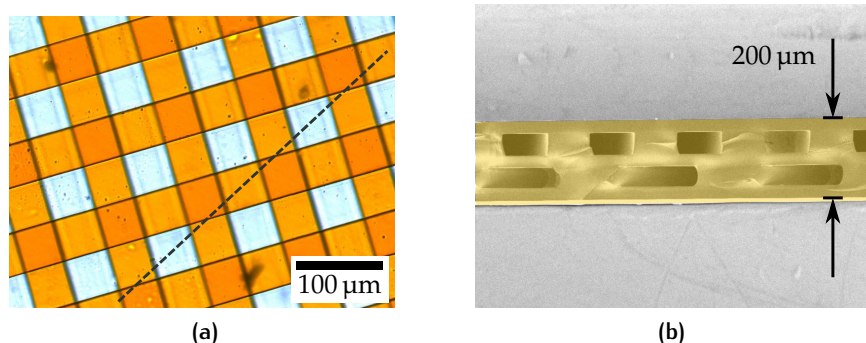


Figure 3.4.: (a) Optical micrograph of a SU-8 device filled with a colorant to highlight the two layers of orthogonal microfluidic channels. The dashed line indicates the orientation of the cross section observed in the colourized SEM image (b).

vate any unreacted photoinitiator molecule that may still be present, so that the resin is fully polymerised and crosslinked at the end of the process. The devices were finally released by dissolving both the aluminium and chromium sacrificial layers by putting the wafer sandwich in a 34% HCl solution, then rinsed with deionised water and dried (Fig. 3.3h). This process allowed to obtain 200 μm thick ($\sim 0.06\%X_0$), free-standing, monolithic SU-8 chips with two embedded layers of microfluidic channels (Fig. 3.4).

3.4 OPTICAL COATING EXPERIMENTS

Although SU-8 has good optical properties in terms of transparency and surface quality, its refractive index is rather high. At the wavelength of peak emission of most commercial liquid scintillators, $\lambda = 425 \text{ nm}$ (i.e. blue light), SU-8 has a refractive index of about 1.6, while the liquids themselves range from 1.51 to 1.57. This means that an SU-8 microchannel filled with a commercial liquid scintillator does not behave as a light guide, as there cannot be any total internal reflection. Experiments to coat the inner surface of the microchannels with a low-refractive index material were done [72, 73].

3.4.1 Materials and methods

The amorphous fluoropolymer *Teflon AF* (copolymer of tetrafluoroethylene and 2,2-bis(trifluoromethyl)-4,5-difluoro-1,3-dioxole [74]) was selected because several properties make it interesting for this application. It has the lowest refractive index of any known polymer ($n \sim 1.31$), an excellent optical clarity (transmission higher than 95% in the visible range), extreme chemical resistance (compatible with

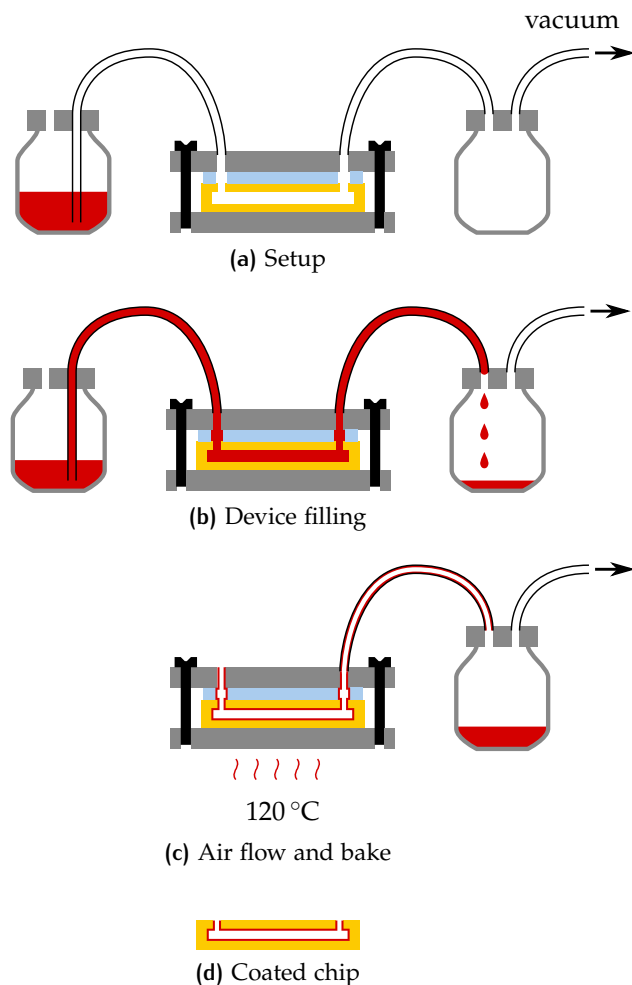


Figure 3.5.: Procedure used for the microchannel coating experiments.

virtually any chemistry except for few fluorinated solvents) [49] and its use as a cladding in optofluidic waveguides is reported in literature [75, 76]. Other fluoropolymers such as *FEP* (*Fluorinated Ethylene Propylene*, a copolymer of hexafluoropropylene and tetrafluoroethylene [77]) or *PEA* (*PerFluoroAlkoxy*, a copolymer of tetrafluoroethylene and perfluoroether [78]), have somewhat similar characteristics. A commercial solution of Teflon AF polymer dissolved in a fluorinated solvent was selected for the coating (solution 601S2-100-6 by DUPONT [79], consisting in grade 1600 Teflon AF, i.e. with a T_g of 160 °C and 65 mol% dioxole, dissolved in Fluorinert FC-40 by 3M, a perfluoroalkylamine solvent). One inlet of the SU-8 microfluidic devices was connected to a reservoir filled with the coating solution, while the other inlet was connected to a vacuum pump via a sealed container to recover the liquid, as shown in Fig. 3.5a. After filling the devices (Fig. 3.5b), the excess solution was removed by disconnecting the solution reservoir and letting air flow through the microchannel. In this way only a thin layer of solution wetting the inner surface of the mi-

crochannel is left. The devices were heated to 120 °C for 20 min while maintaining the air flow (Fig. 3.5c), in order to make the solvents evaporate and obtain a dry layer of Teflon AF that coats the inner surface of microchannel (Fig. 3.5d). In order to observe the section of the coated microchannels, the SU-8 chips were frozen by dipping them in liquid nitrogen, then cleaved with tweezers. A thin (20 nm) carbon layer was finally evaporated on the surface of the samples to allow observation with a scanning electron microscope.

3.4.2 Results

The coating process proved very challenging to control for several reasons. A first difficulty is given by the high viscosity of the commercial polymer solution (~ 82 cP [74]), which made the filling of the chips a very lengthy operation, which often lead to the delamination of the bonding interface because of the high pressure drop needed to make it flow in the narrow microchannels. This problem was addressed by further diluting the solution with perfluorohexane, in weight ratios up to 50%. A second difficulty is given by the surface tension of the solution which, albeit low, is sufficient to cause the accumulation of the liquid in the corners of the microchannels, leading to a inhomogeneous coating thickness. It was observed that the thickness of the coating would reach 2 – 3 μm in the corners and gradually decrease to $\sim 200 - 300$ nm in the central part of the microchannels (Fig. 3.6). In average, these values are below the minimum required thickness ($\sim 3 - 4$ μm) that was calculated to be necessary for a Teflon AF optical cladding (see section 2.2.2, and Fig. 2.3 in particular). Multiple coating steps to increment the thickness of the coating were attempted, but no significant changes in the final result were observed: it is believed that during the injection phase the solvent in the coating solution readily dissolves the previous thin coating, and thus the final thickness is not affected. Moreover other defects could occasionally be observed, such as pinholes in the coating or the formation of polymer clusters on the surfaces. All these difficulties in the control of the coating process eventually led to its abandonment.

3.5 EXPERIMENTAL VALIDATION

Validation experiments with SU-8 devices filled with a high refractive index fluorescent solution were performed as follows. SU-8 microchannel arrays with a length of 20 mm were manufactured according to the fabrication process described in section 3.2. Arrays with pitches of both 0.8 mm (16 channels, 12.5 mm array width) and

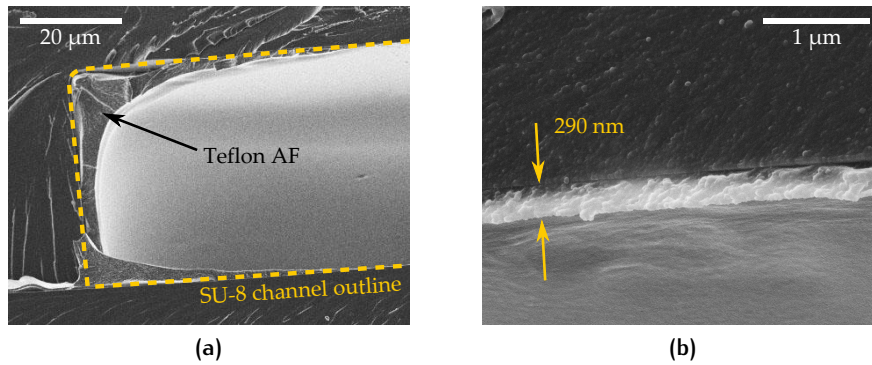


Figure 3.6.: SEM micrographs of coated microchannel cross sections. The polymer was observed to accumulate near the corners of the microchannels (a), then become increasingly thinner until the central part of the channel (b), where the thickness is only of few hundreds of nm.

0.2 mm (64 channels, 12.7 mm array width) were fabricated, in order to match the pixels of the photodiode arrays used for the light detection (respectively HAMAMATSU S8866-128-02 and HAMAMATSU S8865-256 [51]). A high refractive index fluorescent liquid was prepared by dissolving rhodamine 6G in methylene diiodide ($n = 1.74$ [80]). The SU-8 devices were filled by simply depositing a droplet of the solution on one inlet and letting the liquid crawl into the microchannels by capillary action. The filling occurred in few tens of seconds because of the small internal volume of the devices, which is less than 15 μL . One side of the devices was coupled to the photodiode arrays (as depicted in Fig. 3.7a) by means of a mechanical holder, and put in a dark box. Light from a green LED was shined on the chips to excite the fluorescence of rhodamine 6G, and the output light from the microchannels was measured with the photodiodes. Results for both empty microchannels and microchannels filled with the liquid are reported in Fig. 3.7b, showing that the light produced by fluorescence and guided along the microchannels is detected by the photodiodes. These results demonstrate that a microfluidic scintillation detector based on plain SU-8 microchannels is feasible, provided that a scintillator with suitable optical properties is available. To the best of the author's knowledge, no commercial scintillator with a refractive index higher than that of SU-8 ($n = 1.6$) exists, however at least one custom liquid scintillator with a suitable refractive index ($n = 1.62$), based on methyl naphthalene, is reported in literature [41].

3.6 CONCLUSIONS AND OUTLOOK

The SU-8 photoepoxy has many characteristics that make it suitable for the microfabrication of microfluidic scintillation detectors. Pro-

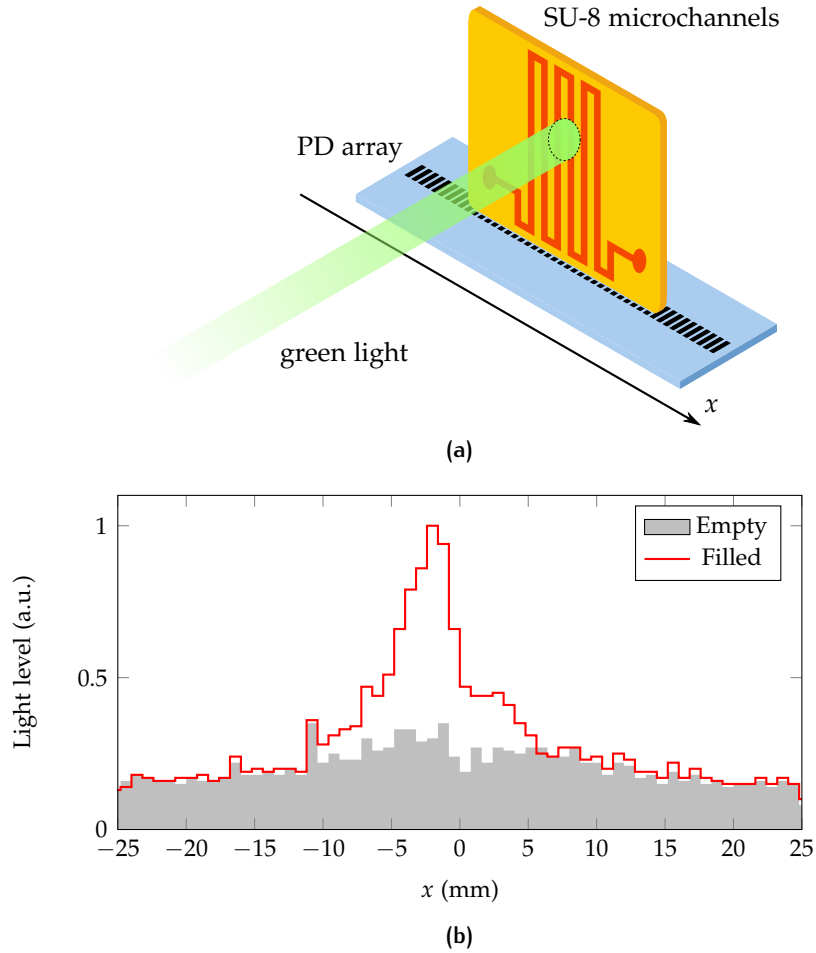


Figure 3.7.: (a) Depiction of the setup for the measurement of the light output from a SU-8 microchannel array. The microchannels had a cross section $100 \times 50 \mu\text{m}^2$ and a length of 20 mm. Both the microchannel array (12.7 mm wide) and the photodiode array (51.2 mm wide) had a pitch of 0.2 mm. The diameter of the light spot on the chip surface was of ~ 4 mm. (b) Experimental results showing the light output from empty microchannels (gray area) and from microchannels filled with a high-refractive index fluorescent dye (red line). In the latter case the additional signal is due to the fluorescent light generated in the liquid and guided along the microchannels.

cesses for the development of SU-8 devices with both one and two layers of microfluidic were developed. Such processes can be extended to the fabrication of multi-layer structures different than channels that can be of interest in microsystem manufacturing. A process for the internal coating of the microchannels based on the injection of Teflon AF polymer solutions was investigated, but the obtention of a sufficient thickness and optical surface quality were found to be challenging. Nonetheless the results obtained could be of interest for non-optical applications, for example the chemical passivation of microfluidic devices. To demonstrate the concept of a microfluidic detector operating by total internal reflection, the experimental validation of an SU-8 device was performed using a fluorescent solution with a high refractive index. To complete such validation and study the device performance (in terms of light yield, crosstalk, efficiency) experiments in which light is excited by high energy particles need to be performed, for example by developing a custom liquid scintillator with high-refractive index to be used with bare SU-8 channels.

4

SILICON MICROFLUIDIC DEVICES FOR SCINTILLATION DETECTION

In this chapter the work performed on microfluidic scintillation detectors based on silicon microchannels is reported. A brief introduction is given in section 4.1. The microfabrication processes that were developed for manufacturing microfluidic devices by dry and wet etching of silicon are presented respectively in section 4.2 and 4.3. The experiments performed with some of these devices are discussed in sections 4.4 and 4.5.

4.1 INTRODUCTION

Several factors make silicon a very interesting material for the fabrication of microfluidic scintillation detectors. Since silicon is a semiconductor, the integration of solid-state devices such as photodetectors and front-end electronics in the same substrate containing the microchannels can be imagined, potentially leading to very compact detector systems. Analogously, the fabrication of microchannels in the same substrate used by silicon pixel detectors [81], providing a scintillation measurement on top of the ionization one, can be imagined. Many established techniques exist for structuring silicon at the microscale [82, 83], leading to a plethora of design possibilities. While SU-8 microchannels were created with an *additive* process, i.e. adding and patterning the material on top of a substrate, a *subtractive* process is necessary in order to create deep microfluidic channels in silicon, i.e. selectively removing material by etching (an approach called *bulk micromachining*). Silicon can be etched using both *dry* methods (gases [84], plasmas [85, 86, 87]) and *wet* methods (liquid etchants [88, 89, 90, 91]). In this work technological solutions relying on both approaches were explored.

4.2 FABRICATION OF DEVICES BY DRY ETCHING

In this section the fabrication of microfluidic scintillation detectors based on silicon microchannels obtained by dry etching is described (see also [92]).

4.2.1 Deep reactive ion etching of silicon

Deep reactive ion etching (DRIE) is a strongly anisotropic dry etching technique, commonly used in microsystems manufacturing to yield structures with vertical sidewalls and high aspect ratios [86]. This technique relies on an alternation of fluorine-based plasmas. In a first phase an etching plasma – typically ionised sulphur hexafluoride (SF_6) – is created in the reactor. Such plasma chemically and physically attacks silicon, prevalently in the vertical direction because of the vertical electric field applied to the chamber that accelerates the gas ions perpendicularly to the surface of the wafer. After a few seconds, the atmosphere of the reactor is switched to a passivating plasma – typically ionised octafluorocyclobutane (C_4F_8) – which results in the deposit of a very thin fluoropolymer layer on the surface, protecting the silicon surface from further etching. In a DRIE process, these two etching and passivation phases are alternated many times until the desired etching depth is reached. Since during the etching phase the attack occurs prevalently in the vertical direction, the polymer layer deposited in the passivation phase is quickly destroyed at the bottom of the silicon trench, which continues to be etched, while it stays on the sidewalls, which are not etched. For this reason the process is overall strongly anisotropic, with the etching occurring almost exclusively along the vertical direction. However, a slight attack of the silicon in the in-plane direction occurs at each etching cycle, finally resulting in a typical undulation along the sidewalls, the so-called *scalloping* [87]. The sidewall of a microchannel exhibiting scalloping after the etching process is shown in Fig. 4.1a. This phenomenon is undesirable in applications involving optics such as the one presented in this work, since the scalloping spatial period (typically in the order of 100 – 400 nm) is comparable to the wavelength of the light emitted by the liquid scintillator (peak emission at 425 nm), resulting in sidewalls that behave as diffraction gratings or diffuse reflectors, and thus degrading the light transport in microchannels. In order to remove scalloping a smoothing process was developed, consisting in the growth of a 3 μm thick SiO_2 layer on the silicon surface by wet oxidation and its subsequent removal by buffered hydrofluoric acid (BHF). Because silicon oxidation is a process limited by the isotropic diffusion of the oxygen coming from the external environment, the shape of the Si/ SiO_2 interface initially matches the scalloping undulation but tends to even out as the thickness of the oxide layer increases, as depicted in Fig. 4.1c. Hence, when the thick oxide layer is removed with BHF, the smooth silicon surface underneath – corresponding to the former Si/ SiO_2 interface – is revealed,

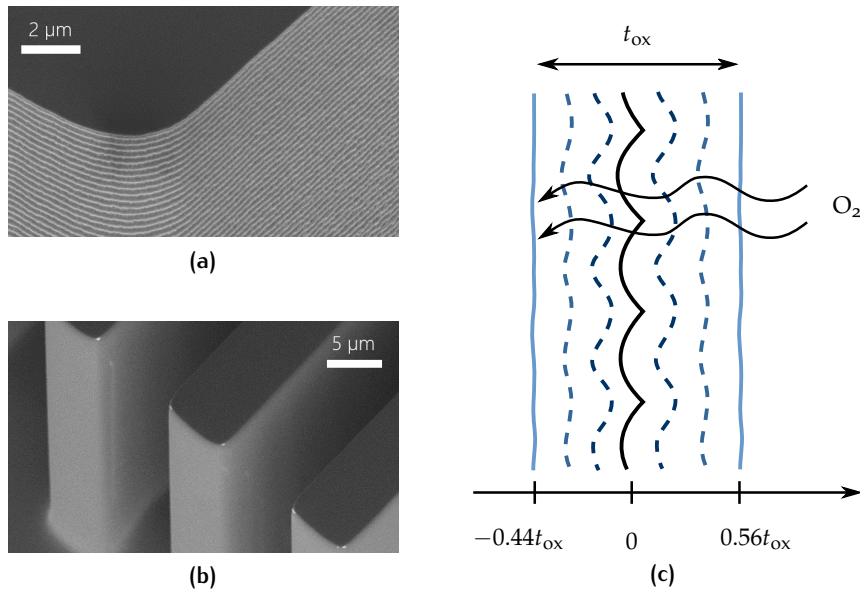


Figure 4.1.: Smoothing of silicon microchannels. (a) SEM micrograph of silicon sidewalls after DRIE, exhibiting scalloping. (b) SEM micrograph showing smooth silicon after removing the oxide with hydrofluoric acid. In the case of this work it was found that $t_{\text{ox}} = 3 \mu\text{m}$ is sufficient to eliminate scalloping with a 300 nm period. (c) schematic depiction of the evolution of the SiO_2 layer during wet oxidation of silicon. The initial silicon surface is located at 0. Silicon reacts with oxygen from the water vapour in the furnace environment, forming silicon oxide. The oxide layer distributes with approximately 44% of its thickness t_{ox} below and 56% over the original surface, because of the higher molar volume of SiO_2 with respect to Si. As the oxidation continues, oxygen must diffuse through the whole SiO_2 layer to reach the silicon surface underneath. The combination of these two effects causes the topography of the Si/ SiO_2 interface (located at $-0.44t_{\text{ox}}$) to become flatter as the oxide thickness increases.

providing a surface suitable for light transport by specular reflections (Fig. 4.1b).

4.2.2 Dry etching of microfluidic channels and inlets

Silicon wafers with a thickness of 380 μm, $\varnothing 100$ mm, polished on both sides, were used as substrates. A layer of SiO_2 with a thickness of 1 – 3 μm (depending on the depth of microchannels to be etched) was grown on the surface of the wafer by wet oxidation. This layer was patterned by dry etching on both the backside – to define alignment marks needed for the subsequent photolithography and bonding steps – and the front side of the wafers, to define a hard mask needed for the dry etching of the microchannel array (Fig. 4.2a). A photoresist layer was spun on the wafer and patterned in such a way as to protect the whole surface except for some openings in correspondence of the fluidic inlets/outlets for the microchannels, then

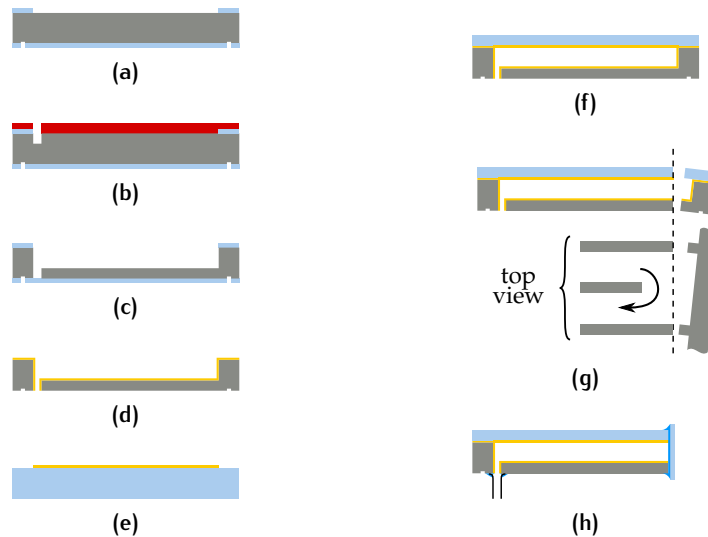


Figure 4.2.: Schematic process flow for the fabrication of dry etched microfluidic channels in silicon. (a) Dry etching of the microchannel pattern in silicon oxide, (b) partial silicon etching in correspondence of fluidic openings through a thick photoresist mask, (c) etching of the microchannels through the oxide hard mask and opening of the fluidic inlets/outlets with a single DRIE process, (d) smoothing of the silicon surface by SiO_2 growth/etching and metallization of the microchannels by Ti/Al sputtering, (e) patterning of Ti/Al reflective stripes on Pyrex cover wafer by lift-off, (f) anodic bonding of Pyrex and silicon wafer to close microchannels, (g) microchannel ends cut open during wafer dicing, in such a way that liquid circulation is still possible and (h) glueing of thin glass window and fluidic connectors.

a DRIE process was used to etch silicon, to a depth corresponding to the difference between the wafer thickness and the microchannel depth desired (Fig. 4.2b). After removing the photoresist with an oxygen plasma attack, the microfluidic channels were etched in the silicon substrate (again by DRIE) through the previously patterned hard mask. During the same etching step the depth of the partially etched pits reaches the backside of the wafer (Fig. 4.2c), thus providing fluidic inlets/outlets for the device once the residual oxide was removed by BHF.

4.2.3 Surface smoothing and optical coating

The smoothing process described in section 4.2.1 was used to remove the scalloping resulting from the etching process. Smooth microfluidic channels with several depths, ranging from 100 to 300 μm were fabricated with this method. Since the reflectivity of a bare silicon surface is relatively low (reflectivity calculated at the emission peak of the liquid scintillator for an average angle: 37.1%), an optical coating is necessary to enhance the light transport in the etched microfluidic channels (see discussion in section 2.2.2). Aluminium was chosen as a coating material because of its high reflectivity (calculated angular av-

erage: 89.3%), and ease of deposition. A 50 nm thick aluminium film was deposited on the whole silicon wafer by conformal DC sputtering – over a 10 nm thick titanium layer to improve adhesion – resulting in a mirror-like microchannel surface (Fig. 4.2d).

4.2.4 Fluidic and optical packaging

In order to close the etched microfluidic channels, the same Ti/Al stack was deposited on a 525 μm thick Pyrex (CORNING 7740) wafer and patterned via a *lift-off* process to obtain reflective metal stripes slightly wider than the microchannels but with the same pitch (Fig. 4.2e); this geometry allows to align and put the wafers in contact in such a way that the metal stripes on the glass completely cover the microchannels. The aluminium/Pyrex contact was exploited to solder the cover wafer and the wafer with the etched microchannels together using anodic bonding [93] (350 °C, 800 V), thus yielding closed microfluidic channels with a mirror-like internal surface. A wafer-to-wafer alignment precision better than 5 μm could be consistently achieved using a Suss BA6 aligner and SB6 bonder. The thickness of the Pyrex wafer was then reduced by mechanical grinding, down to 100 μm (Fig. 4.2f). Since silicon is not transparent, it is necessary to provide to the scintillation light a way out from the microchannels. This was done by aligning the wafer dicing¹ cut lines to the microchannels so that the latter are cut open on one side, but in such a way that it's possible to close them again without preventing the circulation of the liquid, as depicted in Fig. 4.2g. For this purpose, glass stripes (SCHOTT D263) with a thickness of 150 μm were glued with a transparent epoxy resin to the side the chips, providing an optical interface to the microchannels. Metallic connectors were glued directly on silicon in correspondence of the fluidic openings (Fig. 4.2h), providing a simple way to connect tubes to the chip and fill the microchannels with liquid scintillator. An example prototype is pictured in Fig. 4.3a, having a footprint of 20 \times 15 mm² with an active area of about 12 \times 12 mm² (16 such chips fit on a \varnothing 100 mm wafer). Several chips fabricated in this way can be assembled together to make a layered detector, as shown in Fig. 4.3b.

¹ The term *dicing* used throughout the text refers to the process of sawing the wafer to obtain single chips.

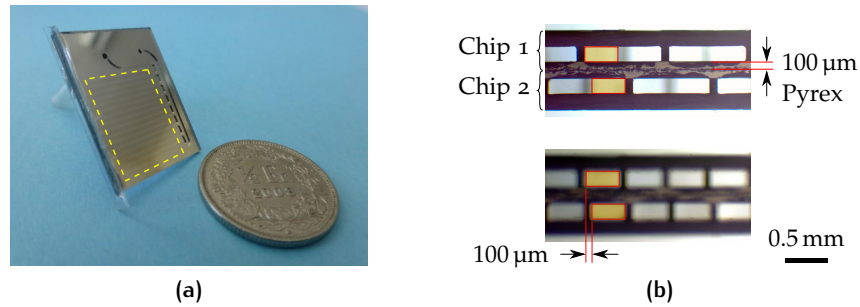


Figure 4.3.: Silicon devices fabricated by dry etching. (a) A $20 \times 15 \text{ mm}^2$ microfluidic chip, next to a 50 cents swiss franc coin for size comparison. The thin glass window can be seen on the left side, while fluidic connectors for filling with the liquid scintillator are glued on the backside. The dashed line indicates the location of the $12 \times 12 \text{ mm}^2$ detection area. (b) Optical micrographs of the cross section of two superimposed chips, showing how the microchannels can be staggered to increase the geometrical coverage of the detector. In the bottom photo the focal plane is in the middle of the microchannel walls terminations, allowing to visualize better the cross section of the microchannels ($400 \times 190 \mu\text{m}^2$ in the imaged chips).

4.3 FABRICATION OF DEVICES BY WET ETCHING

The processes developed for the fabrication of microfluidic scintillation detectors based on anisotropic wet etching of silicon [56, 94, 57] are presented in this section.

4.3.1 Anisotropic wet etching of silicon

Although the deep reactive ion etching technique offers great control and design flexibility for the fabrication of microfluidic channels in silicon, wet etching has some complementary advantages. First of all it is cheaper and allows a greater throughput, as the equipment is less costly and many wafers can be processed at the same time in a shared etching bath, instead of one at a time in a plasma reactor. Moreover both sides of a wafer can be etched at the same time, while only one side at a time can be processed by dry etching; in the case of microfluidic scintillation detectors it is interesting to etch both sides of a wafer to obtain two layers of microfluidic channels which are either at a right angle, to allow two dimensional resolution as discussed before, or staggered with respect to each other to increase the geometrical efficiency of the detector. Another advantage is the possibility of exploiting the anisotropy of some wet etchants with respect to the crystalline lattice of silicon, to obtain particular three-dimensional structures that would be much more difficult to obtain by dry etching. In the case of this work this last characteristic was exploited to obtain slanted mirrors at the end of the microfluidic channels that can deflect the scintillation light in the out-of-plane direction, as will be discussed in section 4.3.5.

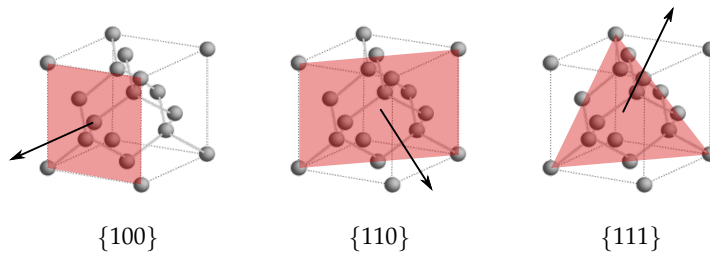


Figure 4.4.: Depiction of the three main crystalline planes that can be identified in the silicon lattice, denoted by their Miller indices. Curly brackets denote the family of all planes that are equivalent with respect to the crystal symmetry (e.g. $\{100\}$), while angular brackets denote the directions normal to such planes (e.g. $\langle 100 \rangle$), here represented by the arrows.

The silicon crystal features a *diamond cubic* structure, in which three main families of planes, denoted with the Miller notation [95] $\{100\}$, $\{110\}$ and $\{111\}$, can be identified (see Fig. 4.4). Atoms on silicon surfaces cut along these planes feature a different number of dangling bonds and thus a different capability of binding the hydroxide ions which result in a direction-dependent etch rate when exposed to an alkaline wet etchant [90]. In particular, the etching rate for $\{111\}$ surfaces is much smaller than those for $\{110\}$ or $\{100\}$ directions. The etch rates also depend on the concentration and the temperature of the solution. Aqueous solutions of KOH (potassium hydroxide) were chosen for wet etching, mainly because of the availability and safety of the process with respect to other alkaline solutions such as TMAH (tetramethylammonium hydroxide) or EDP (ethylenediamine pyrocatechol). Standard $\langle 100 \rangle$ -oriented monocrystalline silicon wafers were used as substrates, i.e. with a surface parallel to the $\{100\}$ planes and a flat cut along to one of the $\langle 110 \rangle$ directions.

4.3.2 Alignment of masks to the silicon crystal

Since the etching anisotropy depends on the lattice orientation, the masks used to define the etch pattern need to be precisely aligned to the silicon crystal. For this purpose the method described in [96] was used as follows. A SiO_2 layer to be used as a hard mask for the wet etching was grown on the wafers by wet oxidation. A particular pattern for the alignment to the crystal is transferred on the wafer via photolithography and dry etching of the oxide. Such alignment pattern consists in two groups of marks, placed on diametrically opposite sides of the wafer. In each group, circular apertures having a diameter of $72\ \mu\text{m}$ are disposed, with an angular pitch of 0.1° , along an arc having a radius of $44\ \text{mm}$ and spanning an angle of 8° . The 0.1° angular pitch defines the precision of the alignment obtained with this method, while the 8° angular width defines a maximum

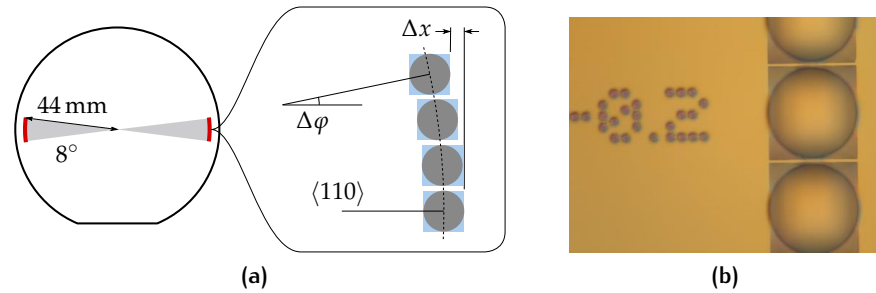


Figure 4.5.: Marks for the alignment to silicon crystal planes. (a) Depiction of the circular openings on the wafer. After the etching the circles yield inverted pyramids with an horizontal offset Δx depending on the angular misalignment $\Delta\varphi$ with respect to the $\langle 110 \rangle$ direction. (b) Micrograph of the mark better aligned with the $\langle 110 \rangle$ direction, identified by the smallest observed shifts with respect to the neighbouring marks. The etched number indicates that a correction of -0.2° needs to be applied with respect to the first alignment.

misalignment of $\pm 4^\circ$ between the mask used to transfer the pattern on the wafer and the horizontal $\langle 110 \rangle$ direction. For each circle, a corresponding mark with a standard “cross” shape is placed on an arc with a radius of 43 mm.

The wafers with such a patterned oxide layer were then immersed in a 40% solution of KOH at 60°C for about 3 h. Because the $\{111\}$ crystalline planes of silicon are attacked very slowly by KOH, the circular apertures in the oxide result in inverse pyramids etched in silicon having a square base with the sides oriented along the $\langle 110 \rangle$ directions. The bases of the pyramids are horizontally shifted with respect to each other of an amount Δx that grows with the angular misalignment $\Delta\varphi$ between their centres and the horizontal $\langle 110 \rangle$ direction (see figure Fig. 4.5a). The wafers are inspected with an optical microscope to locate the pyramid which has the smallest shift with respect to its neighbours, meaning it also has the best angular alignment with respect to the $\langle 110 \rangle$ direction (an example of such mark is shown in Fig. 4.5b). As a practical improvement to the original method, the angular correction with respect to the first alignment is reported every other pyramid on the oxide layer, as well as on the corresponding alignment crosses, with a dotted font that remains readable after the KOH etching. In such a way, once the best aligned pyramid is found it is sufficient to read the angular correction etched on the surface, which identifies the two alignment crosses to be used.

4.3.3 Wet etching of the microchannels

The pattern defining the microchannels is then transferred to the oxide mask via a further photolithography and dry etching process, us-

ing the alignment marks identified in the previous step. Such pattern is not a 1:1 drawing of the microchannel array, as is the case for deep reactive ion etching; instead it keeps into account the anisotropic behaviour of KOH etching. In particular, in order to obtain microchannels with vertical sidewalls, the arrays are oriented at 45° with respect to the flat of the wafer, i.e. along the $\langle 100 \rangle$ directions. With such orientation the sidewalls and the bottom of a microchannel are all made by $\{100\}$ crystalline planes, and hence a single etch rate e_{100} relative to these planes can be used for calculations. It should be noted that in the immediate vicinity of the $\langle 100 \rangle$ direction, the etching rate stays close to e_{100} (see Fig. 4.6), which is why the $\sim 0.1^\circ$ alignment precision used is sufficient for the control of this process. A simplified design approach for the design of the masks defining the microchannels was used, relying on the e_{100} rate only. In particular, let us consider a mask pattern of width w_0 , as shown in Fig. 4.7. To etch a microchannel of depth d , the etching time needed is simply given by $t = d/e_{100}$. However, since both sides of the pattern are also under-etched at the same rate, the width w of the channel will increase of a factor $\Delta w = 2te_{100} = 2d$; this means that using this etching technique only aspect ratios given by:

$$AR = \frac{d}{w} = \frac{d}{w_0 + \Delta w} = \frac{d}{w_0 + 2d} < \frac{1}{2} \quad (4.1)$$

can be obtained, as opposed to the high aspect ratios obtainable with deep reactive ion etching.² In channel turns, convex corners in the pattern expose the $\{111\}$ planes where the etching stops (or, more exactly, becomes much slower), yielding oblique surfaces. A couple of etching experiments that exemplify these results are shown in Fig. 4.8.

The slanted $\{111\}$ surfaces appearing in the corners at channel turns can be eliminated at the dicing step to open microchannels, in a similar fashion as the one described in section 4.2.4 for dry etched channels. Alternatively, such surfaces can be exploited as slanted micromirrors that deflect the scintillation light in the out of plane direction: in this case a transparent surface is placed above the micromirror, and there is no need to open the microchannels by dicing. These two possibilities are depicted in figure Fig. 4.9.

² It is however possible to obtain much higher aspect ratios by KOH etching, if silicon wafers with different crystalline orientations are used [97, 98]

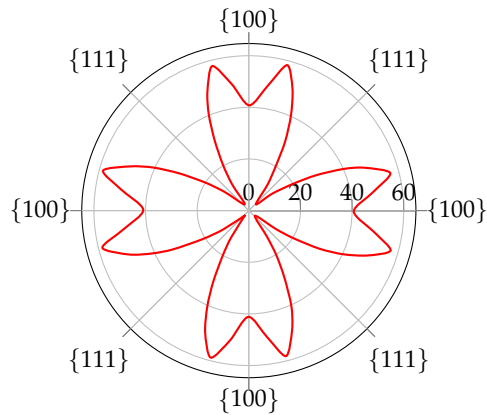


Figure 4.6.: Polar plot of the etch rate (in $\mu\text{m/h}$) measured in the in-plane direction for $\langle 100 \rangle$ silicon wafers exposed to 50% KOH at 78°C (adapted from [90]). In these conditions $e_{100} \sim 40 \mu\text{m/h}$. The flatness of the curve in correspondence of the $\{100\}$ planes reduces the sensitivity of the process to small alignment errors.

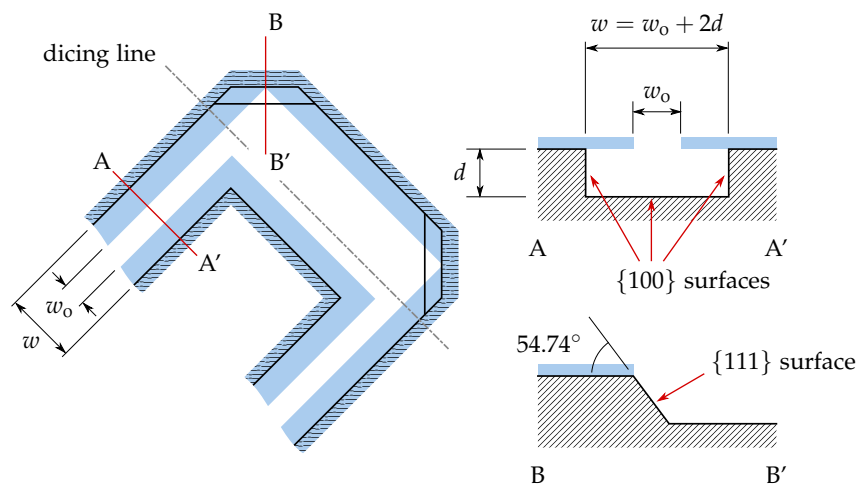


Figure 4.7.: Simplified calculation of the microchannel geometry resulting from KOH etching. The SiO_2 mask, depicted in light blue, defines microchannels oriented at 45° with respect to the wafer flat. The opening on the mask, of width w_0 , leads to microchannels of depth d and width $w = w_0 + 2d$ because of underetching. At the convex corners the etching “pins” to the $\{111\}$ crystalline planes, yielding slanted surfaces. These surfaces can either be eliminated at the dicing step to open the microchannels – for example cutting along the dicing line indicated in the figure – or engineered to act as slanted micromirrors that deflect the light in the out-of-plane direction.

4.3.4 Devices with in-plane light output

Devices with in-plane light output, i.e. such as the ones fabricated by dry etching, were fabricated with both one and two layers of microfluidic channels as follows.

For single layer devices, silicon wafers with a thickness of 0.525 mm were used, and the oxide etching mask – aligned to the wafer with the process described before – was designed in such a way to have microchannels with a depth of 0.4 mm. The width of the pattern defining the microchannels on the oxide mask was of 50 μm , which resulted in a final microchannel width of 0.85 mm. A pitch of 1.15 mm was chosen for the array, meaning the spacing between microchannels was of 0.3 mm. The oxide was patterned also on the other side of the wafer to yield openings corresponding to the fluidic inlets for the microchannels. In this way both the microchannels and the inlet could be obtained in the same etching step. After stripping the oxide mask with BHF, a further wet oxidation step was performed, then an aluminium film of 200 nm was sputtered on the microchannels to increase the reflectivity of the surfaces. A second silicon wafer was prepared, having the same SiO_2/Al film stack. This wafer was used to close the microchannels by thermocompression bonding of the Al/Al interface, performed at 490 °C and with a pressure of ~ 25 bar in a Suss SB6 substrate bonder. The oxide layers in this case act as barriers that avoid the diffusion of aluminium into the silicon (which would prevent the bonding). A cross section of the bonding interface is shown in Fig. 4.10a. The devices were then diced opening the microchannels at one side in such a way that fluid circulation is still possible. A strip of glass (SCHOTT D263, 0.15 mm thick) was then glued with epoxy to the side of the chip, to close the microchannels and provide an optical window for the output of the scintillation light.

This process was adapted to the fabrication of devices with two layers of microfluidic channels. In this case double side polished silicon wafers with a thickness of 0.38 mm were used. The wet oxide was patterned on both sides of the wafer to yield two microchannels arrays oriented at 90° with respect to each other, i.e. along the two $\langle 100 \rangle$ directions in the wafer plane. Both sides of the wafer were then etched at the same time in KOH, yielding microchannels with a depth of 150 μm (hence separated by a residual 80 μm silicon layer). In this case microchannels had a width of 0.5 mm and a pitch of 0.8 mm. After the oxide strip and re-oxidation processes, performed as in the previous case, aluminium was deposited on both sides of the wafer by sputtering. Two other aluminium-coated wafers were used to close respectively the frontside and backside microchannels, in a three-wafer

thermocompression bonding step. Fluidic inlets were mechanically drilled through one of the wafers prior to bonding. After bonding a dry etching step was performed to pierce through the 80 μm silicon membrane underneath the inlets, in order to provide a connection to the other layer of microchannels as well. The devices were then diced opening the microchannels at two sides of the chip (see Fig. 4.10b), and closing them again with two stripes of glass.

4.3.5 Devices with out-of-plane light output

Devices with out-of-plane light output were fabricated on silicon wafers with a thickness of 0.525 mm. The same process described for single layer devices in the previous section was used, except in this case the oxide mask at the channel turns was patterned as shown in Fig. 4.11a, in order for the $\{111\}$ surfaces to form slanted micromirrors at the end of each channel (Fig. 4.11b), that deflect the light in the out-of-plane direction. After the etching and the oxide strip, a smoothing process by wet oxidation and BHF etching was performed as described in section 4.2.1. An aluminium film of 200 nm was sputtered to yield reflective surfaces. The microchannels were closed with a pyrex wafer by anodic bonding. Such wafer featured aluminium stripes patterned in correspondence of the microchannels to provide a reflective cap, except in the area directly above the slanted micromirrors to provide a way out for the scintillation light. In this case the dicing only defines the device shape but does not cut through the microchannels. Fluidic tests proved that no air is trapped by these structures during the filling procedure.

4.4 LIGHT YIELD MEASUREMENTS

In this section the light yield measurements that were performed on silicon devices and the methods used to analyse the data are reported. In particular, devices with silicon microchannels fabricated by dry etching, as the one depicted in Fig. 4.3a, were used for the experiments.

4.4.1 Measurement setup

Electrons with an energy of up to 2.2 MeV, coming from a ^{90}Sr radioactive source, were used to excite the detector. Such particles have energies in the minimum ionization range for the liquid scintillator used to fill the microchannels (EJ-305 from ELJEN TECHNOLOGY, selected for its high light output). A SiPM (HAMAMATSU S12571-050P)

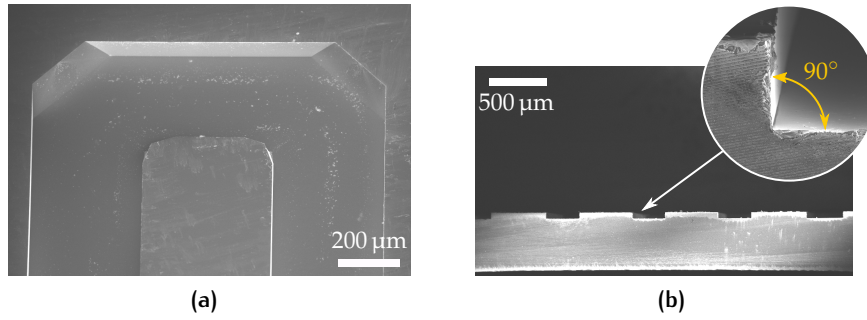


Figure 4.8.: Test microchannels etched by 40% KOH at 60 °C. (a) Turn of a microchannel similar to the one calculated in Fig. 4.7. (b) Cross section of a test microchannel array, showing the straight sidewalls.

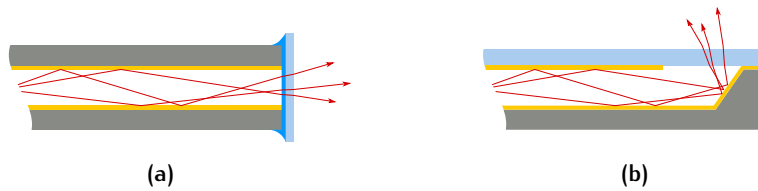


Figure 4.9.: Alternative designs for the termination of wet-etched microchannels. (a) Glass window glued on the side (“in-plane” light output). (b) Slanted channel ends with transparent window above (“out-of-plane” light output).

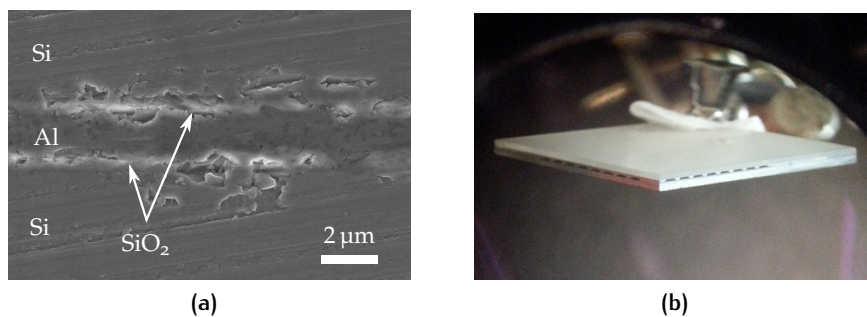


Figure 4.10.: (a) SEM micrograph showing the cross section of a Al-Al thermo-compression bonding. The SiO_2 film acts as a diffusion barrier that prevents the aluminium to diffuse into silicon. (b) Device with two orthogonal layer of microchannels, fabricated by the thermocompression bonding of three aluminium-coated wafers, shown after dicing.

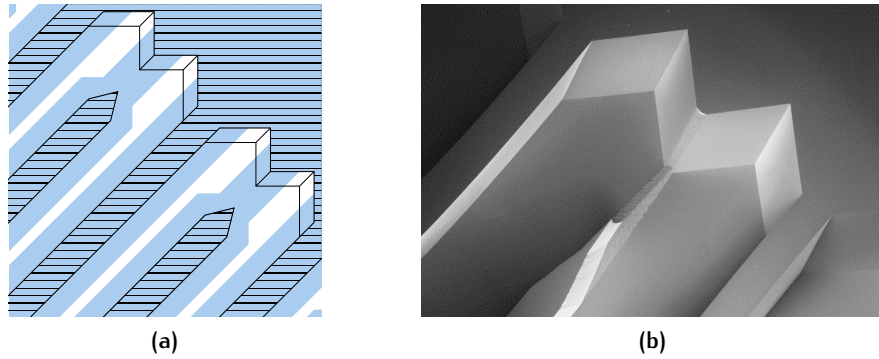


Figure 4.11.: (a) Sketch of the design used for the fabrication of microchannel ends featuring slanted mirror facets. The light blue represents the oxide mask while the hatched area represents the initial silicon surface. Notice that the microchannels are not joint in the mask design. (b) SEM micrograph showing the etching results, differing from the expectations of the simplified design approach only in the central part where the microchannels connect (due to secondary crystalline planes exposed during the etching).

was coupled to the end of the microchannels. A thin layer of optical grease (ELJEN TECHNOLOGY EJ-550) was applied between the SiPM and the glass window of the devices to avoid having an air gap in the optical path, and thus reduce the Fresnel reflection losses. Two rods of scintillating plastic having a cross section of $1 \times 1 \text{ mm}^2$, each coupled to a photodetector were superposed at a right angle below the microfluidic device under test; with such configuration, the coincidence of signals from both the photodetectors indicates the passage of an electron through the $1 \times 1 \text{ mm}^2$ surface defined by the superposition of the two rods (i.e. a *trigger event*). The detector composed by the SiPM/microchannels assembly could be moved with respect to the trigger area by a motorized table, so that it was possible to perform scans along microchannels.

4.4.2 Data analysis

For each interaction event selected by the trigger, the integral of the output pulse from the photodetector was recorded. Such value is a measure of the charge produced by the photodetector, and thus it is proportional to the number of detected photons. The data were gathered in histograms as shown in Fig. 4.12, in order to obtain the statistical distribution of the detector output signals. It can be noted, in particular in the leftmost part of the plot, that the data is distributed in a series of peaks.

The first peak, called *pedestal*, groups the events with the lowest signals, which correspond to the output of the photodetector when no photons were detected. This can happen because of both “fake”

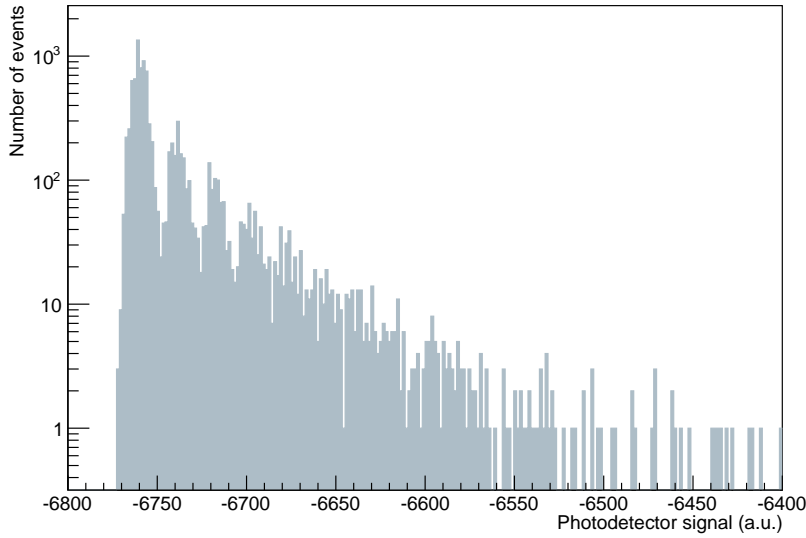


Figure 4.12.: Typical spectrum of the detector output signals, obtained from 9795 trigger events.

events (trigger coincidences not corresponding to the passage of a particle through the chip) or inefficiency of the detector (resulting from microchannel fill factor, limited thickness, light guide inefficiency,...). The pedestal P was modelled by a normal distribution:

$$P = \frac{k_p}{\sigma_0 \sqrt{2\pi}} \exp\left(-\frac{(x - \mu_0)^2}{2\sigma_0^2}\right) \quad (4.2)$$

Where the amplitude k_p is a scaling constant, the mean value μ_0 represents the average “zero photons” signal, and the standard deviation σ_0 accounts for the noise of the readout electronics.

The events contained in the successive peaks correspond to the detection of respectively one, two, three, etc. photons. Each peak was modelled with a normal distribution P_i :

$$P_i = \frac{k_i}{\sigma_i \sqrt{2\pi}} \exp\left(-\frac{(x - \mu_i)^2}{2\sigma_i^2}\right) \quad (4.3)$$

with

$$\mu_i = \mu_0 + i \cdot G \quad (4.4)$$

$$\sigma_i^2 = \sigma_0^2 + i \cdot \sigma_M^2 \quad (4.5)$$

$$k_i = \frac{k}{\pi} \int_0^\infty \exp\left(-t \log t - G \frac{i - N_{pe}^*}{\sigma^*} t\right) \sin(\pi t) dt \quad (4.6)$$

The mean value μ_i represents the average signal corresponding to i detected photons, and is defined in terms of the factor G , corresponding to the gain of the photodetector expressed in units of charge per photon. The standard deviation σ_i depends on both the noise of the readout electronics σ_0 and the shot noise $\sqrt{i} \cdot \sigma_M$ arising from the multiplication of i photoelectrons in the photodetector, which accounts for the increasing width of the peaks in the data histograms. The amplitude k_i is given by a scaling constant k multiplied by a Landau distribution with mode $\mu^* = \mu_0 + GN_{pe}^*$, where N_{pe}^* is an integer corresponding to the most probable number of output photoelectrons, and width σ^* . This keeps into account the fact that the number of photons produced by the scintillator is directly related to the energy deposited by the particle, which can be statistically described by a Landau distribution (see section 1.1.3).³ With such definitions, the complete model for the detector output statistics can be thus be written as an infinite sum of Gaussians, corresponding to the pedestal and to each single photoelectron contributing to the signal:

$$\begin{aligned}
 P + \sum_{i=1}^{\infty} P_i &= \frac{k_p}{\sigma_0 \sqrt{2\pi}} \exp\left(-\frac{(x - \mu_0)^2}{2\sigma_0^2}\right) \\
 &+ \frac{k}{\pi} \sum_{i=1}^{\infty} \left\{ \frac{1}{\sigma_i \sqrt{2\pi}} \exp\left(-\frac{(x - (\mu_0 + i \cdot G))^2}{2(\sigma_0^2 + i \cdot \sigma_M^2)}\right) \right. \\
 &\cdot \left. \int_0^{\infty} \exp\left(-t \log t - G \frac{i - N_{pe}^*}{\sigma^*} t\right) \sin(\pi t) dt \right\} \quad (4.7)
 \end{aligned}$$

The eight parameters of this model, summarised in table Tab. 4.1 and visualised over experimental data in Fig. 4.13, can be extracted by fitting. In particular, the parameters k_p , μ_0 and σ_0 were extracted by fitting Eq. (4.2) to the first peak, while the rest of the parameters were extracted by fitting Eq. (4.7) to the whole data set.

The Landau-weighting of the photoelectrons used in this model was found to fit data better than the typically used Poisson-weighting, most probably because the scintillator thickness involved is very limited, leading to high fluctuations in photon production (see section 1.1.3) and thus to a long tail in the distribution. Typically the average number $\langle N_{pe} \rangle$ of photoelectrons per MIP is given as a figure of merit for a scintillation detector. Since the average is not analitically

³ More exactly, the distribution of the number of photons would be given by the convolution of a Landau and a Poisson distribution. However such an approach makes data fitting much more complex and lengthy, without significant improvement of the results.

Table 4.1.: Parameters for the model of the detector output statistics.

Parameter	Significance
k_p	Pedestal scaling constant
μ_0	Average photodetector signal for zero photons
σ_0	Noise of the readout electronics
k	Scaling constant
G	Gain of the photodetector
σ_M	Shot noise of the photodetector
N_{pe}^*	Most probable number of output photoelectrons
σ^*	Width of the Landau distribution

defined for the Landau distribution, this parameter was calculated numerically as:

$$\langle N_{pe} \rangle = \frac{\sum_{i=0}^{\infty} i \cdot k_i}{\sum_{i=0}^{\infty} k_i} \quad (4.8)$$

where the infinite sum was truncated at one million terms.

Values of $\langle N_{pe} \rangle$ up to 2.7 were obtained for a single microchannel (see Fig. 4.14). By fitting the data obtained at different triggering positions along a microchannel, the dependency of $\langle N_{pe} \rangle$ from the excitation distance could be obtained. An attenuation length of ~ 20.4 mm was measured for the microchannels, as shown in Fig. 4.15.

4.5 SCINTILLATOR DAMAGE STUDIES

Experiments in which the liquid scintillator was damaged were performed [99], in order to provide a proof-of-principle of the possibility to replace it by pumping during the operation of the detector. In particular, UV radiation was used to damage the scintillator. UV light both excites fluorescent emission from the scintillator and induces damage at the same time by *photobleaching* (photochemical decomposition of the wavelength shifters). This mechanism, although different from the damage caused by ionizing radiation, provides a mean to degrade the light yield of the scintillator in a laboratory environment, avoiding the logistic and safety issues related to heavy irradiation tests. Moreover photobleaching occurs over a much shorter time scale than damage by ionizing radiation, allowing accelerated tests.

The chips, featuring a transparent opening on the microchannel top part (Pyrex locally not coated with aluminium), were filled with liquid scintillator (ELJEN TECHNOLOGY EJ-309) using a syringe pump and observed under a fluorescence microscope fitted with a 120 W mercury metal halide lamp (LEICA EL6000), filtered to emit primarily around the 360 nm spectral line. In a first experiment, the microchan-

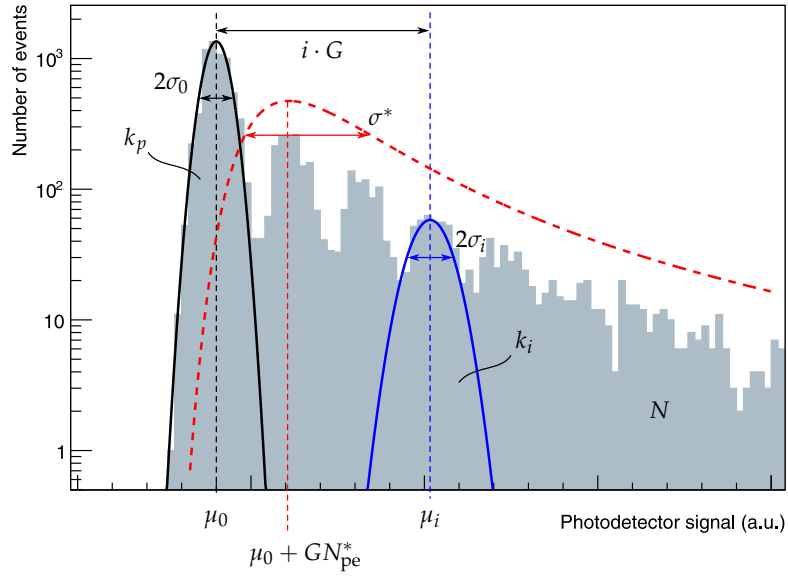


Figure 4.13.: Schematic depiction of some parameters of the model over experimental data. The black Gaussian represents the pedestal, the blue one the i^{th} photoelectron (in particular, $i = 3$ is shown), and the red dashed curve the Landau distribution, having a mode corresponding to the most probable photoelectron peak (in this example, $N_{\text{pe}}^* = 1$). The area of the histogram, N , corresponds to the total number of trigger events.

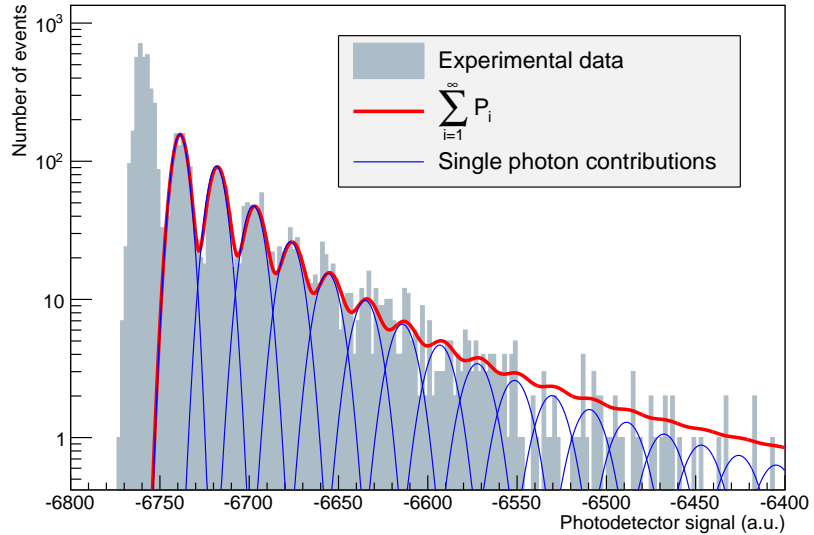


Figure 4.14.: Distribution of output signals from a microchannel with a depth of $190\ \mu\text{m}$, obtained from $N = 1087$ events, fitted with the model (4.7) (fit goodness $\chi^2/N_{\text{dof}} = 2.17$). In this case $N_{\text{pe}}^* = 1$, $\langle N_{\text{pe}} \rangle = 2.7$.

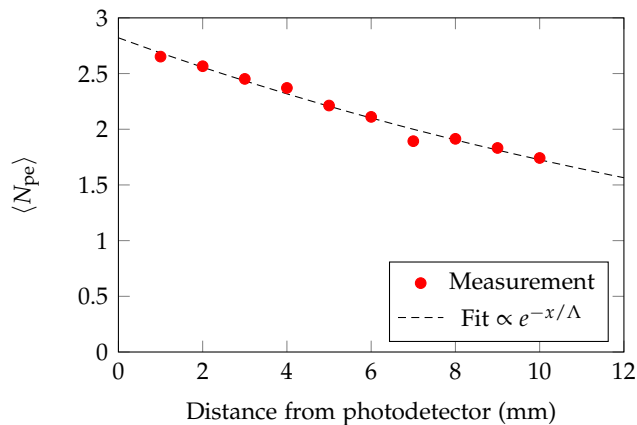


Figure 4.15.: Scan of the trigger position along a microchannel with a cross section of $700 \times 190 \mu\text{m}^2$. The data is well fit ($r^2 = 0.98$) by a decaying exponential with an attenuation length $\Lambda \sim 20.4 \text{ mm}$.

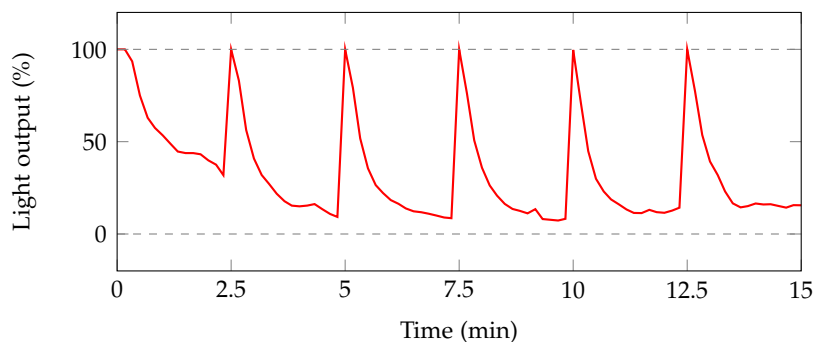


Figure 4.16.: Light output from the scintillator in a microchannel under continuous UV irradiation. Photobleaching damages the scintillator and rapidly reduces the light output (measured time constant of the decay: $\tau \sim 22 \text{ s}$). Fresh scintillator is pumped in every 2.5 min, bringing the light output back to 100% efficiency at each cycle.

nel was continuously irradiated with UV, and the light output was imaged with the microscope CCD, using a band pass filter ($570 \pm 20 \text{ nm}$) which selected the fluorescent light only. The liquid scintillator inside the chip was completely replaced by pumping every 2.5 min. The light output, which with no flow decays exponentially because of photobleaching, could be brought back to the initial value at each cycle (see Fig. 4.16), demonstrating that it is possible to completely change the damaged active material in the microfluidic detector (i.e. there is no backflow or local stagnation of the liquid).

A second experiment was performed by measuring the light output from the microchannels under continuous UV irradiation for different scintillator flow rates (imposed with the syringe pump). In this case it could be observed that, for each given flow rate, a dynamic equilibrium between the wavelength shifter molecules decomposed by photobleaching and the new ones introduced by pumping is es-

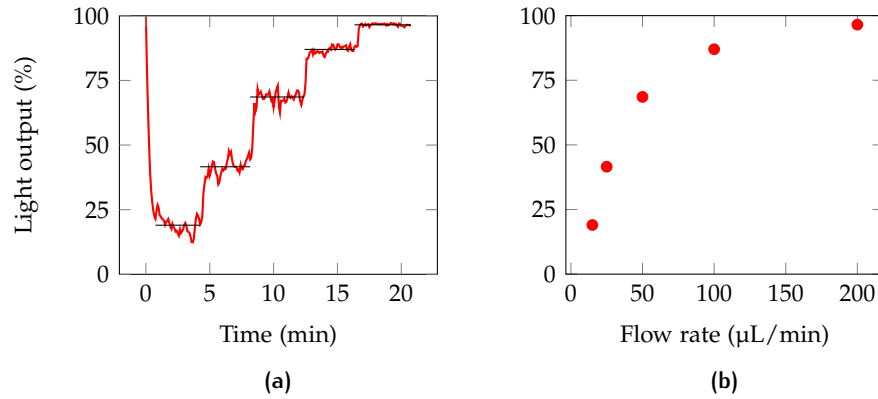


Figure 4.17.: (a) Light output from the scintillator in a microchannel under continuous UV irradiation for increasingly high flow rates. The plateaux correspond to the equilibria reached between scintillator photobleaching and replacement respectively at flow rates of 15, 25, 50, 100 and 200 $\mu\text{L}/\text{min}$. (b) Equilibrium light output as a function of flow rate, calculated by averaging each plateau.

tablished (see Fig. 4.17). This demonstrates that on top of the possibility of periodically replacing the scintillator, it is also possible to obtain a light output constant in time for a given irradiation condition by imposing a continuous flow. It should be noted that damage from ionizing particles occurs on much larger time scales than photobleaching, thus the flow rates needed to balance scintillator damage in a real application would be scaled down accordingly. Moreover, these proof-of-principle experiments do not keep into account the degradation of other components of the detector such as the optical coatings and the photodetectors, which would occur with exposure to ionizing radiation in an actual application and would contribute to the reduction of its overall life span.

4.6 CONCLUSIONS AND OUTLOOK

Silicon offers many technological possibilities for the fabrication of microfluidic scintillation detectors. Processes for the manufacturing of silicon devices based on both dry and wet etching techniques were developed, the former technique being advantageous in terms of flexibility and ease of design and the second in terms of fabrication cost and throughput. In particular, solutions were studied to eliminate scalloping in dry etched silicon sidewalls and to simplify the design of microchannels obtained by anisotropic wet etching. Devices with light output in both the in-plane and out-of-plane direction were fabricated, as well as devices featuring two layers of microfluidic channels. An experimental characterization of the light yield of some devices was obtained using electrons from a ^{90}Sr radioisotope. A proof-

of-concept study of the liquid scintillator ageing was performed to demonstrate the capability of scintillator circulation in microfluidic detectors. Tests in proton beams of complete prototypes of microfluidic scintillation detectors based on silicon and manufactured via the developed techniques are foreseen for the next future.

5

CONCLUSIONS AND OUTLOOK

In the context of this work, several technological solutions related to microfluidic scintillation detectors were developed and studied. The main results and perspectives can be summarised as follows.

Development of a Monte Carlo optical simulation tool

The tool, which was used to aid in the design of prototype devices, can perform simple simulations of light propagation in three dimensional models, using a hybrid geometrical optics/transfer matrix method approach. Ongoing developments aim to extend the underlying model to additional optical phenomena relevant to the guiding of scintillation light, in particular modal dispersion, chromatic dispersion and scattering by rough surfaces. The simulation speed of the tool can be further improved by (i) precalculating “reflectivity tables” for the materials with respect to the wavelength and incidence angle of the photons (as of now computed at simulation time) and (ii) reducing the computational complexity of the photon-surface collision detection algorithm (as of now linear with respect to the number of surfaces in the model), for example by applying *binary space partitioning* to the models of the geometry.

Development of prototype devices based on SU-8 resin

Microfabrication processes for the manufacturing of free standing monolithic SU-8 microfluidic devices were established. With these processes, devices embedding one or two layers of microfluidic channels were constructed, having a thickness of respectively 110 μm and 200 μm , which correspond to only $\sim 0.03\%$ and $\sim 0.06\%$ of the radiation length of SU-8. The protocols developed can be used to manufacture other types of suspended SU-8 microstructures different from microfluidic channels – such as cantilevers, bridges suspended masses, suspended membranes – which can be of interest in the field of polymer microsystems. A technique for the internal coating of the microchannels based on the injection of Teflon AF polymer solutions was investigated, but further development is needed to obtain a film thickness suitable for guiding light in the wavelength range of interest. An experimental validation of a SU-8 device was performed using a fluorescent solution with a high refractive index, as a proof-of-concept for a microfluidic detector operating by total in-

ternal reflection. For a complete characterization of the technology, further experiments in which scintillation light is excited by high energy particles need to be performed. This is possible by synthesizing a custom liquid scintillator with high-refractive index – such as the ones based on methyl naphthalene reported in literature – and using it to fill the SU-8 devices fabricated.

Development of prototype devices based on silicon

Microfabrication processes for the manufacturing of microchannels in silicon, having characteristics suitable for microfluidic scintillation detection, were established. Approaches based on both dry and wet etching were studied, in particular (i) a smoothing by wet oxidation technique was combined with a standard DRIE process to obtain dry etched microchannels with smooth surfaces usable for light guiding and (ii) a method for obtaining arrays of microchannels having straight sidewalls, based on standard KOH anisotropic wet etching, was devised and used to produce different kinds of devices (having one or two layers of microchannels, with in-plane or out-of-plane light output). Characterization experiments on silicon devices were performed using MeV-range electrons from a radioactive isotope. A physical model was used to fit experimental data and evaluate the performance of the detector. In particular, a maximum average of 2.7 photoelectrons per MIP and an attenuation length of about 20 mm were measured with this model for aluminium coated microchannels having a depth of 190 μm . Experiments of accelerated ageing of the detector in which the liquid scintillator was damaged by intense UV irradiation were performed, providing a proof-of-concept of how the capability of recirculating the active material in microfluidic scintillation detectors can be used to extend their lifetime or increase the stability of their performance in time. The promising results obtained on silicon microchannels led to the production of larger prototypes, for which a test in a proton beam is foreseen at the end of May 2015.



Basing on these results, several possibilities for microfluidic scintillation detectors can be imagined. Compact and portable detector devices can be obtained via the wafer-level integration of solid state photodetectors with silicon microchannels. Microchannels can be fabricated in the same substrate of solid state particle detectors such as silicon pixels, potentially leading to low material budget devices integrating different detection mechanisms (ionization and scintillation) as well as services (e.g. convective cooling of the detector using the liquid scintillator). The manufacturing of large arrays of microchannels

based on polymers, in order to build extended scintillation trackers, can be envisioned at contained costs, using manufacturing technologies from the plastics industry.

A

INTERNALS OF THE CUSTOM MONTE CARLO SIMULATOR

In this appendix further details on the inner mechanisms and models of the Monte Carlo simulator developed are given.

A.1 STRUCTURE AND DEPENDENCIES

The tool consists of a set of *Python 2* [100] scripts that can be grouped in three main modules, corresponding to the simulation workflow:

MODEL BUILDER These scripts are used to define the geometry (optical surfaces, position of the photodetectors, ...) and the optical properties (refractive indices, behaviour of the surfaces, ...) of the model to be analysed. A script describing a given model is written by the user, using the class library furnished by the framework, and is then compiled into a binary file that can be loaded by the tracer script. A tool based on *VPython* [101] that allows to inspect the geometry of the model in 3D is provided as well.

TRACER The tracer script loads the binary file describing the model and takes care of the generation and propagation of the photons according to the specifications of the user (position of the scintillation point, number of photons, maximum number of interactions allowed per photon, ...). The optics calculations are done via the *transfer matrix method* [102, 103, 48], using the *tnm* library [104]. The calculated photon trajectories are visualised in real time in a 3D viewer to have an immediate feedback on the correctness of the model (this feature is usually deactivated once the model is validated to reduce the simulation time). The results are written into a binary file in the form of a database that contains the trajectories and interactions of all the photons.

POST-PROCESSING These scripts load the database produced by the tracer and generate the wanted reports and plots, e.g. the photon transport efficiency, the spatial distribution of the photon hits, etc. The scientific computing libraries *NumPy* [105] and *SciPy* [106] are used for these calculations, while the output plots/histograms are generated with the *matplotlib* [107] library.

A.2 MODELS

A model is defined as a set of *optical interfaces*, with which the photons interact. Geometrically, each interface is a polygon defined by a set of $N \geq 3$ vectors $\{\vec{p}_1, \vec{p}_2, \dots, \vec{p}_N\}$ (with $\vec{p}_i \in \mathbb{R}^3$) describing the coplanar vertices of the polygon, in counter clockwise order. A normal unitary vector \hat{n} is associated to each interface, and it is used to describe its orientation in space: Such vector is calculated as:

$$\hat{n} = \frac{(\vec{p}_2 - \vec{p}_1) \times (\vec{p}_3 - \vec{p}_2)}{\|(\vec{p}_2 - \vec{p}_1) \times (\vec{p}_3 - \vec{p}_2)\|} \quad (\text{A.1})$$

Non planar objects are described as a set of planar interfaces. An interface can be flagged to be a *detector*, meaning the tracer will stop the calculation for the photons that hit it and consider them as detected (no modelling of the detector efficiency is present up to now). Each interface separates two *volumes*, to which the optical properties of the material are associated. The main property is the *complex refractive index* $n + jk$, calculated by interpolating a table of (λ, n, k) tuples to extract the value at the wanted wavelengths. The (λ, n, k) data is obtained experimentally from ellipsometry or from online databases. In the latest revisions, the possibility of pre-calculating *reflectivity maps* for the surfaces was introduced, i.e. tables that express the reflection probability $\rho(\lambda, \theta, P)$ as a function of the photon wavelength, angle of incidence and polarization (an example is shown in Fig. A.1). This reduces the simulation time as the probability can then be computed by interpolating the tables instead of being calculated in real time.

A.3 PHOTON PROPAGATION

In the tracer script, photons are generated either from a fixed point or from a random position in a segment representing the track of the particle in the scintillator. In the latter case, for a segment of length ℓ , the generation position along the segment is chosen for each photon with a uniform random distribution $\mathcal{U}_x(0, \ell)$. The direction of emission of the photon is represented by a unitary vector \hat{i} , initially chosen randomly within the whole solid angle – to model the isotropy of scintillation – with two uniform distributions $\mathcal{U}_{\psi, \phi}(0, 2\pi)$ which define its polar and azimuthal spherical coordinates.

Each photon is considered to propagate in a straight line until an optical interface is hit. For detecting the photon/interface collision, a simple algorithm is used that first determines whether \hat{i} intersects the plane of the polygon (computational complexity $O(1)$) and then determines if the intersection point is inside the polygon (complexity

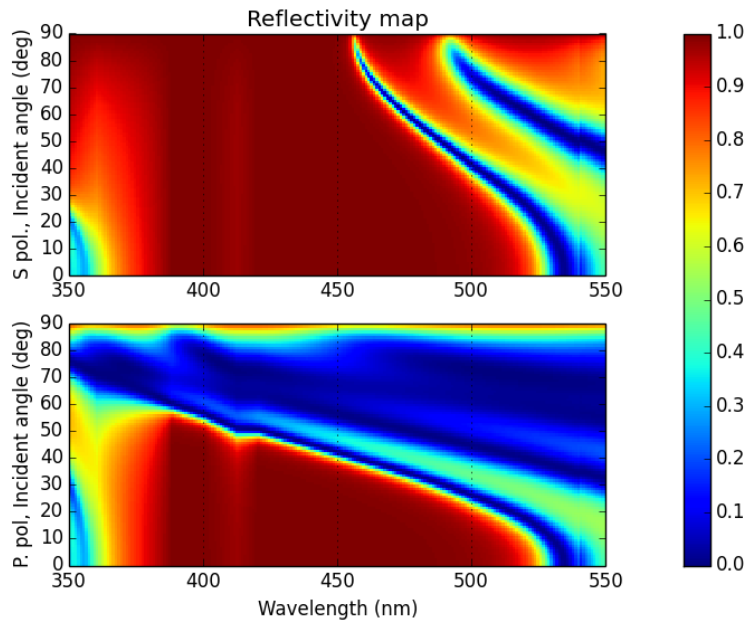


Figure A.1.: Reflectivity maps (for s and p polarization) calculated via the transfer matrix method for a microchannel coating consisting of 10 alternated layers of TiO_2 (35 nm) and SiO_2 (72 nm), a Bragg mirror structure calculated to efficiently reflect light emitted from the liquid scintillator over a broad range of angles. This example was chosen to show the capability of the simulator to manage complex optical coatings. Random polarizations is accounted for by performing an average of the s and p map.

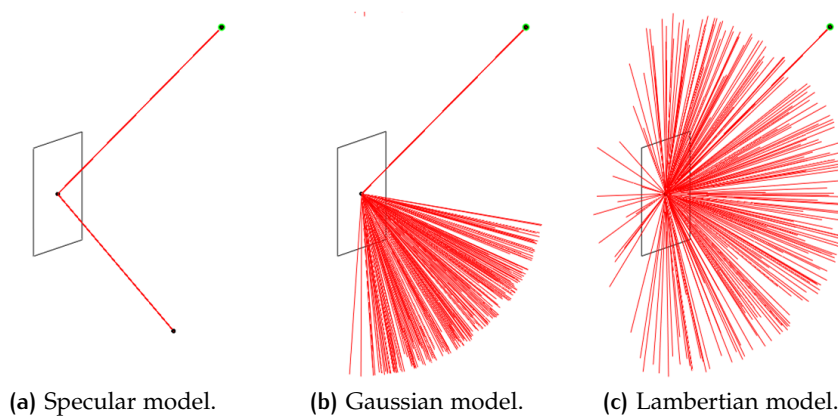


Figure A.2.: Simulations of a pencil beam of photons being reflected from a specular, rough, and diffusive surface.

$O(n)$ for a polygon with n edges). The current approach is however slow, because the intersection points with *all* the interfaces in the model are calculated at each step and then the closest one is selected to determine the actual collision (linear complexity with respect to the number of polygons in the model). A smarter choice would be to use data structures such as *binary space partitioning trees* or *octrees* to represent the model geometry and accelerate the search (logarithmic complexity with respect to the number of polygons). This is being considered for the next revisions.

Upon determination of the collision point, first the possibility that the photon was absorbed during its propagation in the optical volume is considered. The probability of occurrence of such event is computed from the absorption length of the material $\Lambda(\lambda)$ basing on the *Beer-Lambert law*:

$$p(\text{absorption}) = 1 - e^{-x/\Lambda(\lambda)} \quad (\text{A.2})$$

with x the travelled distance. If a photon is not absorbed, then it can be reflected or refracted. The probability of reflection R is calculated by the tmm library, solving the *Fresnel equations* for complex refractive indices with the transfer matrix method (conversely, the probability of refraction is $1 - R$). In the first versions this was done at simulation time for each collision, but in the latest revisions the use of precalculated tables was introduced, to reduce the computation time.

In case of a *reflection* event, the direction \hat{r} of the reflected photon is calculated according to the laws of specular reflection as:

$$\hat{r} = \hat{i} - 2(\hat{n} \cdot \hat{i})\hat{n} \quad (\text{A.3})$$

Where \hat{i} describes the direction of the incoming photon and \hat{n} is the normal to the surface of incidence. In the latest revisions, the addition of different reflective behaviours to model rough and diffusive surfaces is being studied, using respectively normal distributions or *Lambert's cosine law* (see Fig. A.2).

In the case of a *refraction* event, the direction of the refracted photon is calculated (only for dielectric media) using the vectorial form of *Snell's law*:

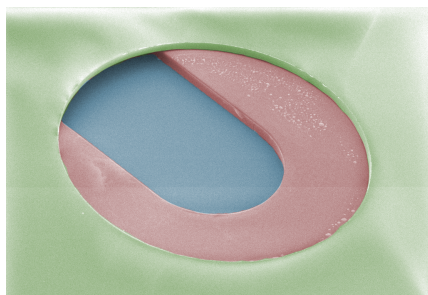
$$\hat{r} = \frac{n_1}{n_2}\hat{i} - \left(\frac{n_1}{n_2}\hat{n} \cdot \hat{i} + \sqrt{1 - \left(\frac{n_1}{n_2}\right)^2 (1 - (\hat{n} \cdot \hat{i})^2)} \right) \hat{n} \quad (\text{A.4})$$

Where $n_1(\lambda)$ and $n_2(\lambda)$ are the (real) refractive indices of the origin and destination optical media. For metallic media (complex refractive index) refracted photons are directly considered as absorbed to reduce the computation time (this assumption holds for most prac-

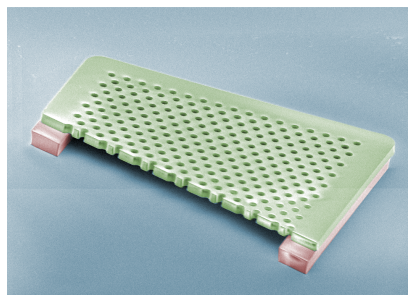
tical metals unless extremely thin layers, i.e. less than ~ 40 nm, are considered).

B | ADDITIONAL APPLICATIONS FOR THE SU-8 BONDING AND RELEASE PROCESS

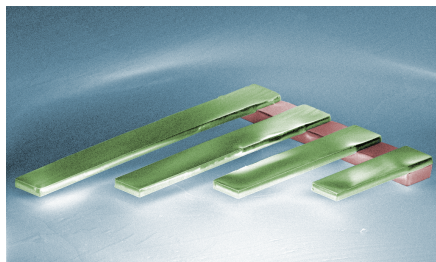
The processes based on full wafer bonding and release from sacrificial layers described in Chapter 3 can be used to manufacture different types of suspended SU-8 microstructures besides microfluidic channels. The fabrication of microfluidic channels by bonding crosslinked SU-8 layers is reported in literature [108, 109]. Free-standing chips are also described, but obtained by dissolving the whole carrier wafer rather than sacrificial films [110]. Other techniques to obtain such structures are reported in literature, but they either rely on the lamination [111] or deposition [112, 113] of *uncrosslinked* SU-8 films to create the suspended parts.



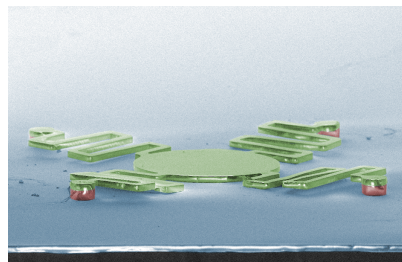
(a) Microchannel inlet.



(b) Suspended mesh.



(c) Cantilevers.



(d) Anchored dish.

Figure B.1.: Colourised SEM micrographs of various microstructures completely made of SU-8, using the processing technique described in Chapter 3. The base layer (30 μm thick) is colored in blue, the red structures (50 μm thick) are obtained directly over it, while the green ones (30 μm thick) are obtained on a separate wafer then bonded.

Such techniques yield a certain number of problems, such as the risk of reflow of the uncrosslinked resin inside cavities during thermal treatments, the long processing time needed for the development of unexposed resin in buried areas of the structures – which limits

their dimension – and the restrictions to the length of the suspended parts in the case of lamination. The proposed technique is a combination of these approaches, relying on the bonding of crosslinked SU-8 layers to avoid reflow problems and allowing to have longer suspended parts, but also introducing release from metal sacrificial layers to yield free-standing structures.

Some example of free-standing structures obtained with three layers of SU-8 are shown in Fig. B.1. All these test structures were obtained with the same process described in Chapter 3, in free areas of the wafers used for manufacturing microfluidic scintillation detectors. Fig. B.1a shows the inlet of a SU-8 microfluidic chip, demonstrating how microchannels with low aspect ratio can be obtained with this technique, without noticeable bending of the top membrane (In the depicted channel – 50 μm deep and 500 μm wide – the aspect ratio is of 1 : 10). The suspended membranes can be patterned, for example as the one shown in Fig. B.1b, which features 30 μm holes with a 50 μm spacing and is suspended for 800 μm . Fig. B.1c shows test cantilevers with a width of 100 μm and lengths of 400, 600, 800 and 1000 μm . A slight bending of the 30 μm thick resin under its own weight is noticeable in the longest two. By reducing the dimensions of the suspended part it is possible to obtain *flexible* anchors or springs, as shown in Fig. B.1d. In this case a dish (diameter 600 μm) is anchored to SU-8 pillars via 30 μm wide spring beams.

The integration of superficial or embedded electrodes in such structures can be obtained by including metal deposition and etching (or lift-off) steps in the fabrication process proposed. In such a way electrical actuation or sensing functionalities can be added, leading to potential applications in the field of plastic MEMS.

GLOSSARY

APD	Avalanche photodiode
AR	Aspect ratio
BHF	Buffered hydrofluoric acid
CCD	Charge coupled device
CERN	European Organization for Nuclear Research
CSDA	Continuous slowing down approximation
DC	Direct current
DRIE	Deep reactive ion etching
EDP	Ethylenediamine pyrocatechol
EMA	Extra-mural absorber
FEP	Fluorinated ethylene propylene
FF	Fill factor
GM1070	A commercial SU-8 resin by Gersteltec
Kapton	Commercial name of a polyimide polymer
KOH	Potassium hydroxide
LED	Light emitting diode
LHCb	Large Hadron Collider beauty
MAPMT	Multi anode photomultiplier tube
MEMS	Micro electromechanical system
MIP	Minimum ionizing particle
MSD	Microfluidic scintillation detector
Mylar	Commercial name of a polyethylene terephthalate polymer
PD	Photodiode
PDE	Photon detection efficiency

GLOSSARY

PFA	Perfluoroalkoxy
PGMEA	Propylene glycol methyl ether acetate
PMT	Photomultiplier tube
PR	Photoresist
PTFE	Polytetrafluoroethylene
Pyrex	Commercial name of a Corning borofloat glass
RPM	Revolutions per minute
SciFi	Scintillating fibre
SEM	Scanning electron microscope
SiPM	Silicon photomultiplier
Teflon	Commercial name for several DuPont fluoropolymers
TIR	Total internal reflection
TMAH	Tetramethylammonium hydroxide
TMM	Transfer matrix method
UV	Ultraviolet

BIBLIOGRAPHY

- [1] W. Crookes. "The emanations of radium". In: *Proceedings of the Royal Society of London* 71 (1903), pp. 405–408. URL: <http://goo.gl/fGnxud>.
- [2] S. C. Curran and W. R. Baker. *US. Atomic Energy Report MDDC. Radiation Laboratory, University of California, 1944.*
- [3] S. C. Curran and W. R. Baker. "Photoelectric Alpha-Particle Detector". In: *Review of Scientific Instruments* 19 (1948), p. 116. URL: <http://goo.gl/1i5HGp>.
- [4] R. Hofstadter. "The detection of gamma-rays with thallium-activated sodium iodide crystals". In: *Physical Review* 75 (1949), p. 796. URL: <http://goo.gl/ZR6Ay0>.
- [5] I. Broser and H. Kallmann. "Über die Anregung von Leuchtstoffen durch schnelle Korpuskularteilchen L (Eine neue Methode zur Registrierung und Energiemessung schwerer geladener Teilchen)". In: *Zeitschrift Naturforschung Teil A* 2 (1947), p. 439. URL: <http://goo.gl/EZ2To4>.
- [6] P. R. Bell. "The use of anthracene as a scintillation counter". In: *Physical Review* 73 (1948), p. 1405. URL: <http://goo.gl/zMEG50>.
- [7] W. S. Koski and C. O. Thomas. "Scintillations Produced by α -Particles in a Series of Structurally Related Organic Crystals". In: *Physical Review* 76 (1949), p. 308. URL: <http://goo.gl/7gCVEZ>.
- [8] M. Ageno, M. Chiazzotto, and R. Querzoli. "Sulla nuova tecnica dei contatori a scintillazione". In: *Rendiconti dell'Accademia Nazionale dei Lincei* 6 (1949), p. 626.
- [9] G. T. Reynolds, F. B. Harrison, and G. Salvini. "Liquid scintillation counters". In: *Physical Review* 78 (1950), p. 488. URL: <http://goo.gl/SL8eRo>.
- [10] M. G. Schorr and F. L. Torney. "Solid non-crystalline scintillation phosphors". In: *Physical Review* 80 (1950), p. 474. URL: <http://goo.gl/lzDUmd>.
- [11] J. Konijn et al. *RD46 status report: high resolution tracking devices based on capillaries filled with liquid scintillator*. Tech. rep. CERN-LHCC-97-038. CERN, 1997. URL: <http://goo.gl/5Byrkh>.

- [12] A. Mapelli et al. "Scintillation particle detection based on microfluidics". In: *Sensors and Actuators A: Physical* 162 (2010), pp. 272–275. URL: <http://goo.gl/f1TB1E>.
- [13] H. Bichsel. "A method to improve tracking and particle identification in TPCs and silicon detectors". In: *Nuclear Instruments and Methods in Physics Research A* 562 (2006), pp. 154–197. URL: <http://goo.gl/a9TxHs>.
- [14] K.A. Olive et al. (Particle Data Group). "Review of Particle Physics". In: *Chinese Physics C* 38.090001 (2014). URL: <http://goo.gl/mqQfss>.
- [15] E. A. Uehling. "Penetration of heavy charged particles in matter". In: *Annual Review of Nuclear Science* 4 (1954), pp. 315–350. URL: <http://goo.gl/95fh6x>.
- [16] H. Bichsel. "Straggling in thin silicon detectors". In: *Reviews of Modern Physics* 60 (1988), pp. 663–699. URL: <http://goo.gl/s6Vbeb>.
- [17] H. A. Bethe. "Molière's theory of multiple scattering". In: *Physical Review* 89 (1953), pp. 1256–1266. URL: <http://goo.gl/SpH2Nm>.
- [18] V. L. Highland. "Some practical remarks on multiple scattering". In: *Nuclear Instruments and Methods* 129 (1975), pp. 497–499. URL: <http://goo.gl/HPuQ3y>.
- [19] G. R. Lynch and O. I. Dahl. "Approximations to multiple Coulomb scattering". In: *Nuclear Instruments and Methods in Physics Research B* 58 (1991), pp. 6–10. URL: <http://goo.gl/qZNnGv>.
- [20] F. Brooks. "Development of organic scintillators". In: *Nuclear Instruments and Methods* 162 (1979), pp. 477–505. URL: <http://goo.gl/ahHz3Q>.
- [21] J. B. Birks. *The theory and practice of scintillation counting*. International series of monographs on electronics and instrumentation. Oxford: Pergamon, 1964.
- [22] W. R. Leo. *Techniques for Nuclear and Particle Physics Experiments*. 2nd ed. Springer, 1994.
- [23] T. Förster. "Zwischenmolekulare Energiewanderung und Fluoreszenz". In: *Annalen der Physik* 437 (1948), pp. 55–75. URL: <http://goo.gl/CBrLjT>.
- [24] D. Clark. "The intrinsic scintillation efficiency of plastic scintillators for ^{60}Co gamma excitation". In: *Nuclear Instruments and Methods* 117 (1974), pp. 295–303. URL: <http://goo.gl/HWd1aE>.
- [25] G. F. Knoll. *Radiation Detection and Measurement*. 3rd ed. Wiley, 1999.

- [26] L. Koester, K. Knopf, and W. Waschowski. “Neutron scattering length of lithium and boron and their isotopes”. In: *Zeitschrift für Physik A Atoms and Nuclei* 312 (1983), pp. 81–88. URL: <http://goo.gl/hVyPtg>.
- [27] V. Senchishin et al. “A new radiation stable plastic scintillator”. In: *Nuclear Instruments and Methods in Physics Research A* 364 (1995), pp. 253–257. URL: <http://goo.gl/YkXuID>.
- [28] A. Cardini et al. “Comparison of plastic scintillating fibres and capillaries filled with liquid scintillator”. In: *Nuclear Instruments and Methods in Physics Research A* 346 (1994), pp. 163–167. URL: <http://goo.gl/rs59gJ>.
- [29] S. Golovkin et al. “Radiation damage studies on new liquid scintillators and liquid-core scintillating fibers”. In: *Nuclear Instruments and Methods in Physics Research A* 362 (1995), pp. 283–291. URL: <http://goo.gl/jqB9d0>.
- [30] K. Arisaka. “New trends in vacuum-based photon detectors”. In: *Nuclear Instruments and Methods in Physics Research A* 442 (2000), pp. 80–90. URL: <http://goo.gl/LC6uag>.
- [31] Hamamatsu Photonics. *Photomultiplier Tubes Basics and Applications*. 2007. URL: <http://goo.gl/Lflgww>.
- [32] S. M. Sze and K. K. Ng. *Physics of semiconductor devices*. John Wiley & Sons, 2006.
- [33] G. Bondarenko et al. “Limited Geiger-mode silicon photodiode with very high gain”. In: *Nuclear Physics B-Proceedings Supplements* 61 (1998), pp. 347–352. URL: <http://goo.gl/EwnHOA>.
- [34] B. Dolgoshein et al. “Status report on silicon photomultiplier development and its applications”. In: *Nuclear Instruments and Methods in Physics Research Section A: Accelerators, Spectrometers, Detectors and Associated Equipment* 563 (2006), pp. 368–376. URL: <http://goo.gl/Im0Qny>.
- [35] Hamamatsu Photonics. *Hamamatsu Opto-semiconductor Digital Handbook*. URL: <http://goo.gl/Q0z9pV>.
- [36] C. P. Achenbach. “Active optical fibres in modern particle physics experiments”. In: (2003). URL: <http://goo.gl/DQiaK5>.
- [37] R. Ruchti et al. “A scintillating glass fiber-optic active target for vertex detection and tracking applications in high energy physics experiments”. In: *IEEE Transactions on Nuclear Science* 34 (1987), pp. 544–546. URL: <http://goo.gl/ypz1t5>.
- [38] The LHCb Collaboration. *LHCb Tracker Upgrade Technical Design Report*. Tech. rep. CERN-LHCC-2014-001. LHCb-TDR-015. CERN, 2014. URL: <http://goo.gl/kwV51g>.

- [39] A. Bay et al. *Viability Assessment of a Scintillating Fibre Tracker for the LHCb Upgrade*. Tech. rep. LHCb-PUB-2014-015. CERN-LHCb-PUB-2014-015. LHCb-INT-2013-004. CERN, 2014. URL: <http://goo.gl/6H4GSa>.
- [40] C. Joram. “LHCb SciFi, the new Fibre Tracker for LHCb”. In: *ECFA High Luminosity LHC Experiments Workshop*. Aix-Les-Bains, France, 2014. URL: <http://goo.gl/xF8sL6>.
- [41] S. Golovkin et al. “Development of tracking detectors based on capillaries with liquid scintillator”. In: *Nuclear Instruments and Methods in Physics Research Section A: Accelerators, Spectrometers, Detectors and Associated Equipment* 305 (1991), pp. 385–390. URL: <http://goo.gl/wGL1q0>.
- [42] M. Adinolfi et al. “Progress on high-resolution tracking with scintillating fibres: a new detector based on capillaries filled with liquid scintillator”. In: *Nuclear Instruments and Methods in Physics Research Section A: Accelerators, Spectrometers, Detectors and Associated Equipment* 315 (1992), pp. 177–181. URL: <http://goo.gl/TPwCk0>.
- [43] A. Bay et al. “A high-resolution tracking hodoscope based on capillary layers filled with liquid scintillator”. In: *Nuclear Instruments and Methods in Physics Research A* 457 (2001), pp. 107–116. URL: <http://goo.gl/YS1y4E>.
- [44] J. Konijn et al. “Capillary detectors”. In: *Nuclear Instruments and Methods in Physics Research Section A: Accelerators, Spectrometers, Detectors and Associated Equipment* 418 (1998), pp. 186–195. URL: <http://goo.gl/zdyvC9>.
- [45] A. Mapelli et al. “SU-8 microfluidic device for scintillating particle detection”. In: *Procedia Chemistry* 1.1 (2009), pp. 1347–1350. URL: <http://goo.gl/TTXImo>.
- [46] A. Mapelli et al. “Development and studies of a novel micro-fabricated radiation hard scintillation particle detector with high spatial resolution”. In: *Nuclear Physics B-Proceedings Supplements* 197 (2009), pp. 43–47. URL: <http://goo.gl/tFw2FB>.
- [47] A. Mapelli, P. Maoddi, and P. Renaud. *Microfabricated scintillation detector*. WO Patent App. PCT/EP2012/001,980. 2013. URL: <http://goo.gl/Wtj090>.
- [48] B. Saleh and M. Teich. *Fundamentals of Photonics*. Wiley, 2007.
- [49] DuPont. *Teflon AF properties*. URL: <http://goo.gl/B8CZoq>.
- [50] N. Products. *Norland Optical Adhesive 1375*. URL: <http://goo.gl/ttFgC5>.

- [51] Hamamatsu Photonics. *Photodiode arrays with amplifier*. URL: <http://goo.gl/kKDFR8>.
- [52] Eljen Technologies. *EJ-305 liquid scintillator*. URL: <http://goo.gl/0kB4qP>.
- [53] A. Busata, M. Haguenaer, and A. Karar. *Device for characterizing a particle beam*. WO Patent App. PCT/FR2007/050,790. 2007. URL: <http://goo.gl/3z2NFy>.
- [54] Berger et al. *ESTAR, PSTAR, and ASTAR: Computer Programs for Calculating Stopping-Power and Range Tables for Electrons, Protons, and Helium Ions*. 2005. URL: <http://goo.gl/whLbSY>.
- [55] M. Moridi et al. "An amorphous silicon photodiode array for glass-based optical MEMS application". In: *Sensors, 2009 IEEE*. IEEE. 2009, pp. 1604–1608. URL: <http://goo.gl/u3rB1c>.
- [56] E. Cuenot. *Étude de l'intégration verticale de photodiodes dans les détecteurs scintillants microfluidiques*. Master Thesis. Jan. 2014.
- [57] C. Wiese. *Integration of amorphous silicon photodiodes to microfluidic scintillation detectors*. Master Thesis. Aug. 2014.
- [58] S. e. a. "Agostinelli. "Geant4 - A Simulation Toolkit". In: *Nuclear Instruments and Methods A* 506 (2003), pp. 250–303. URL: <http://goo.gl/haoHFj>.
- [59] D. H. Wright. *Geant 4 Physics Reference Manual*. 2014. URL: <http://goo.gl/8D4H8I>.
- [60] K. Y. Lee et al. "Micromachining applications of a high resolution ultrathick photoresist". In: *Journal of Vacuum Science & Technology B* 13 (1995), pp. 3012–3016. URL: <http://goo.gl/OB4HF1>.
- [61] C. Cremers et al. "SU-8 as resist material for deep X-ray lithography". In: *Microsystem technologies* 7 (2001), pp. 11–16. URL: <http://goo.gl/uPev2k>.
- [62] M. Aktary et al. "High-resolution pattern generation using the epoxy novolak SU-8 2000 resist by electron beam lithography". In: *Journal of Vacuum Science & Technology B* 21 (2003), pp. L5–L7. URL: <http://goo.gl/34U5QL>.
- [63] F. E. Tay et al. "A novel micro-machining method for the fabrication of thick-film SU-8 embedded micro-channels". In: *Journal of Micromechanics and Microengineering* 11 (2001), p. 27. URL: <http://goo.gl/fuhjGF>.
- [64] P. Maoddi et al. "SU-8 as a Material for Microfabricated Particle Physics Detectors". In: *Micromachines* 5 (2014), pp. 594–606. URL: <http://goo.gl/WB4Ygn>.

- [65] H. Lorenz et al. "SU-8: a low-cost negative resist for MEMS". In: *Journal of Micromechanics and Microengineering* 7 (1997), pp. 121–124. URL: <http://goo.gl/V9awbb>.
- [66] C. Lee, K. Jiang, and G. Davies. "Sidewall roughness characterization and comparison between silicon and SU-8 microcomponents". In: *Materials Characterization* 58 (2007), pp. 603–609. URL: <http://goo.gl/JP9hBy>.
- [67] J.-N. Kuo, H.-W. Wu, and G.-B. Lee. "Optical projection display systems integrated with three-color-mixing waveguides and grating-light-valve devices". In: *Optics Express* 14 (2006), pp. 6844–6850. URL: <http://goo.gl/Mp016I>.
- [68] J. Melai et al. "The electrical conduction and dielectric strength of SU-8". In: *Journal of Micromechanics and Microengineering* 19 (2009). URL: <http://goo.gl/rd0vfv>.
- [69] J. Melai et al. "Qualitative and quantitative characterization of outgassing from SU-8". In: *Microelectronic Engineering* 86 (2009), pp. 761–764. URL: <http://goo.gl/d3EYKy>.
- [70] M. Key, V. Cindro, and M. Lozano. "On the radiation tolerance of SU-8, a new material for gaseous microstructure radiation detector fabrication". In: *Radiation Physics and Chemistry* 71 (2004), pp. 1003–1007. URL: <http://goo.gl/vLSzbd>.
- [71] S. Metz, A. Bertsch, and P. Renaud. "Partial release and detachment of microfabricated metal and polymer structures by anodic metal dissolution". In: *Journal of Microelectromechanical Systems* 14 (2005), pp. 383–391. URL: <http://goo.gl/BQpiqD>.
- [72] D. Haftgoli Bakhtiari. *Development of a set-up for the injection of optical coatings in embedded microfluidic waveguides*. EPFL Semester Project Report. Jan. 2013. URL: <http://goo.gl/oMKo7G>.
- [73] D. McMeekin. *Teflon Coating of Microfluidic Channels for Scintillation Detectors*. EPFL Semester Project Report. June 2013. URL: <http://goo.gl/3Mt6Zx>.
- [74] "Properties of Amorphous Fluoropolymers Based on 2,2-Bistrifluoromethyl-4,5-Difluoro-1, 3-Dioxole". In: *183rd Meeting of the Electromechanical Society Honolulu*. 1993, pp. 1–11.
- [75] R. Manor et al. "Microfabrication and characterization of liquid core waveguide glass channels coated with Teflon AF". In: *Sensors Journal, IEEE* 3 (2003), pp. 687–692. URL: <http://goo.gl/EKJovV>.
- [76] C.-W. Wu and G.-C. Gong. "Fabrication of PDMS-Based Nitrite Sensors Using Teflon AF Coating Microchannels". In: *Sensors Journal, IEEE* 8 (2008), pp. 465–469. URL: <http://goo.gl/oPuYed>.

- [77] DuPont. *Teflon FEP Resin and Film*. URL: <http://goo.gl/abDGtc>.
- [78] DuPont. *Teflon PFA Resin and Film*. URL: <http://goo.gl/WLPuDg>.
- [79] DuPont. *DuPont Teflon AF 1601S and 2400S*. URL: <http://goo.gl/4koR8X>.
- [80] C. Wohlfarth. "Refractive index of diiodomethane". In: *Refractive Indices of Pure Liquids and Binary Liquid Mixtures*. Springer, 2008, pp. 68–68.
- [81] W. Snoeys et al. "First beam test results from a monolithic silicon pixel detector". In: *Nuclear Instruments and Methods in Physics Research Section A: Accelerators, Spectrometers, Detectors and Associated Equipment* 326 (1993), pp. 144–149. URL: <http://goo.gl/OhRfZO>.
- [82] M. Elwenspoek and H. V. Jansen. *Silicon micromachining*. Cambridge, UK: Cambridge University Press, 2004.
- [83] M. J. Madou. *Fundamentals of microfabrication: the science of miniaturization*. CRC press, 2002.
- [84] H. Winters and J. Coburn. "The etching of silicon with XeF₂ vapor". In: *Applied Physics Letters* 34 (1979), pp. 70–73. URL: <http://goo.gl/QtCwtA>.
- [85] G. Schwartz and P. Schaible. "Reactive ion etching of silicon". In: *Journal of Vacuum Science and Technology* 16 (1979), pp. 410–413. URL: <http://goo.gl/kRPc9Z>.
- [86] T. Pandhumsoporn et al. *High-etch-rate anisotropic deep silicon plasma etching for the fabrication of microsensors*. 1996. URL: <http://goo.gl/zh00H7>.
- [87] "High aspect ratio via etching conditions for deep trench of silicon". In: *Surface and Coatings Technology* 171 (2003), pp. 290–295. URL: <http://goo.gl/YjbHaF>.
- [88] M. J. Declercq, L. Gerzberg, and J. D. Meindl. "Optimization of the Hydrazine-Water Solution for Anisotropic Etching of Silicon in Integrated Circuit Technology". In: *Journal of The Electrochemical Society* 122 (1975), pp. 545–552. URL: <http://goo.gl/kBfdSW>.
- [89] A. Reisman et al. "The Controlled Etching of Silicon in Catalyzed Ethylenediamine-Pyrocatechol-Water Solutions". In: *Journal of the Electrochemical Society* 126 (1979), pp. 1406–1415. URL: <http://goo.gl/WnGQeb>.

- [90] H. Seidel et al. "Anisotropic Etching of Crystalline Silicon in Alkaline Solutions: I. Orientation Dependence and Behavior of Passivation Layers". In: *Journal of The Electrochemical Society* 137 (1990), pp. 3612–3626. URL: <http://goo.gl/e8xpM2>.
- [91] O. Tabata et al. "Anisotropic etching of silicon in TMAH solutions". In: *Sensors and Actuators A: Physical* 34 (1992), pp. 51–57. URL: <http://goo.gl/wBWKx9>.
- [92] P. Maoddi et al. "Scintillation detectors based on silicon microfluidic channels". In: *Journal of Instrumentation* 9 (2014). URL: <http://goo.gl/NkDtS0>.
- [93] Y.-T. Cheng et al. "Vacuum packaging technology using localized aluminum/silicon-to-glass bonding". In: *Microelectromechanical Systems, Journal of* 11 (2002), pp. 556–565. URL: <http://goo.gl/bww7CK>.
- [94] L. Batooli. *Towards integration of amorphous silicon photodiodes to microfluidic scintillation detectors*. Master Thesis. Jan. 2014.
- [95] N. Ashcroft and N. Mermin. *Solid State Physics*. Philadelphia: Saunders College, 1976.
- [96] G. Ensell. "Alignment of mask patterns to crystal orientation". In: *Sensors and Actuators A: Physical* 53 (1996), pp. 345–348. URL: <http://goo.gl/iA2mfV>.
- [97] D. L. Kendall. "On etching very narrow grooves in silicon". In: *Applied Physics Letters* 26 (1975), pp. 195–198. URL: <http://goo.gl/RM042L>.
- [98] D. L. Kendall. "Vertical etching of silicon at very high aspect ratios". In: *Annual Review of Materials Science* 9 (1979), pp. 373–403. URL: <http://goo.gl/AMkUYv>.
- [99] D. Brouzet. *Mechanical and fluidic integration of scintillating microfluidic channels into detector system*. Master Thesis. Aug. 2014.
- [100] *Python programming language*. URL: <https://www.python.org/>.
- [101] D. Scherer. *VPython, 3D Programming for Ordinary Mortals*. URL: <http://vpython.org/>.
- [102] M. Born and E. Wolf. *Principles of optics: electromagnetic theory of propagation, interference and diffraction of light*. 7th ed. Cambridge university press, 1999.
- [103] C. C. Katsidis and D. I. Siapkas. "General transfer-matrix method for optical multilayer systems with coherent, partially coherent, and incoherent interference". In: *Applied optics* 41 (2002), pp. 3978–3987. URL: <http://www.opticsinfobase.org/ao/fulltext.cfm?uri=ao-41-19-3978>.

- [104] S. J. Byrnes. *tmm library manual*. URL: http://sjbyrnes.com/fresnel_manual.pdf.
- [105] *NumPy package*. URL: <http://www.numpy.org/>.
- [106] *SciPy library*. URL: <http://www.scipy.org/>.
- [107] *matplotlib plotting library*. URL: <http://matplotlib.org/>.
- [108] F. Blanco et al. "Novel three-dimensional embedded SU-8 microchannels fabricated using a low temperature full wafer adhesive bonding". In: *Journal of Micromechanics and Microengineering* 14 (2004), p. 1047. URL: <http://goo.gl/AbTfsd>.
- [109] M. Agirregabiria et al. "Fabrication of SU-8 multilayer microstructures based on successive CMOS compatible adhesive bonding and releasing steps". In: *Lab on a Chip* 5 (2005), pp. 545–552. URL: <http://goo.gl/DdG4i8>.
- [110] S. Tuomikoski and S. Franssila. "Free-standing SU-8 microfluidic chips by adhesive bonding and release etching". In: *Sensors and Actuators A: Physical* 120 (2005), pp. 408–415. URL: <http://goo.gl/GPmq3c>.
- [111] P. Abgrall et al. "A novel fabrication method of flexible and monolithic 3D microfluidic structures using lamination of SU-8 films". In: *Journal of Micromechanics and Microengineering* 16 (2006), p. 113. URL: <http://goo.gl/OG2LZE>.
- [112] A. Mata, A. J. Fleischman, and S. Roy. "Fabrication of multi-layer SU-8 microstructures". In: *Journal of micromechanics and microengineering* 16 (2006), p. 276. URL: <http://goo.gl/NDFtSn>.
- [113] H. Sato et al. "An all SU-8 microfluidic chip with built-in 3D fine microstructures". In: *Journal of Micromechanics and Microengineering* 16 (2006), p. 2318. URL: <http://goo.gl/iRgEVA>.

Pietro Maoddi

Chemin de Villars 1
1030 Bussigny
Switzerland
☎ +41 078 7392086
✉ pietro.maoddi@gmail.com

Personal information

Date of birth January 5th 1988
Nationality Italian

Experience

- 2012–2015 **Doctoral student.**
Physics Department, European Organization for Nuclear Research (CERN)
Microsystems Laboratory, École Polytechnique Fédérale de Lausanne (EPFL)
- 2011–2012 **Intern.**
Physics Department, European Organization for Nuclear Research (CERN)
- 2011 **Master project intern.**
Ayanda Biosystems SA
Microsystems Laboratory, École Polytechnique Fédérale de Lausanne (EPFL)
- 2010 **Research intern.**
Biomicrofluidics Laboratory, University of California Los Angeles (UCLA)

Education

- 2012–2015 **Ph.D. in Microsystems and Microelectronics.**
École Polytechnique Fédérale de Lausanne (EPFL), Switzerland
- 2009–2011 **M.Sc. in Micro and Nano Technologies.**
110/110, cum Laude
Politecnico di Torino, Italy
Institut National Polytechnique de Grenoble (INPG), France
École Polytechnique Fédérale de Lausanne (EPFL), Switzerland
- 2006–2009 **B.Sc. in Computer Engineering.**
110/110
Politecnico di Torino, Italy
Institut National de Sciences Appliquées (INSA) de Lyon, France
- 2001–2006 **Maturità Scientifica.**
100/100
Liceo Scientifico Enrico Fermi di Nuoro, Italy

Publications & patents

P. Maoddi et al. **SU-8 as a Material for Microfabricated Particle Physics Detectors**, *Micromachines* 5, pp. 594–606 (2014).

P. Maoddi et al. **Scintillation detectors based on silicon microfluidic channels**, *Journal of Instrumentation* 9 (2014).

H. Deschout, K. Raemdonck, S. Stremersch, P. Maoddi et al. **On-chip light sheet illumination enables diagnostic size and concentration measurements of membrane vesicles in biofluids**, *Nanoscale* 6, pp. 1741–1747 (2013).

H. Deschout, K. Raemdonck, S. Stremersch, P. Maoddi et al. **Disposable microfluidic chip with integrated light sheet illumination enables diagnostics based on membrane vesicles**, 17th International Conference on Miniaturized Systems for Chemistry and Life Sciences (MicroTAS 2013) Freiburg, Germany. Vol. 3, pp. 2010–2012 (2013).

A. Mapelli, P. Maoddi and P. Renaud **Microfabricated scintillation detector**, WO Patent PCT/EP2012/001980 (2013).

E. Sollier, C. Murray, P. Maoddi, D. Di Carlo **Rapid prototyping polymers for microfluidic devices and high pressure injections**, *Lab on a Chip* 11, pp. 3752–3765 (2011).

Supervised projects

2015 **Design and fabrication of silicon photodiodes for microfluidic scintillation detectors.**

Rosalia Moreddu (Politecnico di Torino), Master project at CERN.

2015 **Fabrication of microfluidic scintillation detectors based on PMMA microchannels.**

Jacopo Bronuzzi (Politecnico di Torino), Master project at CERN.

2014-2015 **Development of readout system for photodiode arrays.**

Hariharan Katharajan, internship at CERN.

2014 **Development of a SiPM readout system and a trigger system for microfluidic scintillation detectors.**

Mikhail Asiatici (Politecnico di Torino), Master project at CERN.

2014 **Integration of amorphous silicon photodiodes to microfluidic scintillation detectors.**

Davy Brouzet (EPFL), Master project at CERN.

2014 **Integration of amorphous silicon photodiodes to microfluidic scintillation detectors.**

Cindy Wiese (EPFL), Master project at CERN.

- 2014 **Improvement of Monte Carlo simulator of light transport in microfluidic channels.**
Guillaume Catry (EPFL), Summer project at CERN.
- 2013-2014 **Towards integration of amorphous silicon photodiodes to microfluidic scintillation detectors.**
Leili Batooli (EPFL), Master project at CERN.
- 2013-2014 **Étude de l'intégration verticale de photodiodes dans les détecteurs scintillants microuidiques.**
Eric Cuenot (EPFL), Master project at CERN.
- 2013 **Development of KOH etched microchannels for microfluidic scintillation detectors.**
Ludovic Serex (EPFL), Summer project at LMIS4.
- 2013 **Teflon Coating of Microfluidic Channels for Scintillation Detectors.**
David McMeekin (EPFL), Semester project at LMIS4.
- 2013 **Development of a set-up for the injection of optical coatings in embedded microfluidic waveguides.**
Dara Haftgoli Bakhtiari (EPFL), Semester project at LMIS4.